

Electron-Reservoir Effect on a Perylene Diimide Tethered Rhenium Bipyridine Complex for CO₂ Reduction

Josh D. B. Koenig^a, Zachary Dubrawski^a, Keerthan R. Rao^b, Janina Willkomm^a, Benjamin S. Gelfand^a, Chad Risko^b, Warren E. Piers^a, and Gregory C. Welch^{a*}

^a Department of Chemistry, University of Calgary, 2500 University Drive N.W., Calgary, Alberta, T2N 1N4, Canada.

^b Department of Chemistry & Center for Applied Energy Research, University of Kentucky, Lexington, Kentucky 40506, United States

* Corresponding Author
Email: gregory.welch@ucalgary.ca
Phone Number: 1-403-210-7603

■ Abstract

Here we report on a molecular catalyst with a built-in electron-reservoir for enhanced CO₂ conversion. The synthesis and characterization of this N-annulated perylene diimide (PDI) photosensitized Re(bpy) supramolecular dyad [**Re(bpy-TAz-PDI)**], as well as successful electro- and photocatalytic CO₂-to-CO conversion, are detailed herein. Upon electrochemical reduction in the presence of CO₂ and a proton source, **Re(bpy-TAz-PDI)** exhibited significant current enhancement, where the onset of electrocatalytic CO₂ reduction for **Re(bpy-TAz-PDI)** occurred at a much less negative potential than standard Re(bpy) complexes. At an applied potential of -1.8 V vs. Fc^{+/0}, 400 mV lower than the benchmark Re(dmbpy) catalyst, **Re(bpy-TAz-PDI)** was able to achieve the same catalytic activity (TON_{co} = 24) and Faradaic efficiency (FE = 92 %) during controlled potential electrolysis (CPE) experiments. Through a combination of UV-visible-nearIR spectroelectrochemistry (SEC), FTIR SEC, and chemical reduction experiments, it was shown that the PDI-moiety served as an electron-reservoir for Re(bpy), thereby allowing catalytic activity at lower overpotentials. Density functional theory (DFT) studies probing the optimized geometries, frontier molecular orbitals, and spin-densities of various catalytic intermediates revealed that the geometric configuration of PDI, relative to the Re(bpy)-moiety, plays a critical role in accessing electrons from the electron-reservoir. The near identical performance of **Re(bpy-TAz-PDI)** at lower overpotentials relative to the benchmark Re(dmbpy) catalyst highlights the utility of organic chromophore electron-reservoirs as a method for lowering the required overpotential for CO₂ conversion.

■ Introduction

The conversion of combustion products (i.e. CO₂, H₂O) back to chemical precursors and fuels using electrons derived from renewable resources is one viable path towards lowering carbon-emissions and closing the carbon-loop.^{1,2} In theory, solar radiation provides enough energy to perform these thermodynamically and kinetically uphill chemical reactions; but in practice, catalysts are required to enable efficient product delivery.^{3,4} While heterogeneous electrocatalysts are favored for their scalability and facile device integration, these materials often suffer from a lack of product selectivity.⁵⁻⁷ The use of single-atom heterogeneous electrocatalysts can help enhance product selectivity.⁸⁻¹⁰ However, the rational design of molecular catalysts affords a more systematic method to tune and improve catalyst activity and product selectivity.^{11,12} Though most molecular catalysts require a high overpotential to drive electrocatalytic CO₂ reduction, issues concerning the durability of these systems can often be resolved by immobilizing these molecular catalysts.¹³⁻¹⁹ For these catalysts to be employed in long-lasting and industrially-relevant devices, catalyst design should emphasize the importance of accomplishing these chemical processes efficiently at the lowest overpotential possible.^{2,20-23}

One of the most well-explored CO₂ reduction catalyst motifs, first introduced by Lehn and co-workers,²⁴ is based upon Re(2,2'-bipyridine)(CO)₃Cl [Re(bpy)]. The synthetic versatility of the bpy ligand means catalyst properties can be tailored to lower overpotentials for CO₂ electrocatalysis through use of either electronically varied substituents²⁵⁻²⁸ or second-sphere H-bonding groups (see Supporting Information, SI, Table S1).²⁹⁻³¹ Moreover, these catalysts can be tethered to photosensitizers, such as the ruthenium(II) diimine complexes investigated by Ishitani and co-workers, to generate supramolecular dyads that are capable of CO₂ photocatalysis.³²⁻³⁴ Despite the many design principles established for these Ru^{II}-Re^I supramolecular dyads, the extension of these principles towards other organic chromophore photosensitizers is less common. Beyond porphyrins,³⁵⁻³⁷ rylene (di)imides such as naphthalimide,³⁸ naphthalene diimide,³⁹⁻⁴¹ and perylene diimide (PDI)^{42,43} have also been used to photosensitize Re(bpy). While the photophysical properties of these rylene (di)imide functionalized Re(bpy) supramolecular dyads have been thoroughly investigated, surprisingly only the naphthalimide-functionalized rhenium diimine complexes reported by Gobetto and co-workers³⁸ were examined as CO₂ electro- and photocatalysts.

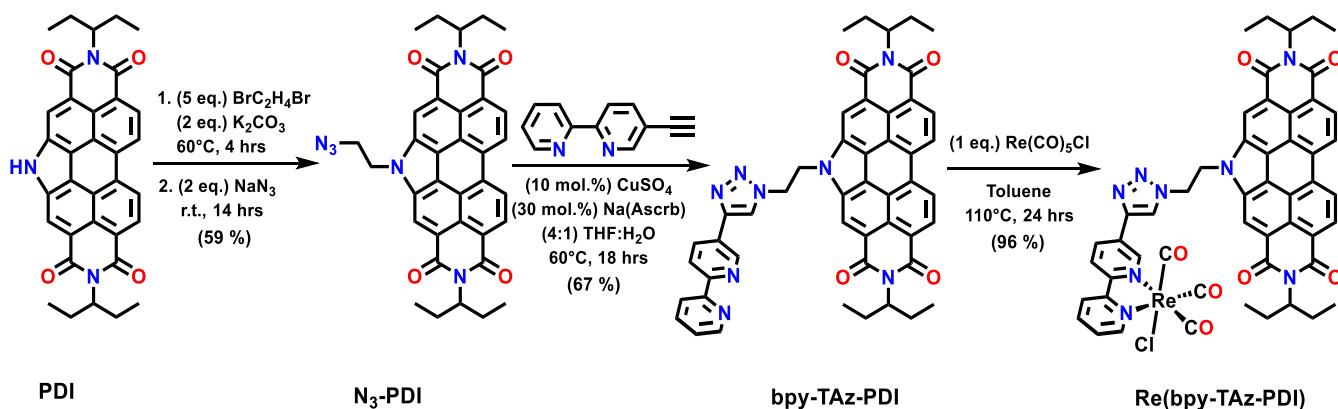
Recognizing the structural diversity and catalytic potential of these hybrid supramolecular dyad systems, we targeted a versatile N-annulated PDI photosensitized Re(bpy) complex. PDIs are ideally suited for photosensitization because they possess high molar absorptivity and redox stability.^{44,45} Relative to other PDI materials, N-annulation provides a pair of nonbonding electrons that can donate into the π -system of the PDI chromophore.^{46,47} This electron donation slightly destabilizes the frontier molecular energy levels, which improves the energetic match between Re(bpy) and the PDI chromophore.⁴⁷ Moreover, the pyrrolic nitrogen on N-annulated PDI provides a synthetically versatile handle through which the dyads' physical and optoelectronic properties may be further tuned.⁴⁷⁻⁵⁰ And unlike previously reported rylene diimide systems,³⁹⁻⁴³ imide functionalization of the perylene precursor may be done symmetrically, making this N-annulated PDI system synthetically more accessible and scalable. Herein we report the synthesis, characterization, and catalytic properties of an N-annulated PDI tethered Re(bpy) supramolecular dyad [**Re(bpy)-TAz-PDI**] capable of CO₂-to-CO electro- and photocatalysis. We show through a series of controlled potential electrolysis (CPE) and

spectroelectrochemistry (SEC) experiments, as well as density functional theory (DFT) calculations that N-annulated PDI acts as an electron-reservoir for Re(bpy), enabling efficient CO₂ reduction at an overpotential 400 mV lower than conventional Re(bpy) catalysts.

■ Synthesis and Characterization

The synthesis of **Re(bpy-TAz-PDI)** (Scheme 1), starting from N-annulated PDI,⁴⁷ exploited an alkylation of the pyrrolic nitrogen with 1,2-dibromoethane followed by an azide-substitution, according to an established literature procedure.⁴⁸ The C2 tether length was selected to mimic the design principles outlined for the Ru^{II}–Re^I supramolecular dyads, where short tether-lengths have proven critical for efficient electron-transfer.^{32–34} Next, N₃-PDI was attached to alkyne-functionalized bipyridine *via* copper catalyzed alkyne-azide cycloaddition,⁴⁸ generating the ligand (bpy-TAz-PDI). Lastly, bpy-TAz-PDI was metallated with Re(CO)₅Cl to afford **Re(bpy-TAz-PDI)** in an overall yield of 38 %, over 4 synthetic steps (see SI for more details).

Scheme 1. Synthesis of bpy-TAz-PDI Ligand and Re(bpy-TAz-PDI) Supramolecular Dyad



The identity of **Re(bpy-TAz-PDI)** was confirmed by MALDI-TOF MS and elemental analysis (Figure S20-S21). Evidence supporting Re metallation was provided by NMR, UV-visible-nearIR (UV-vis-nIR), and FTIR spectroscopies. In the ¹H NMR spectrum, the aromatic peaks in **Re(bpy-TAz-PDI)** attributed to the bipyridine-moiety were deshielded relative to bpy-TAz-PDI, indicating incorporation of the electron-withdrawing Re metal center (Figures S5 – S6). The optical properties of the ligand and **Re(bpy-TAz-PDI)** were nearly identical, differing only in an additional MLCT band ($\lambda = 343$ nm) (Figures S22 – S23). By FTIR, three ν_{CO} stretches (1901, 1920, and 2024 cm⁻¹) emerged for **Re(bpy-TAz-PDI)** at similar frequencies to other reported Re(bpy) complexes (Figures S24 – S25).⁵¹

Single crystals suitable for connectivity mapping by X-ray diffraction crystallography were obtained by layering ethyl acetate on top of a CH₂Cl₂ solution of **Re(bpy-TAz-PDI)**. Weak diffraction and unresolvable twinning prevented the unambiguous confirmation of the single crystal structure. However, the connectivity map provided sufficient evidence that the Re metal center was chelated by the bpy-moiety of the bpy-TAz-PDI ligand (Figure S64). Moreover, bpy

and PDI can be oriented within reasonable π - π stacking distances, which would facilitate electron transfer (*vide infra*). The bulky PDI-moiety also occupied a space that was opposite of the axial chloride, suggesting that there are possible conformations in which PDI would not sterically hinder interactions between Re and CO₂ during electrocatalysis.^{52,53}

■ Electrochemistry

Cyclic voltammetry (CV) experiments performed on **Re(bpy-TAz-PDI)** displayed two oxidation and four reduction events (Figure 1; all reported redox processes were referenced relative to Fc^{+/0}). The first irreversible oxidation ($E_p = +1.01$ V) was attributed to the Re^{II/I} redox process.⁵⁴ The second quasi-reversible oxidation ($E_{1/2} = +1.15$ V), as well as the first and second reversible reduction events ($E_{1/2} = -1.19$ V and -1.48 V) can be assigned as PDI-centered redox events *via* direct comparison to the ligand (Figure S29). This type of electrochemical behavior is characteristic of N-annulated PDI materials.^{47,48,55} The third and fourth reductions ($E_{1/2} = -1.79$ V and $E_p = -2.20$ V, respectively) were analogous to other Re(bpy) complexes, such as Re(4,4'-dimethyl-2,2'-bipyridine)(CO)₃Cl [Re(dmbpy)] (Figure S31),²⁵ suggesting that these events correspond to the quasi-reversible $bpy^{0/\bullet-}$ and irreversible Re^{I/0} redox couples, respectively.²⁴⁻³⁸ Variable scan rate analysis of **Re(bpy-TAz-PDI)** under argon was in accordance with the Randles-Sevcik equation, indicating the dyad exhibits a diffusion-limited current response (Figure S32). It should be noted that the calculated diffusion coefficient for **Re(bpy-TAz-PDI)** ($D = 4 \times 10^{-6}$ cm² s⁻¹) was approximately half that of Re(dmbpy) ($D = 1 \times 10^{-5}$ cm² s⁻¹). These data, when combined with the absence of low-energy shoulders in the UV-vis-nIR spectrum of Re(bpy-TAz-PDI), indicate there is minimal PDI-related aggregation in solution.⁵⁶

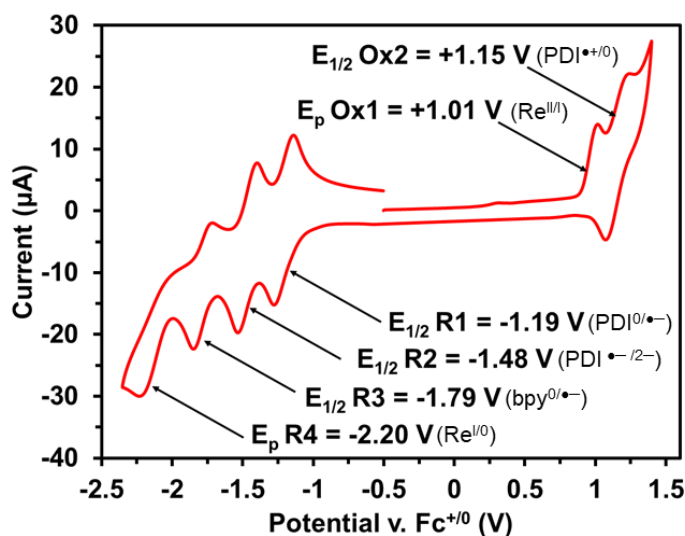


Figure 1. Assigned CV of Re(bpy-TAz-PDI) recorded at 100 mV/s, under argon in CH₂Cl₂ with 0.1 M TBAPF₆ supporting electrolyte (WE = glassy carbon, CE = Pt-wire, RE = Ag/AgCl, and Fc^{+/0} as internal reference standard)

Under an atmosphere of CO₂, the CV of **Re(bpy-TAz-PDI)** did not show significant current enhancement in either DMF or MeCN (Figure 2). Upon addition of either phenol (PhOH) or 2,2,2-trifluoroethanol (TFE), however, a large current enhancement plateau was observed at the fourth reduction event in both solvents. This type of current enhancement can often be indicative of electrocatalytic CO₂ reduction capabilities for Re(bpy)-derived complexes (Figure S34).^{24–38} Closer inspection of these CVs revealed minor changes to the PDI-based reduction events. Incrementally increasing the amount of TFE further caused the first reduction to change from fully reversible to quasi-reversible (Figures S30 and S34). At the same time, the second reduction event shifted to a less negative potential. These observations may be attributed to stabilization of the PDI imide oxygen atoms *via* either protonation of the PDI^{2–} imides and/or the proton-source stabilizing PDI^{2–} through hydrogen-bonding interactions.^{57,58} Perhaps the more significant change in these CVs was that the onset of CO₂ reduction current enhancement for **Re(bpy-TAz-PDI)** now occurred at the third reduction event (Figure 2B, inset). This shift in current enhancement suggests that PDI functionalization results in a lowering of the electrocatalytic CO₂ reduction overpotential, despite a lack of direct π -conjugation to Re(bpy). Notably, the onset of CO₂ current enhancement for **Re(bpy-TAz-PDI)** is 160 mV lower than the less conjugated naphthalimide-functionalized rhenium diimine complexes previously reported by Gobetto and co-workers.³⁸ These results clearly indicate that selection of chromophore (or conjugated unit) is critical to these hybrid systems, which opens a new and relevant approach for structurally engineering CO₂ conversion catalysts.

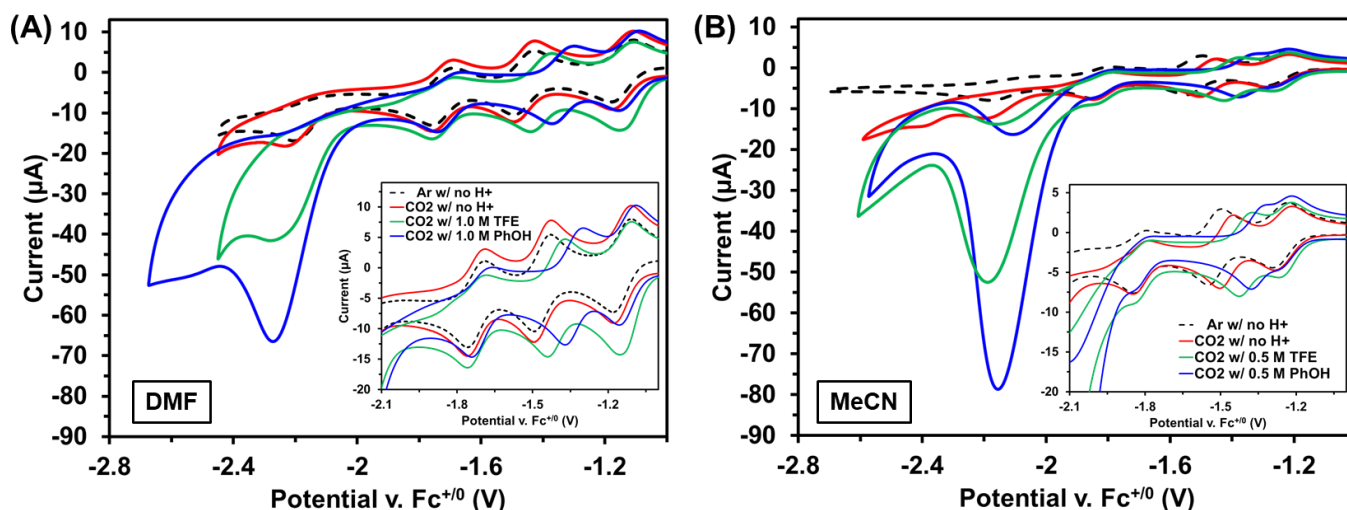


Figure 2. CVs of **Re(bpy-TAz-PDI)** (black) in DMF (A) and MeCN (B) comparing the effects of adding no proton source (red), TFE (green) and PhOH (blue) on catalytic current enhancement under atmospheric CO₂

By comparing the peak currents under CO₂ with 2.0 M TFE (i_{cat} ; Figure S33) relative to those measured under inert conditions (i_{p} ; Figures S31-S32), it is possible to estimate the observed non-electrochemical rate constant during CO₂ conversion (see SI for more details).²⁸ Using this $i_{\text{cat}}/i_{\text{p}}$ method (scan rate, $\nu = 25$ V/s), the observed catalytic rate constants (k_{obs}) for **Re(bpy-TAz-PDI)** were calculated to be 330 and 320 s⁻¹, for i_{cat} values measured in DMF at the third ($E_{1/2} =$

-1.79 V) and fourth ($E_p = -2.25$ V) reduction events, respectively. Under identical testing conditions, the k_{obs} for $\text{Re}(\text{dmbpy})$ was determined to be 1100 s^{-1} at the $\text{Re}^{I/0}$ reduction event ($E_p = -2.35$ V). The smaller k_{obs} for **Re(bpy-TAz-PDI)** may be attributed to either a lower nucleophilicity for CO_2 (given the dramatically lower overpotential)⁵⁹ or perhaps a difference in the electrocatalytic CO_2 reduction mechanism, relative to $\text{Re}(\text{dmbpy})$.⁶⁰ Regardless, these calculated k_{obs} can be used to generate a catalytic Tafel plot (Figure 3), which clearly emphasizes **Re(bpy-TAz-PDI)**'s ability to attain substantially higher catalytic activity than comparable non-PDI substituted $\text{Re}(\text{bpy})$ catalysts, at much lower overpotentials.^{28–30,61,62}

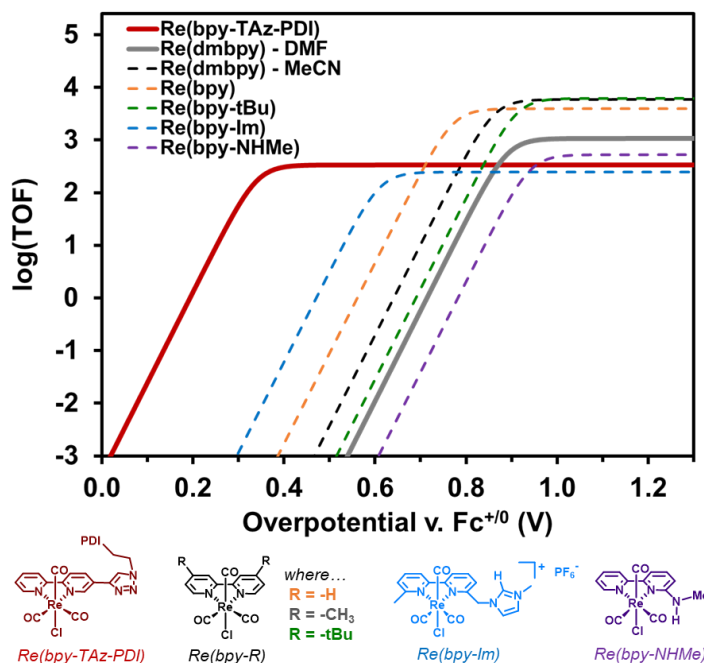


Figure 3. Catalytic Tafel plot comparing $\text{Re}(\text{bpy-TAz-PDI})$ (red) and $\text{Re}(\text{dmbpy})$ (gray) to other $\text{Re}(\text{bpy})$ derivatives. Solid lines indicate measurements were performed in DMF with 2 M TFE at $v = 25$ V/s. Dashed lines indicate $E_{\text{cat}/2}$ values were obtained from literature, where: all $\text{Re}(\text{bpy-R})$ experiments were performed in MeCN with 1 M PhOH at $v = 25$ V/s,²⁸ $\text{Re}(\text{bpy-Im})$ was evaluated in MeCN with 2.8 M water at $v = 3$ V/s,²⁹ and $\text{Re}(\text{bpy-NHMe})$ was measured in MeCN with 2 M TFE at $v = 0.1$ V/s.³⁰

■ Electro- and Photocatalytic CO_2 Reduction

To assess the CO_2 conversion activity of **Re(bpy-TAz-PDI)**, a series of controlled potential electrolysis (CPE) experiments were performed in a two-compartment cell, separated by fine glass frit (Figure S37).⁶² While the shift in onset potential and overall current enhancement for **Re(bpy-TAz-PDI)** redox events were more pronounced in MeCN, the complex's gradual precipitation from MeCN necessitated all CPE experiments to be performed in DMF. To benchmark the CPE setup, experiments were performed using $\text{Re}(\text{dmbpy})$ and TFE as a proton source. $\text{Re}(\text{dmbpy})$ was chosen as the benchmark catalyst because the installation of electron-donating groups on the bipyridine-moiety has been shown to significantly increase catalyst

activity, making this catalyst among the top-performing Re(bpy) derivatives when a proton-source, like TFE, is present.^{25,28}

At an applied potential where half of the maximum current enhancement was observed ($E_{\text{cat}/2} \approx -2.20$ V), Re(dmbpy) reached a TON_{CO} of 24 ± 1 , with a maximum Faradaic efficiency (FE) of 94 ± 2 %, over the 6-hour experiments (Figure 4). At the same applied potentials, **Re(bpy-TAz-PDI)** achieved a modest TON_{CO} of 13 ± 1 , with an FE of 87 ± 10 %. Prolonging the CPE experiments to 24 hours increased the TON_{CO} and decreased the FE_{CO} for both catalysts; Re(dmbpy) achieved a TON_{CO} of 49 and a FE of 61 %, while **Re(bpy-TAz-PDI)** reached a TON_{CO} of 34 and a FE of 79 % (Table S2). Other than H_2 , no other gaseous or liquid products were detected during CPE experiments.

Lowering the applied potential of these CPE experiments by 400 mV ($E = -1.80$ V), in order to better match the onset of CO_2 current enhancement for **Re(bpy-TAz-PDI)**, provided significantly different reactivity for the two complexes. The catalytic activity in Re(dmbpy) was effectively shut down at this applied potential, achieving a $\text{TON}_{\text{CO}} < 2$ and an $\text{FE} < 40$ % after 6 hours of CPE. At the same applied potential, the TON_{CO} and FE of **Re(bpy-TAz-PDI)** were both improved to 24 ± 4 and 92 ± 7 %, respectively. Evidently, lowering the applied potential was beneficial to the catalytic activity of **Re(bpy-TAz-PDI)**. Prolonged CPE experiments of 24 and 48 hours resulted in TON_{CO} of 54 and 84, while FE dropped to values between 42-47 % (Figure S40). As no significant amounts of H_2 (or liquid products) were detected during these prolonged CPE experiments, the apparent drop in FE can be partially attributed to a minor PDI-related degradation process (Figure S41).⁶³⁻⁶⁵

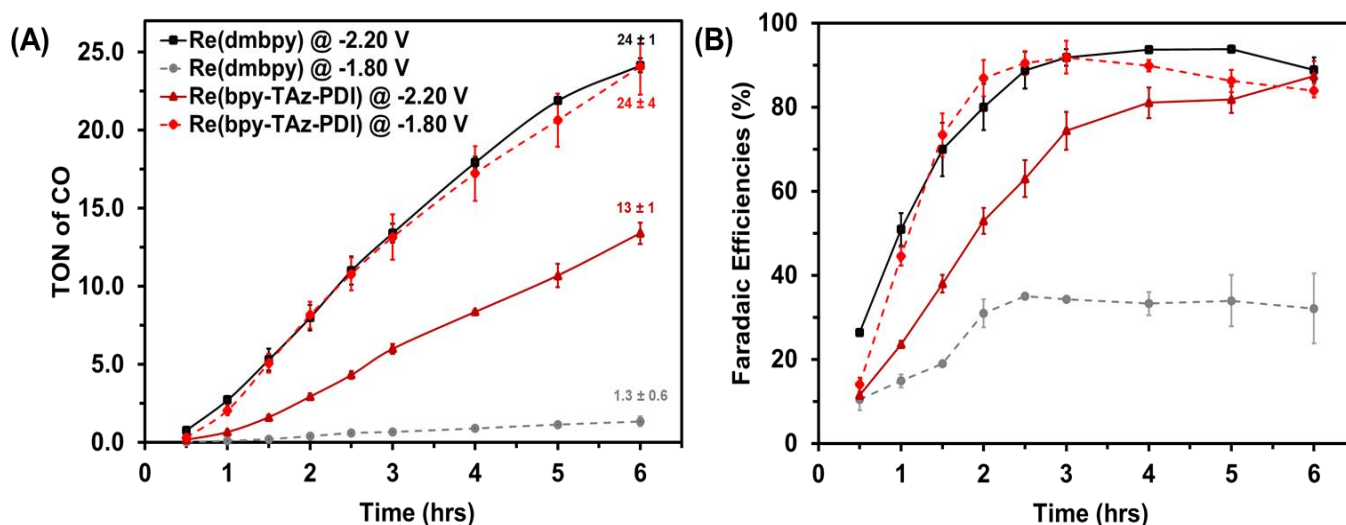


Figure 4. Comparing average TON_{CO} (A) and faradaic efficiencies of CO formation (B) achieved by Re(dmbpy) (grey) and Re(bpy-TAz-PDI) (red) during CPE experiments at different applied potentials ($E = -1.80$ V depicted with dashed lines and $E = -2.20$ V depicted with solid lines)

Additional CPE experiments were carried out to investigate key operating parameters of CO_2 conversion. Under dark conditions, **Re(bpy-TAz-PDI)** exhibited no difference in electrocatalytic

CO₂ reduction activity (Table S2, entry 14). Control experiments omitting CO₂, TFE, and/or **Re(bpy-TAz-PDI)** all produced H₂ as the only gaseous product (Table S2, entries 16-18). Also, pairing the benchmark catalyst Re(dmbpy) and the ligand bpy-TAz-PDI together did not lead to increased CO₂ reduction activity when CPE was performed at -1.80 V (Table S2, entry 19). Together, these experiments strongly suggest that the tether connecting PDI and the Re(bpy)-moiety is essential to the electron transfer process. Moreover, the electron-transfer occurring between the PDI and the Re(bpy)-moiety is not light-mediated but is likely proton-coupled. However, it should be noted that at an applied potential of -1.80 V, the irradiation of **Re(bpy-TAz-PDI)** with blue light ($\lambda = 470 \pm 30$ nm) was found to enhance the rate CO production (Entry 15; TON_{co} = 35, after 6 hours). Further investigation is required to understand the influence of blue light on CO₂ conversion, as the catalytic enhancement may be attributed to photo-assisted CO cleavage^{66,67} and/or photoelectrochemical CO₂ reduction (Figure S42).^{68,69}

Expanding upon these observations, the photocatalytic CO₂ reduction capabilities of **Re(bpy-TAz-PDI)** were assessed by employing the same blue light source, as the use of UV light is known to cause deactivation and/or degradation of Re(bpy) catalysts.^{70,71} While the emission spectrum of the blue light does not perfectly match the λ_{max} of **Re(bpy-TAz-PDI)** (Figure S28), the light source is sufficiently energetic to photoexcite the PDI chromophore. The catalyst (65 μM) was dissolved in a (5:1) mixture of DMF : triethanolamine (TEOA), where TEOA simultaneously functioned as the proton source and the sacrificial electron donor.⁷² Using these conditions, **Re(bpy-TAz-PDI)** produced CO (TON_{co} = 8.4 ± 0.9) after 18 hours of irradiation, with a high selectivity of ~17:1 CO:H₂ (Table S3). Under the same conditions, Re(dmbpy) achieved a TON_{co} of 1.9 ± 0.2 after 18 hours, where CO was the only observable gaseous product. Adding TFE to the reaction mixture caused suppressed formation of both CO and H₂ for **Re(bpy-TAz-PDI)**, whilst Re(dmbpy) experienced complete deactivation in photocatalytic CO₂ reduction. The addition of TFE may be hindering the reaction dynamics between TEOA and the catalyst.^{72,73} In the absence of light, CO₂, or TEOA, neither catalyst produced any CO or H₂. We may therefore attribute the over 4-fold enhanced photocatalytic activity for **Re(bpy-TAz-PDI)** to the better overlap between the absorbance profile of the catalyst and the emission spectrum of the irradiation source. This result again emphasizes the promise of the hybrid supramolecular dyad design approach.

■ Mechanistic Investigation

During the first 30 minutes of all CPE experiments with **Re(bpy-TAz-PDI)**, it was observed that the color of the bulk solution progressed from orange to dark blue. Inspecting the current vs. time plot (Figure S38A), current passed over this induction period rapidly decayed and minimal CO was produced. However, after this catalyst equilibration period, there was a sudden and sustained increase in passed current (Figure S38B), accompanied by a steady production of CO. Thus, to better probe the electrocatalytic CO₂ reduction mechanism of **Re(bpy-TAz-PDI)**, a series of UV-vis-nIR SEC, FTIR SEC, and chemical reduction experiments were performed.

By UV-vis-nIR SEC, applying a potential of -1.2 V (R1) caused a color transition from orange to green, which was accompanied by a bathochromic shift in the wavelength of maximum absorption (λ_{max}) from 521 nm to 690 nm (Figure 5A). The characteristic PDI vibronic fine-structure simultaneously decreased and new absorption bands in the near-IR region emerged at

780, 840, and 925 nm. This same color change was observed with bpy-TAz-PDI (Figure S35), confirming the assignment of a $\text{PDI}^{0/\bullet-}$ reduction.⁷⁴ Decreasing the potential to -1.5 V (R2) caused the solution to progress from green to blue. During this color change, the λ_{max} at 690 nm partially decreased while the absorption fine-structure in the near-IR essentially disappeared. At the same time, two strong absorption bands appeared at 617 and 652 nm. Once again, the same transition was observed with the ligand, confirming the color change was due to $\text{PDI}^{\bullet-/2-}$ reduction.⁵⁸ Further decreasing the applied potential to -1.8 V (R3) did not result in any significant changes to the SEC spectra of **Re(bpy-TAz-PDI)** as the optical contribution from $\text{bpy}^{0/\bullet-}$ reduction would be minor.^{70,71} All electrochemically generated species were also detected when UV-vis-nIR SEC experiments were performed with TFE (Figure S36B).

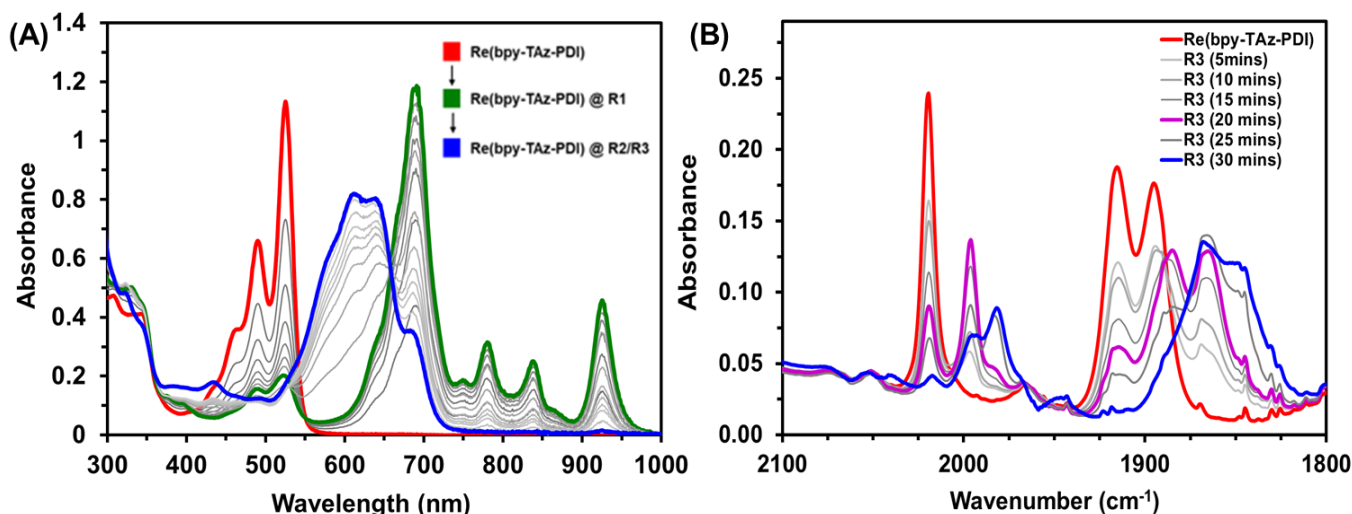


Figure 5. UV-vis-nIR SEC (A) and FTIR SEC (B) absorbance spectra of **Re(bpy-TAz-PDI)**. Spectra were obtained by holding constant applied potentials, where R1, R2, and R3 = -1.2, -1.5, and -1.8 V vs. $\text{Fc}^{+/0}$, respectively. All experiments were performed under argon in DMF with 0.1 M TBAPF₆ supporting electrolyte (WE = Pt-mesh, CE = Pt-wire, pseudo-RE = Ag-wire)

By FTIR SEC, applied potentials of R1 and R2 did not alter the ν_{co} of **Re(bpy-TAz-PDI)**. These data suggest that excess charge was therefore located mostly on the PDI-moiety, with minimal delocalization onto the Re(bpy)-moiety. Increasing the applied potential to R3, however, caused noticeable transitions in the ν_{co} (Figure 5B). Similar to the systems reported by Kubiak and co-workers,^{51,52} the $\text{bpy}^{0/\bullet-}$ reduction can be characterized by a shift to lower wavenumbers for ν_{co} to 1861, 1884, 1995 cm^{-1} . Over time, these ν_{co} further shifted to 1845, 1866, and 1980 cm^{-1} , indicating that the electron has delocalized between bpy and Re, eventually shifting electron-density towards the metal center.⁵⁴ During this equilibration process, it is proposed that a formal $\text{Re}^{\text{I/0}}$ reduction occurs, leading to the displacement of the axial chloride ligand from Re.

To confirm the assignments made by UV-vis-nIR SEC and FTIR SEC, the reduced **Re(bpy-TAz-PDI)** species were independently synthesized (see SI for full experimental details). Each chemically reduced product was characterized by ¹H NMR (Figures S10-S13), as well as UV-vis-nIR and FTIR absorption spectroscopies (Figure S26 and S27). The optical and magnetic

properties of all three anionic **Re(bpy-TAz-PDI)** complexes correlated well with the corresponding electrochemical processes determined by SEC. As expected, the singly and triply reduced complexes exhibited paramagnetic ^1H NMR spectra, while the doubly reduced complex possessed a diamagnetic ^1H NMR spectrum.⁵⁷ The aromatic resonances of this chemically reduced product were shifted slightly upfield relative to the **Re(bpy-TAz-PDI)**, suggesting more electron-donating in character of the PDI-moiety.

The chemically reduced **Re(bpy-TAz-PDI)** species were also investigated using electron paramagnetic resonance (EPR) spectroscopy. As expected for a PDI-based organic radical, the singly reduced species exhibited an axial resonance with $g_{\text{per}} = 2.0009$, $g_{\text{par}} = 2.0037$, and no observable hyperfine splitting (Figure S14).^{75,76} The EPR spectrum of the triply reduced species displayed a small hyperfine coupling between the bpy-based radical and the rhenium metal center [$a(^{183,185}\text{Re}) = 1.65$ mT] (Figure S15), which would only be observed if line-broadening contributions from $^{35,37}\text{Cl}$ were removed. Previous interpretations of related paramagnetic **Re(bpy)** complexes have ascribed this type of coupling pattern to an equilibrium process between the chloro-associated (6-coordinate) and chloro-dissociated (5-coordinate) species.^{77,78}

To further probe the CO_2 reduction mechanism, a DFT-based investigation was undertaken. All calculations were performed using the M06 functional,⁷⁹ the 6-31G(d,p) Pople basis set for all non-metal elements,^{80–82} and the LANL2DZ basis set for rhenium^{83–85} (see SI Section VIII for more details). All optimized geometries described herein were determined to be minima on the potential energy surface through normal mode analyses. The DFT-optimized structure of ground-state **Re(bpy-TAz-PDI)** showed excellent correlation with the single-crystal X-ray diffraction connectivity map (Figure S64). We note that in the optimized ground-state geometry of the complex that the PDI and **Re(bpy-TAz)** are near each other, with the alkyl arm folded to bring the moieties in proximity. Attempts to optimize the geometry of **Re(bpy-TAz-PDI)** starting from an extended conformation were unable to deliver an optimized structure, confirming intramolecular folding is important to this system. Optimized geometries were also determined for each constituent component of **Re(bpy-TAz-PDI)**, namely **Re(bpy-TAz)** and N-annulated PDI, to facilitate the construction of a molecular orbital (MO) diagram (Figure S43), which corresponded well to the assigned redox processes derived from the electrochemical measurements (Figure 1). The localized natures of the frontier MOs reveal that the two fragments are nearly electronically isolated, which is reasonable considering the system is not through conjugated.

We next turned our attention to the natures of the electronic states in the proposed reaction cycle (Figure 6). Emphasis was placed on the optimized geometries, frontier MOs, and spin-density maps to demonstrate the distributions of the electron spin in these states. From the ground-state **Re^I(bpy-TAz-PDI)⁰** (Figure 6A), one electron can be added to the system without significantly affecting the molecular geometry of the complex (Figure S44). The electron spin-density for the doublet state of **Re^I(bpy-TAz-PDI)^{•−}** is localized on PDI, as one may expect, correlating well with the calculated highest occupied α -spin orbital (HO α O; Figure S45).

Adding a second electron to the system to generate **Re^I(bpy-TAz-PDI)^{2−}** also did not greatly change the molecular geometry (Figure S46). Both the singlet and triplet states of **Re^I(bpy-TAz-PDI)^{2−}** were considered based on the lowest unoccupied α -spin orbital (LU α O) and the lowest unoccupied β -spin orbital (LU β O) of **Re^I(bpy-TAz-PDI)^{•−}**. It should be noted that an

unrestricted open-shell calculation for $\text{Re}^{\text{I}}(\text{bpy-TAz-PDI})^{2-}$ converged with all electrons paired on PDI, and the energy difference between the singlet and triplet states is small (~ 0.2 eV). The spin-density of the triplet state of $\text{Re}^{\text{I}}(\text{bpy-TAz-PDI})^{2-}$ is clearly delocalized across the entire complex, where Re-CO anti-bonding interactions are observed (Figure S47). The HOMO of the singlet state, however, showed no Re-CO anti-bonding character (Figure S48). Given that the isolated doubly reduced product was diamagnetic and no $\Delta\nu_{\text{CO}}$ was observed in our FTIR SEC experiments at applied potentials of R2, it is highly likely that $\text{Re}^{\text{I}}(\text{bpy-TAz-PDI})^{2-}$ favors the singlet state.

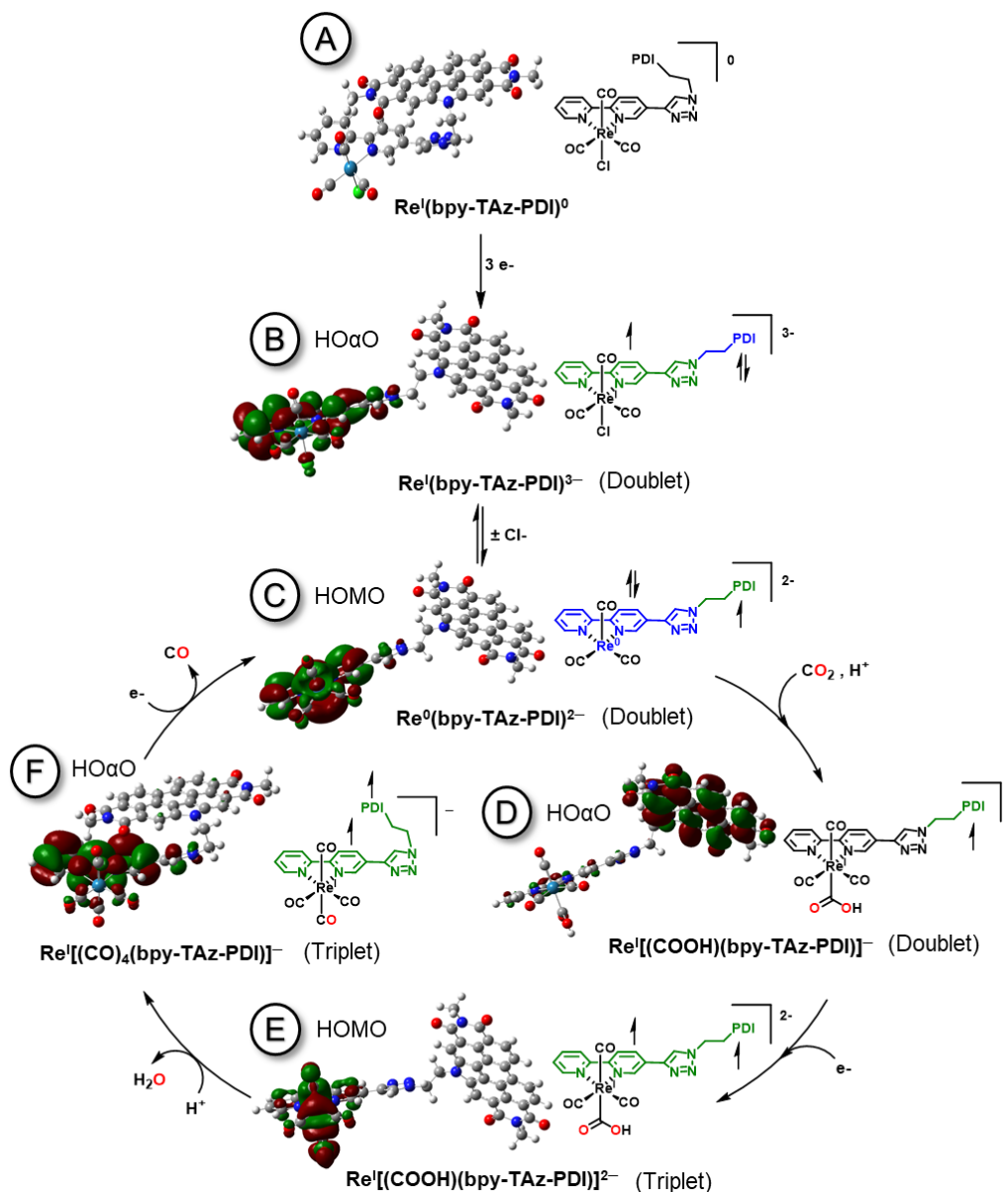


Figure 6. Optimized geometries and relevant HOMO or $\text{HO}\alpha\text{O}$ for the tentative proposed electrocatalytic CO_2 cycle of $\text{Re}(\text{bpy-TAz-PDI})$, determined at the M06/6-31G(d,p)/LANL2DZ level of theory. Black, green, or blue coloration of the $\text{Re}(\text{bpy-TAz})$ and PDI structural moieties indicate the presence of zero, one, or two additional electrons, respectively.

A further one-electron reduction of the complex to **Re^I(bpy-TAz-PDI)³⁻** results in a substantial geometric rearrangement (Figures 6B and S49). Instead of PDI being folded over the Re(bpy-TAz)-moiety, the alkyl arm extends to separate the PDI and Re(bpy-TAz) moieties. Looking at the MOs of the doublet state of **Re^I(bpy-TAz-PDI)³⁻**, the HOMO is PDI-localized, while the HO α O is exclusively Re(bpy-TAz) in character (Figure S50). The extended geometry of the **Re^I(bpy-TAz-PDI)³⁻** likely results from electrostatic repulsion between the negatively charged PDI²⁻ and Re(bpy-TAz)^{•-} moieties.

From the FTIR SEC data, **Re^I(bpy-TAz-PDI)³⁻** was observed to undergo dissociation of the axial chloride-ligand to generate the five-coordinate **Re⁰(bpy-TAz-PDI)²⁻** (Figure 6C). Geometry optimization calculations performed on the five-coordinate **Re⁰(bpy-TAz-PDI)²⁻** species showed that PDI was still in an extended state relative to the Re(bpy-TAz)-moiety (Figure S51). Examining the MOs of this doublet state of **Re⁰(bpy-TAz-PDI)²⁻**, the HO α O is PDI-centered, while the HOMO is distributed over the Re(bpy-TAz)-moiety (Figure S52) in a similar way to the system reported by Kubiak and co-workers.⁸⁶ These MOs imply that an electron was transferred from the PDI²⁻ electron-reservoir to the 5-coordinate Re(bpy-TAz). Such an electron transfer process may have occurred either by a through-bond mechanism similar to Ru^{II}-Re^I systems³²⁻³⁴ or by a through-space mechanism that was facilitated by the orientation of the chromophore.³⁶

Experimentally there was no direct evidence of the catalyst adopting either a Re⁰(bpy-TAz)^{•-} or a Re^I conformation.^{51,52,87,88} We note that attempts to reconcile experimental and theoretical data on **Re⁰(bpy-TAz-PDI)²⁻** via calculations with the SMD implicit solvation model,⁸⁹ explicit inclusion of DMF in the coordination sphere of Re(bpy-TAz) (Figure S53), or explicit protonation of the PDI²⁻ imide oxygens (Figure S54) each resulted in the same MO and spin-density descriptions. While the electronic configuration for the calculated **Re⁰(bpy-TAz-PDI)²⁻** species was not detected experimentally, the possibility of an electron-transfer that results in a Re⁰(bpy-TAz)^{•-} conformation cannot be precluded either. And based on the symmetry of the HOMO being appropriate for a proton-mediated, two-electron nucleophilic attack on CO₂, this species is likely a key intermediate in the catalytic cycle.⁸⁶

Since CO was the major product of CPE experiments, the intermediate formed following CO₂ activation would most likely be **Re^I[(COOH)(bpy-TAz-PDI)]⁻** (Figure 6D). The optimized geometry of this intermediate still demonstrated an extended bpy-TAz-PDI ligand and the spin-density for the doublet state was largely located on PDI (Figure S55). Subsequent reduction of this intermediate to form **Re^I[(COOH)(bpy-TAz-PDI)]²⁻** slightly altered the molecular geometry (Figures 6E and S57A). While both the singlet and triplet states of **Re^I[(COOH)(bpy-TAz-PDI)]²⁻** were considered, the triplet state is ~0.4 eV more stable. The spin-density for the triplet state of **Re^I[(COOH)(bpy-TAz-PDI)]²⁻** shows significant electron-delocalization across the entire bpy-TAz-PDI ligand, consistent with MO contributions of α -spin electrons from both the HO α O-1 and the HO α O (Figure S58). Moreover, appreciable back-bonding interactions were observed between Re and COOH, which could facilitate the proton-assisted displacement of H₂O, en route to forming **Re^I[(CO)₄(bpy-TAz-PDI)]⁻**.⁸⁷

The optimized geometry of **Re^I[(CO)₄(bpy-TAz-PDI)]⁻** shows that PDI re-folds over the Re(bpy-TAz)-moiety (Figure S60). Here, the triplet state is more energetically favorable (by ~0.5

eV) than the corresponding spin-paired singlet state. The spin-density map of the triplet state, containing both HO α O-1 and HO α O (Figure S61), is suggestive of extensive electron-delocalization. Moreover, there were still back-bonding interactions between Re and CO in the HO α O, which could assist with the displacement of CO. Adding another electron to the system, generating **Re^I[(CO)₄(bpy-TAz-PDI)]²⁻**, dramatically impacts the molecular geometry (Figure S62). Not only was twisting observed in the bpy-TAz ligand, there is also a distinct lengthening in one of the axial Re-CO bonds (Figure S62C). The spin-density of this *pseudo* 5-coordinate species is entirely on PDI, suggesting the electron was added to the LU β O of the preceding species. Furthermore, the spin-density of **Re^I[(CO)₄(bpy-TAz-PDI)]²⁻** was similar to that of 5-coordinate **Re⁰(bpy-TAz-PDI)²⁻**, indicating the regeneration of this active species.

Combining these computational studies, along with the CPE, SEC and chemical reduction experiments, a tentative mechanism can be proposed (outlined in Figure 6). Following the formal three-electron reduction of **Re(bpy-TAz-PDI)**, the third electron equilibrates between bpy^{0•-} and Re^{I/0} to liberate the axial chloro-ligand and open a site for CO₂ activation and reduction. In a similar manner to the system reported by Li *et. al.*,²⁰ losing the chloro-ligand triggers a shift in the electron-density from the strongly electron-donating PDI²⁻ electron-reservoir towards the Re(bpy)-moiety. This shift of electron-density allows **Re(bpy-TAz-PDI)** to reduce CO₂, in a proton-coupled electron transfer process, emphasizing the cooperativity between the catalyst and the electron-reservoir. By analogy to other Re(bpy)-based systems,^{51,52,87,88} **Re(bpy-TAz-PDI)** must undergo a successive reduction and proton-assisted displacement of H₂O to generate a tetracarbonyl species. This tetracarbonyl species would undergo a subsequent reduction to liberate CO and thus regenerate the electrocatalytically active 5-coordinate species.

■ Conclusion

In conclusion, we have reported the synthesis and characterization of a PDI photosensitized Re(bpy) supramolecular dyad. In the presence of CO₂ and a proton source, **Re(bpy-TAz-PDI)** electrocatalytically reduced CO₂ at an applied potential 400 mV lower than the benchmark catalyst, Re(dmbpy). Moreover, **Re(bpy-TAz-PDI)** was found to reduce CO₂ photocatalytically with 4-fold higher activity, relative to Re(dmbpy). Through a combination of CPE, UV-vis-nIR SEC, FTIR SEC, and chemical reduction experiments, it was elucidated that the PDI-moiety acted as an electron-reservoir. This electron-reservoir effect allowed for enhanced catalytic CO₂ reduction activity at significantly lower overpotentials. DFT studies on relevant catalytic intermediates revealed that: (1) the PDI works cooperatively with the Re(bpy)-moiety to manage electrons, and (2) the geometric orientation between PDI and the Re(bpy)-moiety is important to the electron-transfer dynamics for **Re(bpy-TAz-PDI)** during CO₂ reduction, where an extended conformation was favorable. These results could help guide future molecular design by thoughtfully tailoring both the chromophore (electron reservoir) and metal-ligand complex. Research is currently ongoing to understand the impact of tether-length, as well as light irradiation on electro- and photocatalytic activity in these **Re(bpy-TAz-PDI)** systems.

This work clearly demonstrates the utility of organic chromophore electron reservoirs to effectively lower the overpotential required for CO₂ reduction for Re(bpy) complexes. Operating these molecular electrocatalysts at lower overpotentials not only decreases the required energetic input, but it may also improve system longevity.^{38,90} Moreover, these chromophores may serve as

useful electrode anchoring units (i.e. through π -stacking), a strategy that is well-known to simultaneously increase catalyst activity and longevity.^{13–19} Combining these concepts of diminished overpotential and improved catalyst stability together may afford the prospect of developing industrially feasible devices.^{2,20–23} Given the abundance of photoactive π -conjugated chromophores, an opportunity exists to systematically synthesize a variety of supramolecular dyad CO₂ reduction catalysts that have tailored properties to maximize performance.

■ Supporting Information

Experimental details; MALDI-TOF MS; elemental analysis; NMR, UV-vis-nIR, FTIR, and SEC spectra; cyclic voltammograms; CPE data; computational methods/data; crystallographic methods/data (PDF)

■ Acknowledgements

GCW acknowledges the Canada Research Chairs Program, CFI JELF (34102), NSERC DG (2019-04392), and the University of Calgary. WEP acknowledges the Canada Research Chairs Program. JK acknowledges Alberta Graduate Excellence Scholarship (AGES) and NSERC CGS-D scholarship programs. This research was undertaken thanks in part to funding from the Canada First Research Excellence Fund (CFREF). CR and KR acknowledge funding by the Research Corporation for Science Advancement (RCSA) Cottrell Scholars program (Award No. 24432); computing resources on the Lipscomb High Performance Computing Cluster were provided by the University of Kentucky Information Technology Department and the Center for Computational Sciences (CCS).

■ References

- (1) Keith, D. W.; Holmes, G.; Angelo, D. S.; Heidel, K. A Process for Capturing CO₂ from the Atmosphere. *Joule* **2018**, 2 (8), 1573–1594. <https://doi.org/10.1016/j.joule.2018.05.006>.
- (2) Luna, P. D.; Hahn, C.; Higgins, D.; Jaffer, S. A.; Jaramillo, T. F.; Sargent, E. H. What Would It Take for Renewably Powered Electrosynthesis to Displace Petrochemical Processes? *Science* **2019**, 364 (6438). <https://doi.org/10.1126/science.aav3506>.
- (3) Windle, C. D.; Perutz, R. N. Advances in Molecular Photocatalytic and Electrocatalytic CO₂ Reduction. *Coord. Chem. Rev.* **2012**, 256 (21), 2562–2570. <https://doi.org/10.1016/j.ccr.2012.03.010>.
- (4) Costentin, C.; Robert, M.; Savéant, J.-M. Catalysis of the Electrochemical Reduction of Carbon Dioxide. *Chem. Soc. Rev.* **2013**, 42, 2423–2436. <https://doi.org/10.1039/C2CS35360A>.
- (5) Zhou, Y.; Che, F.; Liu, M.; Zou, C.; Liang, Z.; Luna, P. D.; Yuan, H.; Li, J.; Wang, Z.; Xie, H.; Li, H.; Chen, P.; Bladt, E.; Quintero-Bermudez, R.; Sham, T.-K.; Bals, S.; Hofkens, J.; Sinton, D.; Chen, G.; Sargent, E. H. Dopant-Induced Electron Localization Drives CO₂ Reduction to C₂ Hydrocarbons. *Nat. Chem.* **2018**, 1. <https://doi.org/10.1038/s41557-018-0092-x>.
- (6) Kibria, M. G.; Edwards, J. P.; Gabardo, C. M.; Dinh, C.-T.; Seifitokaldani, A.; Sinton, D.; Sargent, E. H. Electrochemical CO₂ Reduction into Chemical Feedstocks: From Mechanistic Electrocatalysis Models to System Design. *Adv. Mater.* **2019**, 31 (31), 1807166. <https://doi.org/10.1002/adma.201807166>.

- (7) Nam, D.-H.; De Luna, P.; Rosas-Hernández, A.; Thevenon, A.; Li, F.; Agapie, T.; Peters, J. C.; Shekhah, O.; Eddaoudi, M.; Sargent, E. H. Molecular Enhancement of Heterogeneous CO₂ Reduction. *Nat. Mater.* **2020**, *19* (3), 266–276. <https://doi.org/10.1038/s41563-020-0610-2>.
- (8) Zheng, T.; Jiang, K.; Wang, H. Recent Advances in Electrochemical CO₂-to-CO Conversion on Heterogeneous Catalysts. *Adv. Mater.* **2018**, *30* (48), 1802066. <https://doi.org/10.1002/adma.201802066>.
- (9) Zheng, T.; Jiang, K.; Ta, N.; Hu, Y.; Zeng, J.; Liu, J.; Wang, H. Large-Scale and Highly Selective CO₂ Electrocatalytic Reduction on Nickel Single-Atom Catalyst. *Joule* **2019**, *3* (1), 265–278. <https://doi.org/10.1016/j.joule.2018.10.015>.
- (10) Xia, C.; Zhu, P.; Jiang, Q.; Pan, Y.; Liang, W.; Stavitski, E.; Alshareef, H. N.; Wang, H. Continuous Production of Pure Liquid Fuel Solutions via Electrocatalytic CO₂ Reduction Using Solid-Electrolyte Devices. *Nat. Energy* **2019**, *4* (9), 776–785. <https://doi.org/10.1038/s41560-019-0451-x>.
- (11) Takeda, H.; Cometto, C.; Ishitani, O.; Robert, M. Electrons, Photons, Protons and Earth-Abundant Metal Complexes for Molecular Catalysis of CO₂ Reduction. *ACS Catal.* **2017**, *7*, 70–88. <https://doi.org/10.1021/acscatal.6b02181>.
- (12) Francke, R.; Schille, B.; Roemelt, M. Homogeneously Catalyzed Electroreduction of Carbon Dioxide—Methods, Mechanisms, and Catalysts. *Chem. Rev.* **2018**, *118* (9), 4631–4701. <https://doi.org/10.1021/acs.chemrev.7b00459>.
- (13) Oh, S.; Gallagher, J. R.; Miller, J. T.; Surendranath, Y. Graphite-Conjugated Rhenium Catalysts for Carbon Dioxide Reduction. *J. Am. Chem. Soc.* **2016**, *138* (6), 1820–1823. <https://doi.org/10.1021/jacs.5b13080>.
- (14) Hu, X.-M.; Rønne, M. H.; Pedersen, S. U.; Skrydstrup, T.; Daasbjerg, K. Enhanced Catalytic Activity of Cobalt Porphyrin in CO₂ Electroreduction upon Immobilization on Carbon Materials. *Angew. Chem.* **2017**, *129* (23), 6568–6572. <https://doi.org/10.1002/ange.201701104>.
- (15) Reuillard, B.; Ly, K. H.; Rosser, T. E.; Kuehnle, M. F.; Zebger, I.; Reisner, E. Tuning Product Selectivity for Aqueous CO₂ Reduction with a Mn(Bipyridine)-Pyrene Catalyst Immobilized on a Carbon Nanotube Electrode. *J. Am. Chem. Soc.* **2017**, *139* (41), 14425–14435. <https://doi.org/10.1021/jacs.7b06269>.
- (16) Orchanian, N. M.; Hong, L. E.; Marinescu, S. C. Immobilized Molecular Wires on Carbon-Cloth Electrodes Facilitate CO₂ Electrolysis. *ACS Catal.* **2019**, *9* (10), 9393–9397. <https://doi.org/10.1021/acscatal.9b03134>.
- (17) Orchanian, N. M.; Hong, L. E.; Skrainka, J. A.; Esterhuizen, J. A.; Popov, D. A.; Marinescu, S. C. Surface-Immobilized Conjugated Polymers Incorporating Rhenium Bipyridine Motifs for Electrocatalytic and Photocatalytic CO₂ Reduction. *ACS Appl. Energy Mater.* **2019**, *2* (1), 110–123. <https://doi.org/10.1021/acsaem.8b01745>.
- (18) Willkomm, J.; Bertin, E.; Atwa, M.; Lin, J.-B.; Birss, V.; Piers, W. E. Grafting of a Molecular Rhenium CO₂ Reduction Catalyst onto Colloid-Imprinted Carbon. *ACS Appl. Energy Mater.* **2019**, *2* (4), 2414–2418. <https://doi.org/10.1021/acsaem.9b00216>.
- (19) Sinha, S.; Sonea, A.; Shen, W.; Hanson, S. S.; Warren, J. J. Heterogeneous Aqueous CO₂ Reduction Using a Pyrene-Modified Rhenium(I) Diimine Complex. *Inorg. Chem.* **2019**, *58* (16), 10454–10461. <https://doi.org/10.1021/acs.inorgchem.9b01060>.
- (20) Qiao, X.; Li, Q.; Schaagaard, R. N.; Noffke, B. W.; Liu, Y.; Li, D.; Liu, L.; Raghavachari, K.; Li, L. Well-Defined Nanographene–Rhenium Complex as an Efficient Electrocatalyst and Photocatalyst for Selective CO₂ Reduction. *J. Am. Chem. Soc.* **2017**, *139* (11), 3934–3937. <https://doi.org/10.1021/jacs.6b12530>.
- (21) Wang, M.; Torbensen, K.; Salvatore, D.; Ren, S.; Joulié, D.; Dumoulin, F.; Mendoza, D.; Lassalle-Kaiser, B.; Işci, U.; Berlinguette, C. P.; Robert, M. CO₂ Electrochemical Catalytic Reduction with a Highly Active Cobalt Phthalocyanine. *Nat. Commun.* **2019**, *10* (1), 1–8. <https://doi.org/10.1038/s41467-019-11542-w>.

- (22) Ren, S.; Joulié, D.; Salvatore, D.; Torbensen, K.; Wang, M.; Robert, M.; Berlinguette, C. P. Molecular Electrocatalysts Can Mediate Fast, Selective CO₂ Reduction in a Flow Cell. *Science* **2019**, 365 (6451), 367–369. <https://doi.org/10.1126/science.aax4608>.
- (23) Salvatore, D.; Berlinguette, C. P. Voltage Matters When Reducing CO₂ in an Electrochemical Flow Cell. *ACS Energy Lett.* **2020**, 5 (1), 215–220. <https://doi.org/10.1021/acsenenergylett.9b02356>.
- (24) Hawecker, J.; Lehn, J.-M.; Ziesel, R. Electrocatalytic Reduction of Carbon Dioxide Mediated by Re(Bipy)(CO)₃Cl (Bipy = 2,2'-Bipyridine). *J. Chem. Soc. Chem. Commun.* **1984**, 0 (6), 328–330. <https://doi.org/10.1039/C39840000328>.
- (25) Smieja, J. M.; Kubiak, C. P. Re(Bipy-TBu)(CO)₃Cl—improved Catalytic Activity for Reduction of Carbon Dioxide: IR-Spectroelectrochemical and Mechanistic Studies. *Inorg. Chem.* **2010**, 49 (20), 9283–9289. <https://doi.org/10.1021/ic1008363>.
- (26) Sampson, M. D.; Nguyen, A. D.; Grice, K. A.; Moore, C. E.; Rheingold, A. L.; Kubiak, C. P. Manganese Catalysts with Bulky Bipyridine Ligands for the Electrocatalytic Reduction of Carbon Dioxide: Eliminating Dimerization and Altering Catalysis. *J. Am. Chem. Soc.* **2014**, 136, 5460–5471. <https://doi.org/10.1021/ja501252f>.
- (27) Machan, C. W.; Yin, J.; Chabolla, S. A.; Gilson, M. K.; Kubiak, C. P. Improving the Efficiency and Activity of Electrocatalysts for the Reduction of CO₂ through Supramolecular Assembly with Amino Acid-Modified Ligands. *J. Am. Chem. Soc.* **2016**, 138 (26), 8184–8193. <https://doi.org/10.1021/jacs.6b03774>.
- (28) Clark, M. L.; Cheung, P. L.; Lessio, M.; Carter, E. A.; Kubiak, C. P. Kinetic and Mechanistic Effects of Bipyridine (Bpy) Substituent, Labile Ligand, and Brønsted Acid on Electrocatalytic CO₂ Reduction by Re(Bpy) Complexes. *ACS Catal.* **2018**, 8 (3), 2021–2029. <https://doi.org/10.1021/acscatal.7b03971>.
- (29) Sung, S.; Kumar, D.; Gil-Sepulcre, M.; Nippe, M. Electrocatalytic CO₂ Reduction by Imidazolium-Functionalized Molecular Catalysts. *J. Am. Chem. Soc.* **2017**, 139 (40), 13993–13996. <https://doi.org/10.1021/jacs.7b07709>.
- (30) Hellman, A. N.; Haiges, R.; Marinescu, S. C. Rhenium Bipyridine Catalysts with Hydrogen Bonding Pendant Amines for CO₂ Reduction. *Dalton Trans.* **2019**, 48 (38), 14251–14255. <https://doi.org/10.1039/C9DT02689D>.
- (31) Haviv, E.; Azaiza-Dabbah, D.; Carmieli, R.; Avram, L.; Martin, J. M. L.; Neumann, R. A Thiourea Tether in the Second Coordination Sphere as a Binding Site for CO₂ and a Proton Donor Promotes the Electrochemical Reduction of CO₂ to CO Catalyzed by a Rhenium Bipyridine-Type Complex. *J. Am. Chem. Soc.* **2018**, 140 (39), 12451–12456. <https://doi.org/10.1021/jacs.8b05658>.
- (32) Sahara, G.; Ishitani, O. Efficient Photocatalysts for CO₂ Reduction. *Inorg. Chem.* **2015**, 54, 5096–5104. <https://doi.org/10.1021/ic502675a>.
- (33) Koike, K.; C. Grills, D.; Tamaki, Y.; Fujita, E.; Okubo, K.; Yamazaki, Y.; Saigo, M.; Mukuta, T.; Onda, K.; Ishitani, O. Investigation of Excited State, Reductive Quenching, and Intramolecular Electron Transfer of Ru(II)–Re(I) Supramolecular Photocatalysts for CO₂ Reduction Using Time-Resolved IR Measurements. *Chem. Sci.* **2018**, 9 (11), 2961–2974. <https://doi.org/10.1039/C7SC05338J>.
- (34) Yamazaki, Y.; Ohkubo, K.; Saito, D.; Yatsu, T.; Tamaki, Y.; Tanaka, S.; Koike, K.; Onda, K.; Ishitani, O. Kinetics and Mechanism of Intramolecular Electron Transfer in Ru(II)–Re(I) Supramolecular CO₂–Reduction Photocatalysts: Effects of Bridging Ligands. *Inorg. Chem.* **2019**, 58 (17), 11480–11492. <https://doi.org/10.1021/acs.inorgchem.9b01256>.
- (35) Windle, C. D.; George, M. W.; Perutz, R. N.; Summers, P. A.; Sun, X. Z.; Whitwood, A. C. Comparison of Rhenium–Porphyrin Dyads for CO₂ Photoreduction: Photocatalytic Studies and Charge Separation Dynamics Studied by Time-Resolved IR Spectroscopy. *Chem. Sci.* **2015**, 6 (12), 6847–6864. <https://doi.org/10.1039/C5SC02099A>.
- (36) Lang, P.; Pfrunder, M.; Quach, G.; Braun-Cula, B.; Moore, E. G.; Schwalbe, M. Sensitized Photochemical CO₂ Reduction by Hetero-Pacman Compounds Linking a ReI Tricarbonyl with a

- Porphyrin Unit. *Chem. – Eur. J.* **2019**, 25 (17), 4509–4519. <https://doi.org/10.1002/chem.201806347>.
- (37) Kuramochi, Y.; Fujisawa, Y.; Satake, A. Photocatalytic CO₂ Reduction Mediated by Electron Transfer via the Excited Triplet State of Zn(II) Porphyrin. *J. Am. Chem. Soc.* **2020**, 142 (2), 705–709. <https://doi.org/10.1021/jacs.9b12712>.
 - (38) Franco, F.; Cometto, C.; Garino, C.; Minero, C.; Sordello, F.; Nervi, C.; Gobetto, R. Photo- and Electrocatalytic Reduction of CO₂ by [Re(CO)₃α,α'-Diimine-(4-Piperidinyl-1,8-Naphthalimide)Cl] Complexes. *Eur. J. Inorg. Chem.* **2015**, 2015 (2), 296–304. <https://doi.org/10.1002/ejic.201402912>.
 - (39) Martinez, J. F.; La Porte, N. T.; Wasielewski, M. R. Electron Transfer from Photoexcited Naphthalene Diimide Radical Anion to Electrocatalytically Active Re(Bpy)(CO)₃Cl in a Molecular Triad. *J. Phys. Chem. C* **2018**, 122 (5), 2608–2617. <https://doi.org/10.1021/acs.jpcc.7b11999>.
 - (40) Martinez, J. F.; La Porte, N. T.; Chaudhuri, S.; Sinopoli, A.; Bae, Y. J.; Sohail, M.; Batista, V. S.; Wasielewski, M. R. Effect of Electronic Coupling on Electron Transfer Rates from Photoexcited Naphthalenediimide Radical Anion to Re(Bpy)(CO)₃X. *J. Phys. Chem. C* **2019**, 123 (16), 10178–10190. <https://doi.org/10.1021/acs.jpcc.8b12264>.
 - (41) Martinez, J. F.; La Porte, N. T.; Wasielewski, M. R. Electron Transfer from Photoexcited Naphthalene-1,4:5,8-Bis(Dicarboximide) Radical Anion to Mn(Bpy)(CO)₃X and Re(Bpy)(CO)₃X CO₂ Reduction Catalysts Linked via a Saturated Methylene Bridge. *J. Photochem. Photobiol. Chem.* **2019**, 372, 21–28. <https://doi.org/10.1016/j.jphotochem.2018.11.047>.
 - (42) Hedström, S.; Chaudhuri, S.; La Porte, N. T.; Rudshteyn, B.; Martinez, J. F.; Wasielewski, M. R.; Batista, V. S. Thousandfold Enhancement of Photoreduction Lifetime in Re(Bpy)(CO)₃ via Spin-Dependent Electron Transfer from a Perylenediimide Radical Anion Donor. *J. Am. Chem. Soc.* **2017**, 139 (46), 16466–16469. <https://doi.org/10.1021/jacs.7b09438>.
 - (43) Porte, N. T. L.; Martinez, J. F.; Hedström, S.; Rudshteyn, B.; Phelan, B. T.; Mauck, C. M.; Young, R. M.; Batista, V. S.; Wasielewski, M. R. Photoinduced Electron Transfer from Rylenediimide Radical Anions and Dianions to Re(Bpy)(CO)₃ Using Red and near-Infrared Light. *Chem. Sci.* **2017**, 8 (5), 3821–3831. <https://doi.org/10.1039/C6SC05103K>.
 - (44) Liu, Z.; Wu, Y.; Zhang, Q.; Gao, X. Non-Fullerene Small Molecule Acceptors Based on Perylene Diimides. *J. Mater. Chem. A* **2016**, 4 (45), 17604–17622. <https://doi.org/10.1039/C6TA06978A>.
 - (45) Chen, W.; Zhang, Q. Recent Progress in Non-Fullerene Small Molecule Acceptors in Organic Solar Cells (OSCs). *J. Mater. Chem. C* **2017**, 5 (6), 1275–1302. <https://doi.org/10.1039/C6TC05066B>.
 - (46) Nowak-Król, A.; Shoyama, K.; Stolte, M.; Würthner, F. Naphthalene and Perylene Diimides – Better Alternatives to Fullerenes for Organic Electronics? *Chem. Commun.* **2018**, 54 (98), 13763–13772. <https://doi.org/10.1039/C8CC07640E>.
 - (47) Hendsbee, A. D.; Sun, J.-P.; Law, W. K.; Yan, H.; Hill, I. G.; Spasyuk, D. M.; Welch, G. C. Synthesis, Self-Assembly, and Solar Cell Performance of N-Annulated Perylene Diimide Non-Fullerene Acceptors. *Chem. Mater.* **2016**, 28 (19), 7098–7109. <https://doi.org/10.1021/acs.chemmater.6b03292>.
 - (48) Cann, J. R.; Cabanetos, C.; Welch, G. C. Synthesis of Molecular Dyads and Triads Based Upon N-Annulated Perylene Diimide Monomers and Dimers. *Eur. J. Org. Chem.* **2018**, 2018 (48), 6933–6943. <https://doi.org/10.1002/ejoc.201801383>.
 - (49) Vespa, M.; Cann, J. R.; Dayneko, S. V.; Melville, O. A.; Hendsbee, A. D.; Zou, Y.; Lessard, B. H.; Welch, G. C. Synthesis of a Perylene Diimide Dimer with Pyrrolic N–H Bonds and N-Functionalized Derivatives for Organic Field-Effect Transistors and Organic Solar Cells. *Eur. J. Org. Chem.* **2018**, 2018 (33), 4592–4599. <https://doi.org/10.1002/ejoc.201801055>.
 - (50) Guo, Y.; Ma, Z.; Niu, X.; Zhang, W.; Tao, M.; Guo, Q.; Wang, Z.; Xia, A. Bridge-Mediated Charge Separation in Isomeric N-Annulated Perylene Diimide Dimers. *J. Am. Chem. Soc.* **2019**, 141 (32), 12789–12796. <https://doi.org/10.1021/jacs.9b05723>.
 - (51) Benson Eric E.; Sampson Matthew D.; Grice Kyle A.; Smieja Jonathan M.; Froehlich Jesse D.; Friebel Daniel; Keith John A.; Carter Emily A.; Nilsson Anders; Kubiak Clifford P. The Electronic States of Rhenium Bipyridyl Electrocatalysts for CO₂ Reduction as Revealed by X-ray Absorption

- Spectroscopy and Computational Quantum Chemistry. *Angew. Chem. Int. Ed.* **2013**, 52 (18), 4841–4844. <https://doi.org/10.1002/anie.201209911>.
- (52) Machan, C. W.; Sampson, M. D.; Chabolla, S. A.; Dang, T.; Kubiak, C. P. Developing a Mechanistic Understanding of Molecular Electrocatalysts for CO₂ Reduction Using Infrared Spectroelectrochemistry. *Organometallics* **2014**, 33 (18), 4550–4559. <https://doi.org/10.1021/om500044a>.
 - (53) Machan, C. W.; Chabolla, S. A.; Yin, J.; Gilson, M. K.; Tezcan, F. A.; Kubiak, C. P. Supramolecular Assembly Promotes the Electrocatalytic Reduction of Carbon Dioxide by Re(I) Bipyridine Catalysts at a Lower Overpotential. *J. Am. Chem. Soc.* **2014**, 136 (41), 14598–14607. <https://doi.org/10.1021/ja5085282>.
 - (54) Christensen, P.; Hamnett, A.; Muir, A. V. G.; Timney, J. A. An in Situ Infrared Study of CO₂ Reduction Catalysed by Rhenium Tricarbonyl Bipyridyl Derivatives. *J. Chem. Soc. Dalton Trans.* **1992**, No. 9, 1455–1463. <https://doi.org/10.1039/DT9920001455>.
 - (55) Koenig, J. D. B.; Laventure, A.; Welch, G. C. Harnessing Direct (Hetero)Arylation in Pursuit of a Saddle-Shaped Perylene Diimide Tetramer. *ACS Appl. Energy Mater.* **2019**, 2 (12), 8939–8945. <https://doi.org/10.1021/acsaem.9b01978>.
 - (56) McAfee, S. M.; Dayneko, S. V.; Josse, P.; Blanchard, P.; Cabanetos, C.; Welch, G. C. Simply Complex: The Efficient Synthesis of an Intricate Molecular Acceptor for High-Performance Air-Processed and Air-Tested Fullerene-Free Organic Solar Cells. *Chem. Mater.* **2017**, 29 (3), 1309–1314. <https://doi.org/10.1021/acs.chemmater.6b04862>.
 - (57) Shirman, E.; Ustinov, A.; Ben-Shitrit, N.; Weissman, H.; Iron, M. A.; Cohen, R.; Rybtchinski, B. Stable Aromatic Dianion in Water. *J. Phys. Chem. B* **2008**, 112 (30), 8855–8858. <https://doi.org/10.1021/jp8029743>.
 - (58) Seifert, S.; Schmidt, D.; Würthner, F. An Ambient Stable Core-Substituted Perylene Bisimide Dianion: Isolation and Single Crystal Structure Analysis. *Chem. Sci.* **2015**, 6 (3), 1663–1667. <https://doi.org/10.1039/C4SC03671A>.
 - (59) Costentin, C.; Savéant, J.-M. Towards an Intelligent Design of Molecular Electrocatalysts. *Nat. Rev. Chem.* **2017**, 1 (11), 0087. <https://doi.org/10.1038/s41570-017-0087>.
 - (60) Rountree, E. S.; McCarthy, B. D.; Eisenhart, T. T.; Dempsey, J. L. Evaluation of Homogeneous Electrocatalysts by Cyclic Voltammetry. *Inorg. Chem.* **2014**, 53 (19), 9983–10002. <https://doi.org/10.1021/ic500658x>.
 - (61) Azcarate, I.; Costentin, C.; Robert, M.; Savéant, J.-M. Through-Space Charge Interaction Substituent Effects in Molecular Catalysis Leading to the Design of the Most Efficient Catalyst of CO₂-to-CO Electrochemical Conversion. *J. Am. Chem. Soc.* **2016**, 138 (51), 16639–16644. <https://doi.org/10.1021/jacs.6b07014>.
 - (62) Koenig, J. D. B.; Willkomm, J.; Roesler, R.; Piers, W. E.; Welch, G. C. Electrocatalytic CO₂ Reduction at Lower Overpotentials Using Iron(III) Tetra(Meso-Thienyl)Porphyrins. *ACS Appl. Energy Mater.* **2019**, 2 (6), 4022–4026. <https://doi.org/10.1021/acsaem.9b00761>.
 - (63) Hao, L.; Jiang, W.; Wang, Z. Integration of Nitrogen into Coronene Bisimides. *Tetrahedron* **2012**, 68 (45), 9234–9239. <https://doi.org/10.1016/j.tet.2012.08.084>.
 - (64) Schulze, M.; Steffen, A.; Würthner, F. Near-IR Phosphorescent Ruthenium(II) and Iridium(III) Perylene Bisimide Metal Complexes. *Angew. Chem. Int. Ed.* **2015**, 54 (5), 1570–1573. <https://doi.org/10.1002/anie.201410437>.
 - (65) Li, G.; Zhao, Y.; Li, J.; Cao, J.; Zhu, J.; Sun, X. W.; Zhang, Q. Synthesis, Characterization, Physical Properties, and OLED Application of Single BN-Fused Perylene Diimide. *J. Org. Chem.* **2015**, 80 (1), 196–203. <https://doi.org/10.1021/jo502296z>.
 - (66) Cometto, C.; Chen, L.; Lo, P.-K.; Guo, Z.; Lau, K.-C.; Anxolabéhère-Mallart, E.; Fave, C.; Lau, T.-C.; Robert, M. Highly Selective Molecular Catalysts for the CO₂-to-CO Electrochemical Conversion at Very Low Overpotential. Contrasting Fe vs Co Quaterpyridine Complexes upon Mechanistic Studies. *ACS Catal.* **2018**, 8, 3411–3417. <https://doi.org/10.1021/acscatal.7b04412>.

- (67) Fernández, S.; Franco, F.; Casadevall, C.; Martin-Diaconescu, V.; Luis, J. M.; Lloret-Fillol, J. A Unified Electro- and Photocatalytic CO₂ to CO Reduction Mechanism with Aminopyridine Cobalt Complexes. *J. Am. Chem. Soc.* **2020**, *142* (1), 120–133. <https://doi.org/10.1021/jacs.9b06633>.
- (68) Sahara, G.; Kumagai, H.; Maeda, K.; Kaeffer, N.; Artero, V.; Higashi, M.; Abe, R.; Ishitani, O. Photoelectrochemical Reduction of CO₂ Coupled to Water Oxidation Using a Photocathode with a Ru(II)–Re(I) Complex Photocatalyst and a CoOx/TaON Photoanode. *J. Am. Chem. Soc.* **2016**, *138* (42), 14152–14158. <https://doi.org/10.1021/jacs.6b09212>.
- (69) Kamata, R.; Kumagai, H.; Yamazaki, Y.; Sahara, G.; Ishitani, O. Photoelectrochemical CO₂ Reduction Using a Ru(II)–Re(I) Supramolecular Photocatalyst Connected to a Vinyl Polymer on a NiO Electrode. *ACS Appl. Mater. Interfaces* **2019**, *11* (6), 5632–5641. <https://doi.org/10.1021/acsami.8b05495>.
- (70) Sato, S.; Matubara, Y.; Koike, K.; Falkenström, M.; Katayama, T.; Ishibashi, Y.; Miyasaka, H.; Taniguchi, S.; Chosrowjan, H.; Mataga, N.; Fukazawa, N.; Koshihara, S.; Onda, K.; Ishitani, O. Photochemistry of Fac-[Re(Bpy)(CO)3Cl]. *Chem. Weinh. Bergstr. Ger.* **2012**, *18* (49), 15722–15734. <https://doi.org/10.1002/chem.201202734>.
- (71) Lang, P.; Giereth, R.; Tschierlei, S.; Schwalbe, M. Unexpected Wavelength Dependency of the Photocatalytic CO₂ Reduction Performance of the Well-Known (Bpy)Re(CO)3Cl Complex. *Chem. Commun.* **2019**, *55* (5), 600–603. <https://doi.org/10.1039/C8CC08742C>.
- (72) Morimoto, T.; Nakajima, T.; Sawa, S.; Nakanishi, R.; Imori, D.; Ishitani, O. CO₂ Capture by a Rhenium(I) Complex with the Aid of Triethanolamine. *J. Am. Chem. Soc.* **2013**, *135* (45), 16825–16828. <https://doi.org/10.1021/ja409271s>.
- (73) Kou, Y.; Nabetani, Y.; Masui, D.; Shimada, T.; Takagi, S.; Tachibana, H.; Inoue, H. Direct Detection of Key Reaction Intermediates in Photochemical CO₂ Reduction Sensitized by a Rhenium Bipyridine Complex. *J. Am. Chem. Soc.* **2014**, *136* (16), 6021–6030. <https://doi.org/10.1021/ja500403e>.
- (74) Pekdemir, F.; Orman, E. B.; Selçuki, N. A.; Özkaya, A. R.; Salih, B.; Şengül, A. Spectroscopic, Electrochemical and Electrocolorimetric Properties of Novel 2-(2'-Pyridyl)-1H-Benzimidazole Appended Bay-Substituted Perylene Diimide Triads. *J. Photochem. Photobiol. Chem.* **2019**, *379*, 54–62. <https://doi.org/10.1016/j.jphotochem.2019.04.039>.
- (75) Kumar, Y.; Kumar, S.; Bansal, D.; Mukhopadhyay, P. Synthesis and Isolation of a Stable Perylenediimide Radical Anion and Its Exceptionally Electron-Deficient Precursor. *Org. Lett.* **2019**, *21* (7), 2185–2188. <https://doi.org/10.1021/acs.orglett.9b00490>.
- (76) Zhang, A.; Jiang, W.; Wang, Z. Fulvalene-Embedded Perylene Diimide and Its Stable Radical Anion. *Angew. Chem. Int. Ed.* **2020**, *59* (2), 752–757. <https://doi.org/10.1002/anie.201912536>.
- (77) Scheiring, T.; Klein, A.; Kaim, W. EPR Study of Paramagnetic Rhenium(I) Complexes (Bpy>>>>>)Re(CO)3X Relevant to the Mechanism of Electrocatalytic CO₂ Reduction†. *J. Chem. Soc. Perkin Trans. 2* **1997**, No. 12, 2569–2572. <https://doi.org/10.1039/A702467C>.
- (78) Wang, M.; Weyhermüller, T.; Bill, E.; Ye, S.; Wieghardt, K. Structural and Spectroscopic Characterization of Rhenium Complexes Containing Neutral, Monoanionic, and Dianionic Ligands of 2,2'-Bipyridines and 2,2':6,2''-Terpyridines: An Experimental and Density Functional Theory (DFT)-Computational Study. *Inorg. Chem.* **2016**, *55* (10), 5019–5036. <https://doi.org/10.1021/acs.inorgchem.6b00609>.
- (79) Zhao, Y.; Truhlar, D. G. The M06 Suite of Density Functionals for Main Group Thermochemistry, Thermochemical Kinetics, Noncovalent Interactions, Excited States, and Transition Elements: Two New Functionals and Systematic Testing of Four M06-Class Functionals and 12 Other Functionals. *Theor. Chem. Acc.* **2008**, *120* (1), 215–241. <https://doi.org/10.1007/s00214-007-0310-x>.
- (80) Hariharan, P. C.; Pople, J. A. The Influence of Polarization Functions on Molecular Orbital Hydrogenation Energies. *Theor. Chim. Acta* **1973**, *28* (3), 213–222. <https://doi.org/10.1007/BF00533485>.

- (81) Petersson, G. A.; Bennett, A.; Tensfeldt, T. G.; Al-Laham, M. A.; Shirley, W. A.; Mantzaris, J. A. Complete Basis Set Model Chemistry. I. The Total Energies of Closed-shell Atoms and Hydrides of the First-row Elements. *J. Chem. Phys.* **1988**, *89* (4), 2193–2218. <https://doi.org/10.1063/1.455064>.
- (82) Petersson, G. A.; Al-Laham, M. A. A Complete Basis Set Model Chemistry. II. Open-shell Systems and the Total Energies of the First-row Atoms. *J. Chem. Phys.* **1991**, *94* (9), 6081–6090. <https://doi.org/10.1063/1.460447>.
- (83) Hehre, W. J.; Ditchfield, R.; Pople, J. A. Self—Consistent Molecular Orbital Methods. XII. Further Extensions of Gaussian—Type Basis Sets for Use in Molecular Orbital Studies of Organic Molecules. *J. Chem. Phys.* **1972**, *56* (5), 2257–2261. <https://doi.org/10.1063/1.1677527>.
- (84) Hay, P. J.; Wadt, W. R. Ab Initio Effective Core Potentials for Molecular Calculations. Potentials for the Transition Metal Atoms Sc to Hg. *J. Chem. Phys.* **1985**, *82* (1), 270–283. <https://doi.org/10.1063/1.448799>.
- (85) Wadt, W. R.; Hay, P. J. Ab Initio Effective Core Potentials for Molecular Calculations. Potentials for Main Group Elements Na to Bi. *J. Chem. Phys.* **1985**, *82* (1), 284–298. <https://doi.org/10.1063/1.448800>.
- (86) Smieja, J. M.; Benson, E. E.; Kumar, B.; Grice, K. A.; Seu, C. S.; Miller, A. J. M.; Mayer, J. M.; Kubiak, C. P. Kinetic and Structural Studies, Origins of Selectivity, and Interfacial Charge Transfer in the Artificial Photosynthesis of CO. *Proc. Natl. Acad. Sci.* **2012**, *109* (39), 15646–15650. <https://doi.org/10.1073/pnas.1119863109>.
- (87) Riplinger, C.; Sampson, M. D.; Ritzmann, A. M.; Kubiak, C. P.; Carter, E. A. Mechanistic Contrasts between Manganese and Rhenium Bipyridine Electrocatalysts for the Reduction of Carbon Dioxide. *J. Am. Chem. Soc.* **2014**, *136* (46), 16285–16298. <https://doi.org/10.1021/ja508192y>.
- (88) A. Grice, K.; X. Gu, N.; D. Sampson, M.; P. Kubiak, C. Carbon Monoxide Release Catalysed by Electron Transfer : Electrochemical and Spectroscopic Investigations of [Re(Bpy-R)(CO) 4](OTf) Complexes Relevant to CO 2 Reduction. *Dalton Trans.* **2013**, *42* (23), 8498–8503. <https://doi.org/10.1039/C3DT50612F>.
- (89) Marenich, A. V.; Cramer, C. J.; Truhlar, D. G. Universal Solvation Model Based on Solute Electron Density and on a Continuum Model of the Solvent Defined by the Bulk Dielectric Constant and Atomic Surface Tensions. *J. Phys. Chem. B* **2009**, *113* (18), 6378–6396. <https://doi.org/10.1021/jp810292n>.
- (90) Costentin, C.; Drouet, S.; Robert, M.; Savéant, J.-M. A Local Proton Source Enhances CO₂ Electroreduction to CO by a Molecular Fe Catalyst. *Science* **2012**, *338* (6103), 90–94. <https://doi.org/10.1126/science.1224581>.

*** Table of Contents (TOC) Graphic ***

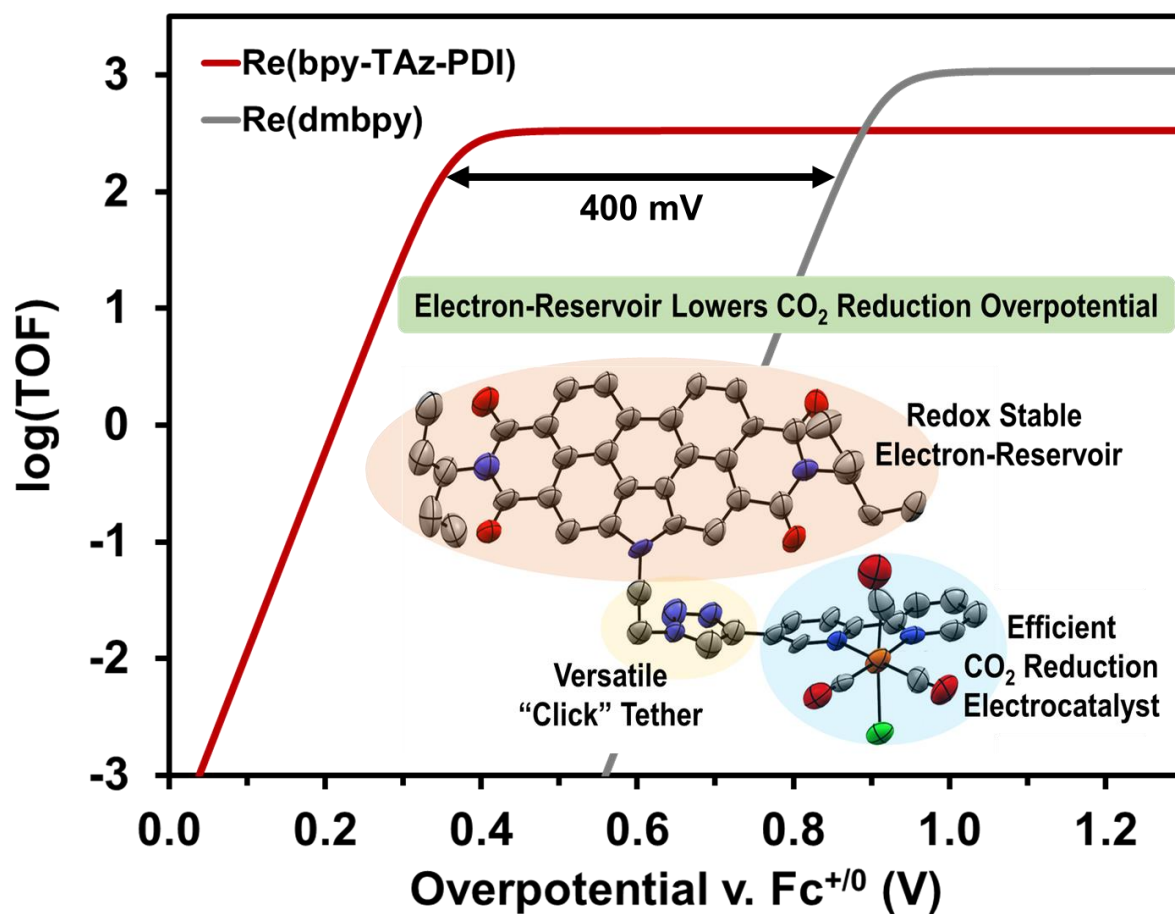


*** Table of Contents (TOC) Graphic ***

Electron-Reservoir Effect on a Perylene Diimide Tethered Rhenium Bipyridine Complex for CO₂ Reduction

(Supporting Information)

Josh D. B. Koenig^a, Zachary Dubrawski^a, Keerthan R. Rao^b, Janina Willkomm^a, Benjamin S. Gelfand^a, Chad Risko^b, Warren E. Piers^a, and Gregory C. Welch^{a*}

^a Department of Chemistry, University of Calgary, 2500 University Drive N.W., Calgary, Alberta, T2N 1N4, Canada.

^b Department of Chemistry & Center for Applied Energy Research, University of Kentucky, Lexington, Kentucky 40506, United States

* Corresponding Author
Email: gregory.welch@ucalgary.ca
Phone Number: 1-403-210-7603

Keywords: CO₂ reduction; electrochemical catalysis; molecular catalysis; rhenium; bipyridine; Re(bpy); perylene diimide; PDI

TABLE OF CONTENTS

| | |
|--|-----------|
| 1. Materials and Methods | S2 – S4 |
| 2. Synthetic/Experimental Procedures | S5 – S9 |
| 3. ¹ H & ¹³ C NMR and EPR Spectroscopies | S10 – S17 |
| 4. MALDI-TOF MS & CHN Elemental Analysis | S18 – S20 |
| 5. UV-Vis & FTIR Spectroscopy | S21 – S24 |
| 6. Cyclic Voltammetry & Spectroelectrochemistry | S25 – S28 |
| 7. Electro- and Photocatalytic CO ₂ Reduction | S29 – S34 |
| 8. Density Functional Theory Calculations | S35 – S45 |
| 9. X-ray Diffraction Crystallography | S46 – S51 |
| 10. References | S52 – S54 |

1. Methods and Materials

Materials: All air-free reactions were carried out under an atmosphere of argon using standard glove box or high vacuum line (Schlenk) techniques unless otherwise stated. For inert atmosphere manipulations, reagents and solvents were stored in argon-filled glove boxes prior to use. THF was dried and degassed over activated alumina using a solvent purification system, dried further with Na/benzophenone and vacuum distilled prior to use. MeCN-d₃ (99.8 % D, Sigma-Aldrich) was transferred into a Schlenk flask and dried over 20% w/v activated 3 Å molecular sieves for at least 24 h then vacuum distilled prior to use. ¹ KC₈ was synthesized according to literature procedure. ² All other reactants, reagents, and catalysts were purchased from Millipore-Sigma or Fisher Scientific and used without further purification.

Nuclear Magnetic Resonance (NMR): ¹H and ¹³C NMR spectroscopy experiments were recorded using a Bruker Avance III 500 MHz spectrometer. All experiments were performed in either chloroform-d (CDCl₃) or acetonitrile-d₃ (MeCN-d₃). Chemical shifts (referenced to residual solvent) were reported in parts per million (ppm). Multiplicities were reported as follows: singlet (s), doublets (d), triplets (t), quartet (q), pentet (p), doublet of doublets (dd), doublet of triplets (dt), doublet of quartets (dq), triplet of doublets (td), triplet of triplets (tt), doublet of doublet of doublets (ddd), and multiplets (m).

High-resolution MALDI-TOF (HR MALDI-TOF): High-resolution MALDI-TOF mass spectrometry measurements were performed courtesy of Johnson Li in the Chemical Instrumentation Facility at the University of Calgary (UofC). Sample solution (~ 1 µg/mL in CH₂Cl₂) was mixed with matrix trans-2-[3-(4-tert-Butylphenyl)-2-methyl-2-propenylidene]malononitrile (DCTB) solution (~5 mg/ml in methanol). All spectra were acquired using a Bruker Autoflex III Smartbeam MALDI-TOF, set to the positive reflective mode (Na:YAG 355 nm laser settings: laser offset = 62-69; laser frequency = 200Hz; and number of shots = 300). The target used was Bruker MTP 384 ground steel plate target.

CHN Elemental Analysis: Elemental analyses were performed by Johnson Li in the Chemical Instrumentation Facility at the UofC. A Perkin Elmer 2400 Series II CHN Elemental Analyzer was used to obtain CHN data, using ~1.5 mg of sample (with particle sizes ranging between 0.2 and 0.5 mm in diameter).

UV-Visible Spectroscopy (UV-Vis): Optical absorption measurements were performed using Agilent Technologies Cary 60 UV-Vis spectrometer at ambient conditions. All solution UV-Vis spectra were measured with 2 or 10 mm quartz cuvettes, using CH₂Cl₂, N,N-dimethylformamide (DMF), or tetrahydrofuran (THF) as solvent. Stock solutions (~1 mg/mL) of each compound were prepared, serially diluted to concentrations between 10⁻⁵ - 10⁻⁶ M, and then used to construct calibration curves for determining molar absorptivity.

Fourier Transform Infrared Spectroscopy (FTIR): All IR absorption measurements were performed using an Agilent Technologies Cary 630 FTIR spectrometer at room temperature. FTIR spectra were measured from CH₂Cl₂ or DMF solutions of the analyte, using either the dial-path module (pathlength = 30 microns) or the transmission module. Solid samples were made from anhydrous potassium bromide (KBr), prepared in an argon filled glovebox, and analyzed with air-free techniques.

Electron Paramagnetic Resonance (EPR): X-band EPR spectra (9.34 GHz) were recorded on a Bruker EMX 10/12 spectrometer equipped with VT capabilities with a 10-inch magnet and a 12 kV power supply. Dry and degassed toluene or THF was used as the solvent. Spectra were simulated with EasySpin³ using the Simultispin GUI package.⁴

Spectroelectrochemistry (SEC): All UV-vis SEC and FTIR SEC experiments were conducted using a LabOmak IR-SEC cell fitted with CaF₂ windows (pathlength = 0.2 mm), a Pt-mesh working electrode (WE), a Pt-wire counter electrode (CE), an Ag-wire pseudo-reference electrode (RE), and Fc⁺⁰ as an internal reference standard. The cell was filled with DMF solutions (~0.1 mL) containing 0.5 mM analyte and 0.1 M TBAPF₆. Solutions were sparged with argon in a scintillation vial for 15 minutes prior to use. Blank DMF solutions containing 0.1 M TBAPF₆ were used to baseline correct spectra at each voltage step.

Cyclic Voltammetry (CV): All electrochemical measurements were performed using a CH Instruments Inc. Model 1200B Series Handheld Potentiostat. A standard 3-electrode setup was utilized, consisting of a freshly polished glassy carbon disk WE, Pt-wire CE, Ag/AgCl pseudo-RE, and ferrocene (Fc⁺⁰) as an internal standard. All cyclic voltammetry experiments were performed at a scan rate of 100 mV/s (unless otherwise specified). Sample solutions, with 0.5 mM compound and 0.1 M tetrabutylammonium hexafluorophosphate (TBAPF₆) supporting electrolyte, were prepared in anhydrous CH₂Cl₂, MeCN, or DMF. All electrochemical solutions were sparged with dry gas (either argon or CO₂) for 15 minutes prior to measurements.

The impact of proton source concentration on catalytic current enhancement was tested using two weak acids, phenol (PhOH: pK_a = 18.8) or 2,2,2-trifluoroethanol (TFE; pK_a = 24.0).⁵ Two initial measurements were run, the first under argon and the second after the solution was sparged with CO₂. To the CO₂-saturated sample (0.23 M in DMF and 0.25 M in MeCN), the specified proton-source was added incrementally until a maximal current enhancement was achieved.

Controlled Potential Electrolysis (CPE): CPE experiments were performed with a customized two-compartment H-shaped cell, using a Princeton Applied Research VersaSTAT 3 potentiostat. A glassy carbon plate (20 mm x 8 mm x 2 mm) was used as the WE, along with a Pt-mesh CE, and a non-aqueous Ag/AgCl pseudo-RE. For all experiments using the two-compartment H-shaped cell (44.1 mL), two solutions were prepared: an active solution (0.5 mM catalyst + 0.1 M TBAPF₆ + TFE), and a blank solution (0.1 M TBAPF₆ + TFE). The glassy carbon plate WE and Ag/AgCl pseudo-RE were immersed into the active solution in the cathodic compartment, while the Pt-mesh CE was immersed into the blank solution in the anodic compartment. The potentiostat, using the chronoamperometry setting, applied a constant voltage for the duration of testing. Small headspace aliquots (50 µL) were periodically removed from the flask/cell to analyze gaseous product distribution.

Gas chromatography (GC): GC headspace analysis (50 µL aliquots) was performed using an Agilent Technologies 7890B GC, equipped with a PoraPlot Q and PLOT molecular sieve (5 Å) column (oven temperature 60 – 120 °C) in series and a VICI pulsed discharge Helium ionization detector. The flow rate of the carrier gas (helium) was approximately 5 mL min⁻¹. The system was calibrated using a customized gas mixture, containing known concentrations of: H₂, CO, CH₄, ethylene, and ethane.

Photochemistry: CO₂ photocatalysis experiments were performed using a 10 mL μ wave vial that was sealed with a rubber septum. The catalyst (65 μ M) was dissolved in either a (5:1:0) or a (4:1:1) mixture of DMF : triethanolamine : TFE. Samples were sparged with CO₂ for 20 minutes prior to be irradiated with a Thor Labs Blue LED ($\lambda = 470 \pm 30$ nm; 4.0 mW cm⁻²). Headspace aliquots (50 μ L) were removed periodically from the vials to analyze gaseous products.

Data Handling/Calculations:

i) Randles Sevcik Equation (i_p scan rate dependency for diffusion-controlled processes) ⁶

$$i_p = 0.4463 nFAc_{cat} \sqrt{\frac{nFvD}{RT}}$$

Where: i_p = peak current of redox wave, n = # of electrons transferred, F = Faradaic constant, A = geometric area of the working electrode, c_{cat} = catalyst concentration, v = scan rate, D = diffusion coefficient, R = universal gas constant, and T = temperature.

ii) Determination of k_{obs} using the i_{cat} / i_p analysis ⁷

$$\frac{i_{cat}}{i_p} = 2.2406 \sqrt{\frac{RT}{nFv}} n' k_{obs}$$

Where: i_{cat} = peak current of redox wave under catalytic conditions, i_p = peak current of redox wave, R = universal gas constant, T = temperature, n = # of electrons transferred, F = Faradaic constant, v = scan rate, n' = # of catalyst molecules required per turnover ($n' = 1$), and k_{obs} = observed catalytic rate constant.

iii) Tafel Plot ⁸

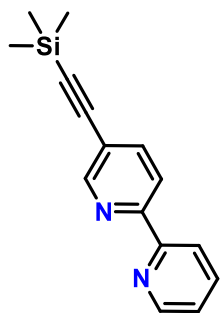
$$TOF = \frac{TOF_{max}}{\left(1 + \exp\left[\left(\frac{F}{RT}\right)(E_{tr}^0 - E_{cat}^0)\right]\right) \times \exp\left[-\left(\frac{F}{RT}\right)\eta\right]}$$

Where: TOF = turnover frequency, $TOF_{max} = k_{obs}$, F = Faradaic constant, R = gas constant, T = temperature, E_{tr}^0 = thermodynamic redox potential of CO₂/CO in DMF (-1.46 V vs. Fc^{+/0}) or in MeCN (-1.12 V vs. Fc^{+/0}), ⁷⁻⁹ E_{cat}^0 = catalyst standard potential of E_{1/2}, and η : overpotential ($E_{tr}^0 - E_{electrode}$).

2. Synthetic/Experimental Procedures

5-[2-((Trimethylsilyl)-1-ethynyl)-2,2'-bipyridine

Starting material, 5-bromo-2,2'-bipyridine, was synthesized using modified literature procedure.¹⁰

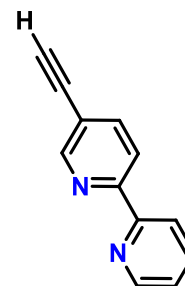


A 20 mL glass pressure vial was charged with 5-bromo-2,2'-bipyridine (1.05 g, 4.5 mmol, 1eq.) and copper iodide (86 mg, 0.45 mmol, 0.1 eq.). The vial was brought into the glovebox, where Pd(PPh₃)₄ (258 mg, 0.22 mmol, 0.05 eq.) was added prior to sealing the vial. After removing the vial from the glovebox, a thoroughly degassed mixture of (1:1) diisopropylamine : toluene (16 mL) was transferred into the vial using a Cannula line. Next, trimethylsilylacetylene (1.9 mL, 13.4 mmol, 3 eq.) was injected into the reaction mixture and then the vial was placed in a 60 °C bead bath for 14 hours, monitoring progress by thin layer chromatography (TLC). Upon reaction completion, the mixture was passed through a Celite plug (eluting with CH₂Cl₂) and solvent was removed by rotary evaporation. The dark brown crude mixture was re-dissolved in minimal CH₂Cl₂, adhered to silica, and then purified using a short silica plug. The plug was first washed with hexanes, followed by a (5:1) hexanes : ethyl acetate mixture. The latter solvent mixture was removed by rotary evaporation to afford a pale-yellow solid that matched known literature data (0.92 g, 3.6 mmol, 81% yield).¹¹ No additional purification was required.

¹H NMR (500 MHz, CDCl₃) δ 8.74 (dd, *J* = 2.1, 0.9 Hz, 1H), 8.69 (ddd, *J* = 4.8, 1.8, 0.9 Hz, 1H), 8.40 (dt, *J* = 8.0, 1.1 Hz, 1H), 8.37 (dd, *J* = 8.2, 0.9 Hz, 1H), 7.88 (dd, *J* = 8.2, 2.1 Hz, 1H), 7.83 (td, *J* = 7.7, 1.8 Hz, 1H), 7.32 (ddd, *J* = 7.5, 4.8, 1.2 Hz, 1H), 0.29 (s, 9H).

5-ethynyl-2,2'-bipyridine

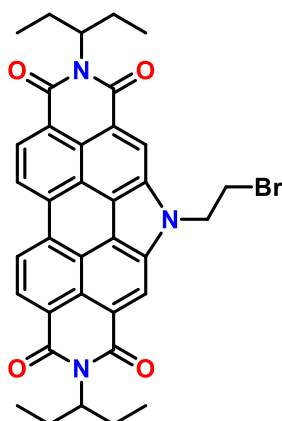
A 100 mL rbf was charged with 5-[2-((Trimethylsilyl)-1-ethynyl)-2,2'-bipyridine (0.92 g, 3.6 mmol, 1 eq.) and K₂CO₃ (1.99 g, 14.4 mmol, 4 eq.). The mixture was dissolved in methanol (25 mL) and stirred vigorously at room temperature. Reaction progress was monitored by TLC until all starting material was consumed. Upon reaction completion, the mixture was filtered through a Celite plug (eluting with CH₂Cl₂) and then solvent was removed by rotary evaporation. The resulting crude solid was re-dissolved in CH₂Cl₂, adhered to silica, and then purified using a short silica plug. The plug was washed with hexanes, then a (5:1) hexanes : ethyl acetate mixture. This solvent mixture was removed by rotary evaporation to afford a fluffy white solid that also matched known literature data (0.64 g, 3.6 mmol, 98% yield).¹¹ No further purification was required.



¹H NMR (500 MHz, CDCl₃) δ 8.76 (dd, *J* = 2.1, 0.9 Hz, 1H), 8.67 (ddd, *J* = 4.8, 1.8, 0.9 Hz, 1H), 8.43 – 8.34 (m, 2H), 7.88 (dd, *J* = 8.2, 2.1 Hz, 1H), 7.80 (td, *J* = 7.8, 1.8 Hz, 1H), 7.30 (ddd, *J* = 7.5, 4.8, 1.2 Hz, 1H), 3.29 (s, 1H).

Bromo-ethyl-N-annulated Perylene Diimide (BrEt-PDI)

Starting material, N-annulated PDI, was synthesized using literature procedure.¹²



N-annulated PDI (600 mg, 1.1 mmol, 1 eq.) and K₂CO₃ (310 mg, 2.2 mmol, 2 eq.) were added to a 20 mL glass pressure vial and dissolved in DMF (10 mL). The vial was sealed, sparged with N₂ for 15 minutes, and then 1,2-dibromoethane (0.48 mL, 5.5 mmol, 5 eq.) was added to the solution. The mixture was placed into a 60 °C bead bath and left to stir for 4 hours, monitoring reaction progress by TLC. When reaction progress was completed, the mixture was diluted with CH₂Cl₂ (50 mL), poured through a short Celite plug, and then solvent was removed using rotary evaporation. Next, the crude solid was subsequently re-dissolved in CH₂Cl₂ and purified using a silica plug (eluted with CH₂Cl₂). After solvent was removed by rotary evaporation, the isolated burgundy product was precipitated from a (19:1) MeOH : H₂O mixture and collected by vacuum filtration (440 mg, 0.68 mmol, 61% yield).

¹H NMR (500 MHz, CDCl₃) δ 9.03 (s, 2H), 8.99 (d, *J* = 8.0 Hz, 2H), 8.87 (d, *J* = 8.0 Hz, 2H), 5.31 (t, *J* = 6.2 Hz, 2H), 5.23 (dddd, *J* = 15.4, 9.5, 7.6 Hz, 2H), 4.05 (t, *J* = 6.2 Hz, 2H), 2.36 (ddq, *J* = 14.8, 9.6, 7.5 Hz, 4H), 2.08 – 1.95 (m, 4H), 0.99 (t, *J* = 7.5 Hz, 12H).

¹³C NMR (126 MHz, CDCl₃) δ 165.93, 164.71, 134.36, 132.44, 128.03, 127.37, 124.37, 123.63, 121.46, 119.47, 118.28, 117.74, 57.25, 47.55, 29.97, 24.65, 10.89.

HRMS ([M-H]⁺) calculated for M = C₃₆H₃₂N₃O₄Br: 648.1492; detected [M-H]⁺: 648.1511

Azide-ethyl-N-annulated Perylene Diimide (N₃-PDI)

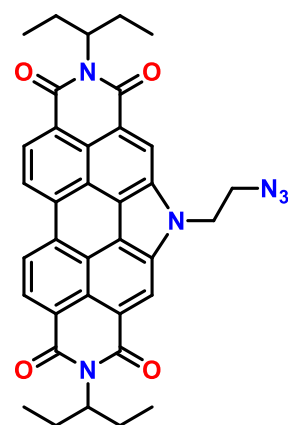
N₃-PDI was synthesized using a slightly modified literature procedure.¹³

BrEt-PDI (440 mg, 0.68 mmol, 1 eq.) and NaN₃ (83.2 mg, 1.3 mmol, 2 eq.) were added to a 100 mL rbf and dissolved in DMF (25 mL). The solution was sealed and left to stir overnight at room temperature. Upon reaction completion (as indicated by TLC), the mixture was poured into MeOH (125 mL) and H₂O (~10 mL) was added to induce precipitation. The resulting brick red precipitate was collected by vacuum filtration (415 mg, 0.67 mmol, 98 % yield).

¹H NMR (500 MHz, CDCl₃) δ 8.96 (s, 2H), 8.86 (d, *J* = 7.9 Hz, 2H), 8.80 (d, *J* = 8.3 Hz, 2H), 5.22 (tt, *J* = 9.5, 5.8 Hz, 2H), 4.97 (t, *J* = 5.5 Hz, 2H), 4.07 (t, *J* = 5.5 Hz, 2H), 2.37 (ddq, *J* = 14.8, 9.4, 7.5 Hz, 4H), 2.03 (tt, *J* = 13.5, 7.4 Hz, 4H), 1.00 (t, *J* = 7.5 Hz, 12H).

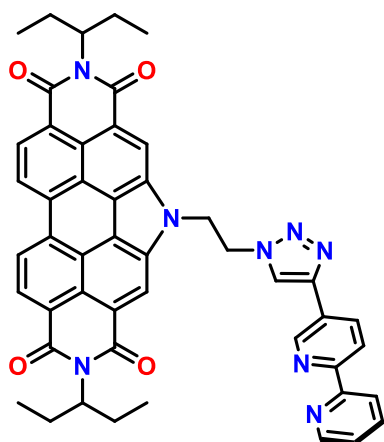
¹³C NMR (126 MHz, CDCl₃) δ 165.87, 164.51, 134.22, 132.16, 127.73, 127.37, 124.19, 123.40, 121.81, 119.22, 117.98, 117.65, 57.27, 51.27, 45.37, 24.64, 10.94.

HRMS ([M-H]⁺) calculated for M = C₃₆H₃₂N₆O₄: 611.2401; detected [M+H]⁺: 611.2377



Bipyridine-Triazole-N-annulated Perylene Diimide (bpy-TAz-PDI)

This compound was synthesized using a slightly modified literature procedure.¹³



N₃-PDI (310 mg, 0.52 mmol, 1 eq.) and 5-ethynyl-2,2'-bipyridine (100 mg, 0.56 mmol, 1.1 eq.) were combined in a 20 mL glass pressure vial with CuSO₄ (20 mg, 0.05 mmol, 0.1 eq.) and sodium ascorbate (60 mg, 0.18 mmol, 0.3 eq.). The vial was sealed and then N₂-sparged for 30 minutes. A degassed mixture of (4:1) THF : H₂O (20 mL) was transferred into the vial using a Cannula line. The mixture was purged an additional 5 minutes, then placed into a 60 °C bead bath for 18 hours. After TLC showed consumption of all starting material, the brick red mixture was poured into MeOH (with a small amount of H₂O) and collected by vacuum filtration. The crude solid was re-dissolved in CH₂Cl₂, adhered to silica, and then purified using a short silica plug. The plug was eluted first using hexanes : acetone gradient (4:1 → 1:1), followed

by flashing the plug with CH₂Cl₂ + 10% MeOH to afford the desired compound. Solvent was removed by rotary evaporation and the resulting bright orange solid was precipitated into MeOH and collected by vacuum filtration (261 mg, 0.33 mmol, 67%).

¹H NMR (500 MHz, CDCl₃) δ 9.00 (d, *J* = 7.8 Hz, 2H), 8.86 (d, *J* = 6.0 Hz, 2H), 8.81 – 8.70 (m, 3H), 8.66 (s, 1H), 8.33 (d, *J* = 4.8 Hz, 2H), 8.03 (d, *J* = 8.0 Hz, 1H), 7.81 (dd, *J* = 12.0, 8.0 Hz, 1H), 7.55 (s, 1H), 7.34 – 7.28 (m, 1H), 5.50 (t, *J* = 5.7 Hz, 2H), 5.19 (t, *J* = 5.7 Hz, 2H), 5.18 – 5.11 (m, 2H), 2.29 (dq, *J* = 7.9 Hz, 4H), 1.95 (dq, *J* = 14.0, 7.0 Hz, 4H), 0.91 (t, *J* = 7.4 Hz, 12H).

¹³C NMR ***not obtained due to very poor solubility of bpy-TAz-PDI (<0.5 mg/mL)***

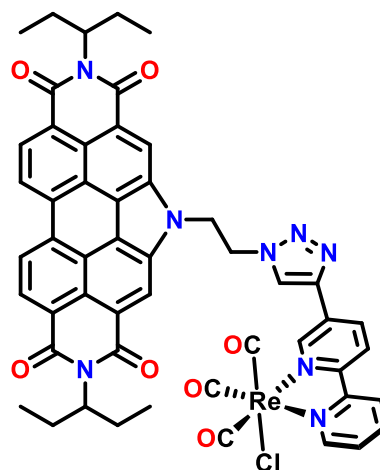
HRMS ([M+H]⁺) calculated for M = C₄₈H₄₀N₈O₄: 793.3245; detected [M+H]⁺: 793.3241

CHN theoretical (%) C: 72.71, H: 5.09, N: 14.13; found (%) C: 72.49, H: 4.99, N: 13.68;

UV-vis λ (x 10⁴ M⁻¹ cm⁻¹): 306 nm (2.5); 458 nm (1.6); 488 nm (3.1); 521 nm (5.9)

Re(bpy-TAz-PDI)(CO)₃Cl

Bpy-TAz-PDI (200 mg, 0.25 mmol, 1 eq.) and Re(CO)₅Cl (91.2 mg, 0.25 mmol, 1 eq.) were combined in a 20 mL glass pressure vial. The vial was sealed and then N₂-sparged for 15 minutes. Degassed toluene (16 mL) was transferred into the vial using a Cannula line. The mixture was purged an additional 15 minutes, then placed into a 110 °C bead bath for 14 hours. After TLC showed consumption of all starting material, solvent was removed from the red mixture by rotary evaporation. The crude solid was dissolved in CH₂Cl₂, adhered to silica, and then purified by silica-plug. The plug used a gradient (1:1 → 0:1) hexanes : THF mixture to remove the impurities and then elute the product. Solvent was removed by



rotary evaporation and the resulting red solid was precipitated into MeOH and collected by vacuum filtration (266 mg, 0.24 mmol, 96 % yield).

$^1\text{H NMR}$ (500 MHz, CDCl_3) δ 9.01 (d, $J = 5.4$ Hz, 1H), 8.98 (d, $J = 2.0$ Hz, 1H), 8.93 (d, $J = 8.0$ Hz, 2H), 8.82 (s, 2H), 8.74 (s, 2H), 8.49 (d, $J = 8.5$ Hz, 1H), 8.13 (dd, $J = 15.9, 8.4$ Hz, 2H), 8.04 (dd, $J = 8.6, 7.0$ Hz, 1H), 7.89 (s, 1H), 7.52 (dt, $J = 8.0, 2.0$ Hz, 1H), 5.52 (d, $J = 6.3$ Hz, 2H), 5.28 (d, $J = 6.1$ Hz, 2H), 5.16 (s, 2H), 2.29 (q, $J = 7.5$ Hz, 4H), 1.96 (dp, $J = 14.1, 7.3$ Hz, 4H), 0.92 (td, $J = 7.4, 3.9$ Hz, 12H).

$^1\text{H NMR}$ (500 MHz, CD_3CN) δ 8.98 (d, $J = 4.2$ Hz, 1H), 8.90 (s, 1H), 8.35-8.20 (m, 8H), 8.14 (td, $J = 7.8, 1.4$ Hz, 1H), 8.07 (br s, 1H), 7.87 (br s, 1H), 7.61 (t, $J = 6.8$ Hz, 1H), 5.09-4.95 (m, 4H), 4.93-4.81 (m, 2H) 1.33-1.21 (m, 8H), 0.93-0.79 (m, 12H)

$^{13}\text{C NMR}$ (126 MHz, CDCl_3) δ 154.63, 153.90, 152.61, 149.03, 141.79, 138.42, 135.18, 134.15, 132.58, 126.49, 124.43, 123.91, 122.56, 122.48, 121.84, 121.53, 119.68, 57.17, 50.66, 45.95, 24.56, 10.86. *some quaternary centers were not visible*

HRMS ($[\text{M}-\text{Cl}]^+$) calculated for $\text{M} = \text{C}_{51}\text{H}_{40}\text{N}_8\text{O}_7\text{ReCl}$: 1063.2572; detected $[\text{M}-\text{Cl}]^+$: 1063.2572

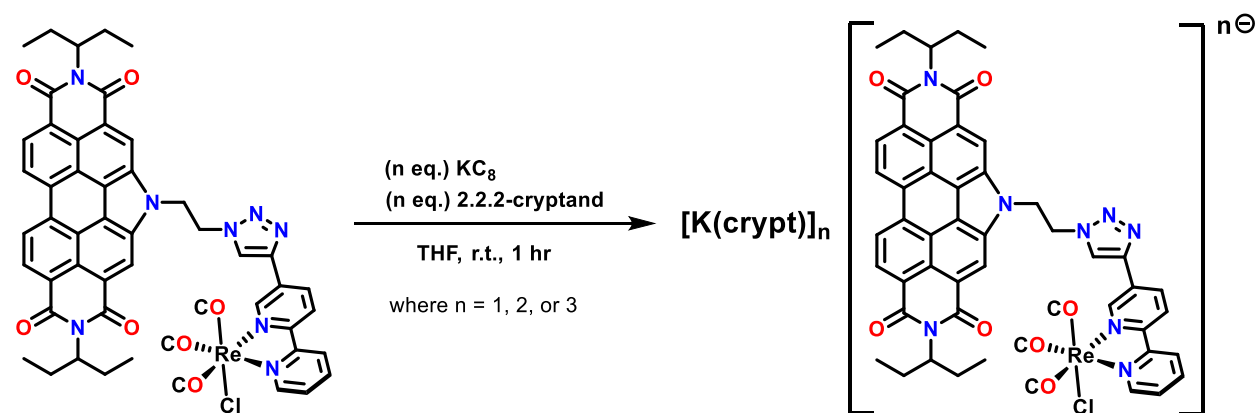
CHN theoretical (%) C: 55.76, H: 3.67, N: 10.20; found (%) C: 55.30 H: 3.75, N: 9.98;

UV-vis λ ($\times 10^4 \text{ M}^{-1} \text{ cm}^{-1}$): 307 nm (2.1); 343 nm (1.6); 456 nm (1.7); 487 nm (3.2); 521 nm (6.0)

FTIR ν_{co} (cm^{-1}): 1901, 1920, and 2024 in CH_2Cl_2 ; 1895, 1915, and 2019 in DMF.

Chemical Reduction of Re(bpy-TAz-PDI)

General chemical reduction procedure was modified from an existing literature procedure.¹⁴



In an argon-filled glovebox, $\text{Re}(\text{bpy-TAz-PDI})$ (15 mg, 0.014 mmol, 1 eq.) was added to a 20 mL scintillation vial and dissolved in anhydrous THF (5 mL). To the stirring solution, KC_8 (2.0 mg, 0.015 mmol, 1.1 eq.) was added in a single portion. Reaction progress was monitored by taking one drop aliquots for UV-vis and FTIR spectroscopic analyses. Upon reaction completion, 2.2.2-cryptand (5.7 mg, 0.015 mmol, 1.1 eq.) was added to the solution, which was left to stir at room temperature for 1 hour. The solution was subsequently passed through a 0.2 μm PTFE syringe filter (with small additional THF washing) and then taken out of the glovebox. Solvent

was removed *in vacuo* on a Schlenk line to yield the highly air-sensitive one-electron reduced product, [K(crypt)][Re(bpy-TAz-PDI)], in quantitative yield. Appropriately scaling the total equivalents of KC₈ and 2.2.2-cryptand to 2.1 eq. or 3.1 eq., the same procedure was applied to acquire the two- or three- electron reduced products, [K(crypt)]₂[Re(bpy-TAz-PDI)] and [K(crypt)]₃[Re(bpy-TAz-PDI)], respectively.

[K(crypt)][Re(bpy-TAz-PDI)]

¹H NMR (500 MHz, CD₃CN) δ 9.07 (br s), 8.97 (br s), 8.19 (br s), 8.00 (br s), 7.54 (br s), 3.49 (br s, K[crypt]), 3.44 (br s, K[crypt]), 2.44 (br s, K[crypt]), 0.62 (br s), -0.40 (br s).

μ_{eff} (THF, Evans, 25 °C) = 2.04 μB (S = 1/2).

UV-vis λ (* = major): 322 nm; 487 nm; 509 nm; 690 nm*; 780 nm

FTIR ν_{co} (KBr): 1888 cm⁻¹, 1913 cm⁻¹, and 2017 cm⁻¹

[K(crypt)]₂[Re(bpy-TAz-PDI)]

¹H NMR (500 MHz, CD₃CN) δ 8.84 (m, 2H), 8.62 (d, J = 4.6 Hz, 2 H), 8.36 (d, J = 8.2 Hz, 2 H), 8.32 (d, J = 8.2, 2H), 8.13 (s, 2 H), 8.07-8.00 (m, 2 H), 7.84 (td, J = 7.6 Hz, 1.43 Hz, 2 H), 7.24-7.17 (m), 7.00-6.86 (m, 1H) 6.77-6.62 (m, 2H), 5.34 (t, 4.68 Hz, 1H), 3.58 (s, crypt), 3.52 (t, J = 5.7 Hz, crypt), 3.39 (s, K[crypt]), 3.34 (t, J = 4.7 Hz, K[crypt]), 2.56 (t, J = 5.7 Hz, crypt), 2.34 (t, J = 4.7 Hz, K[crypt]), 0.70 (m).

UV-vis λ (* = major) : 321 nm; 585 nm; 621 nm*; 653 nm*; 693 nm

FTIR ν_{co} (KBr): 1888 cm⁻¹, 1913 cm⁻¹, and 2017 cm⁻¹

[K(crypt)]₃[Re(bpy-TAz-PDI)]

¹H NMR (500 MHz, CD₃CN) δ 3.48 (s, 12H, K[crypt]), 3.44 (t, 12 H, J = 4.7 Hz, K[crypt]), 2.44 (t, 12H, J = 4.7 Hz).

μ_{eff} (THF, Evans, 25 °C) = 1.94 μB (S = 1/2).

UV-vis λ (* = major) : 321 nm; 585 nm; 621 nm*; 653 nm*; 693 nm

FTIR ν_{co} (KBr): 1852 cm⁻¹, 1877 cm⁻¹, and 1980 - 1992 cm⁻¹

3. ^1H & ^{13}C NMR and EPR Spectroscopies

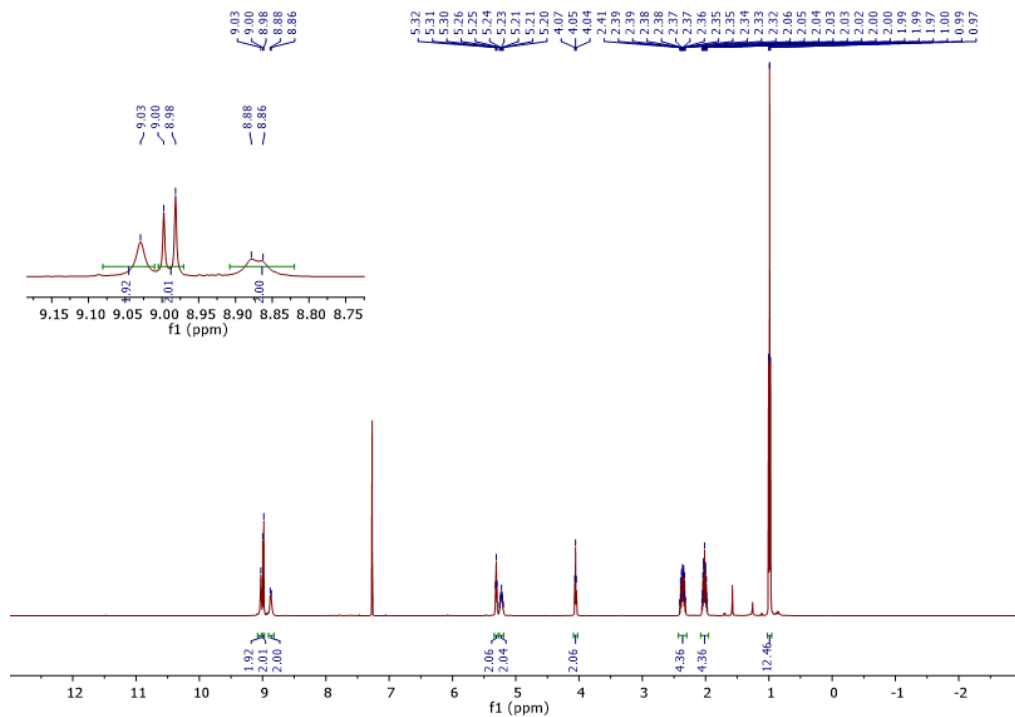


Figure S1. ^1H NMR spectrum of BrEt-PDI (500 MHz, CDCl_3)

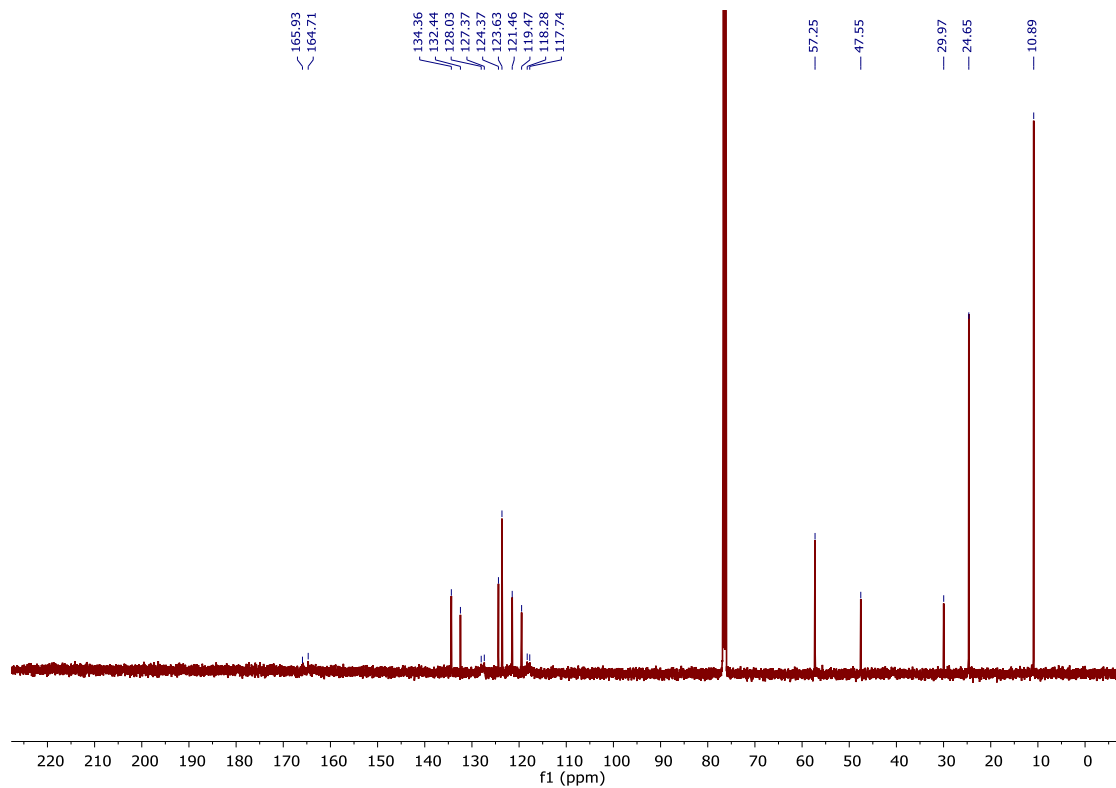


Figure S2. $^{13}\text{C}\{^1\text{H}\}$ NMR spectrum of BrEt-PDI (126 MHz, CDCl_3)

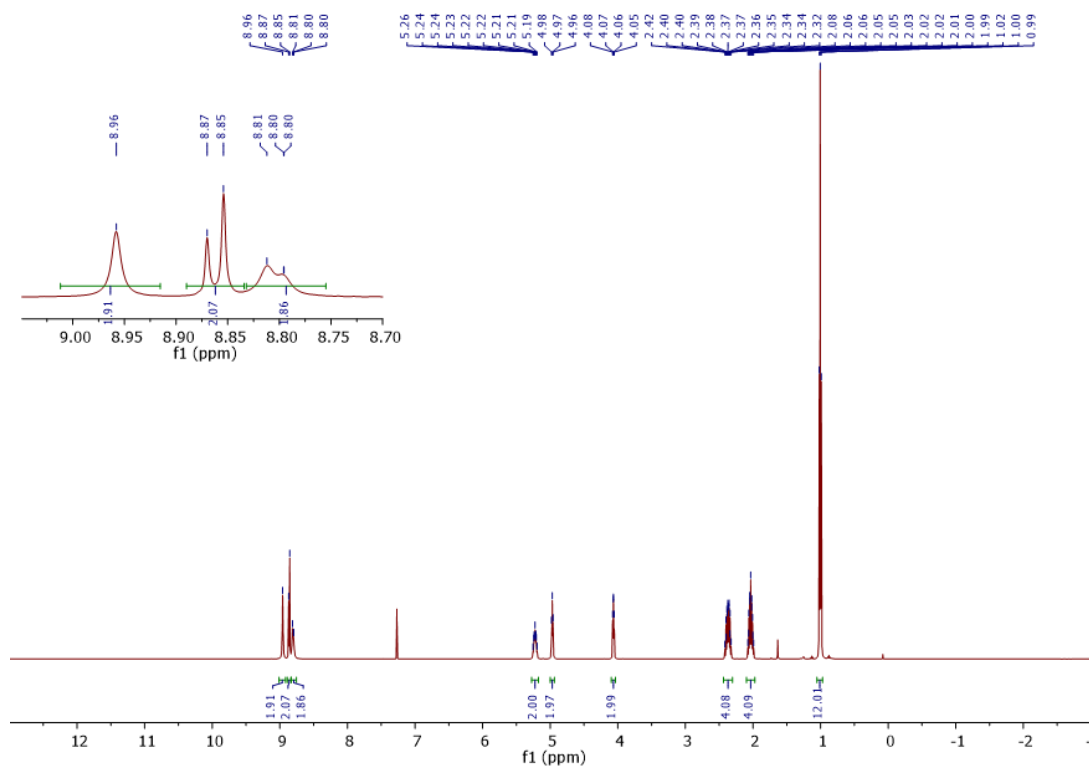


Figure S3. ^1H NMR spectrum of $\text{N}_3\text{-PDI}$ (500 MHz, CDCl_3)

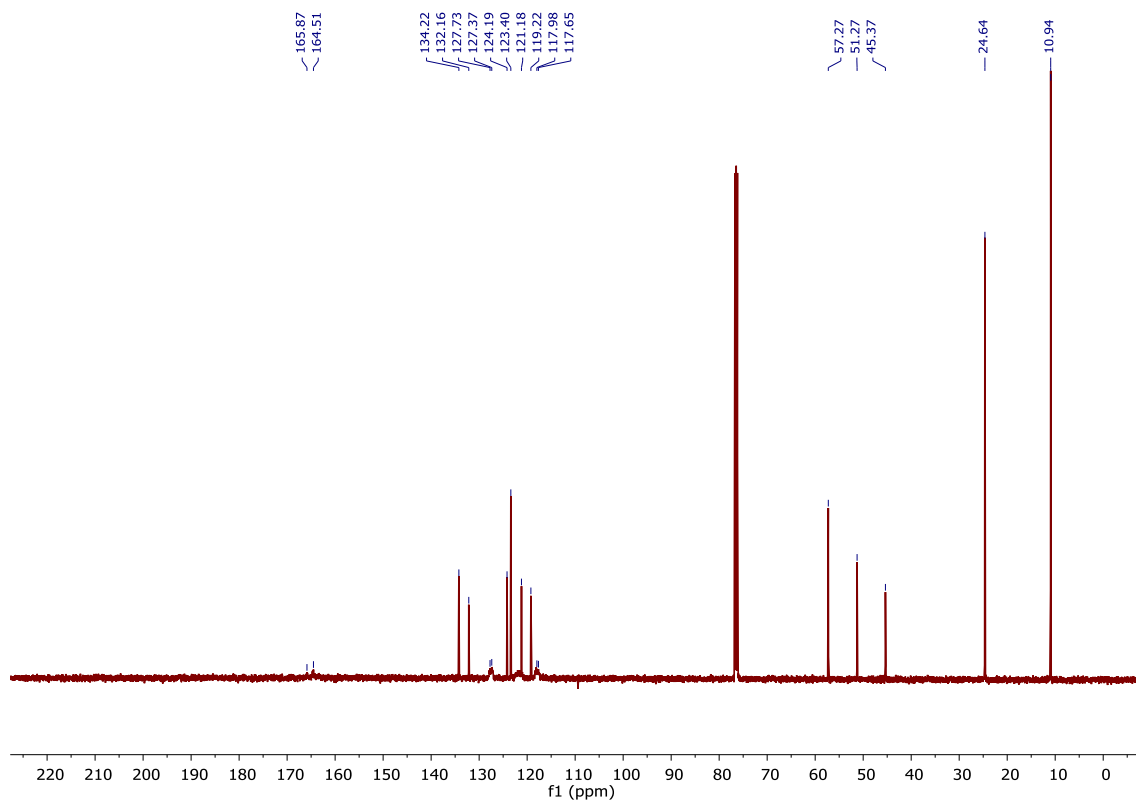


Figure S4. $^{13}\text{C}\{^1\text{H}\}$ NMR spectrum of $\text{N}_3\text{-PDI}$ (126 MHz, CDCl_3)

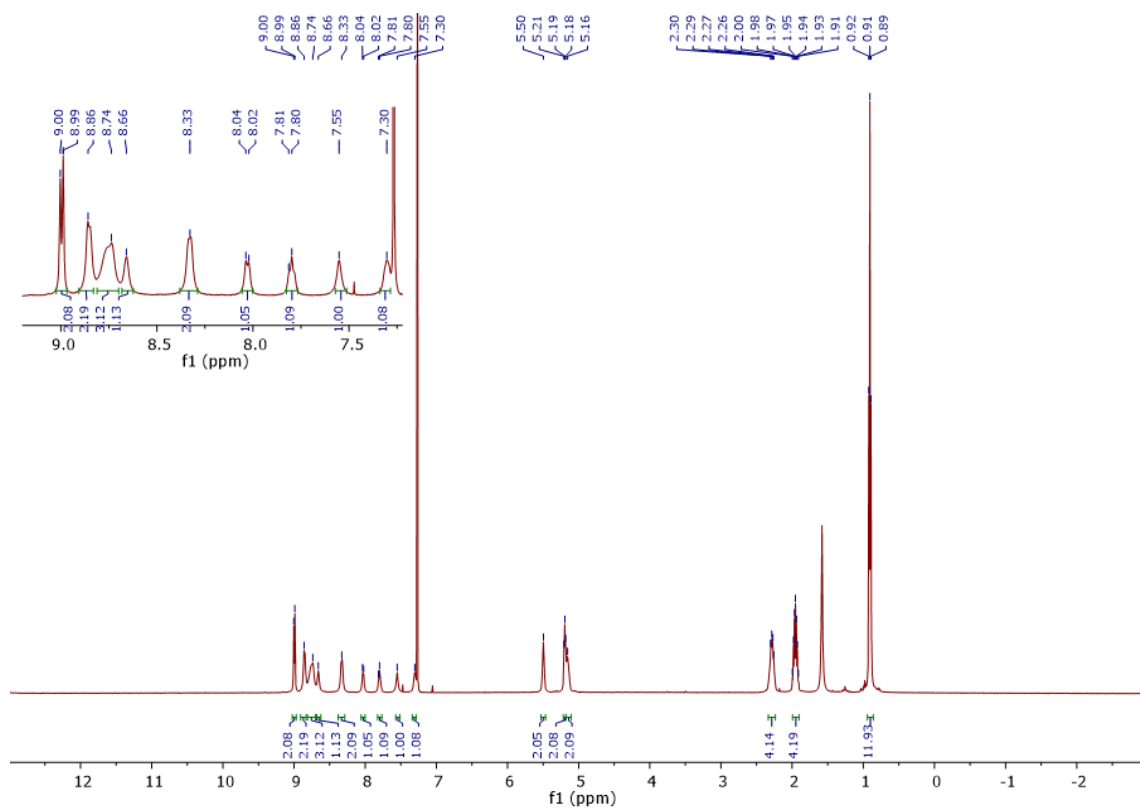


Figure S5. ^1H NMR spectrum of bpy-TAz-PDI (500 MHz, CDCl_3)

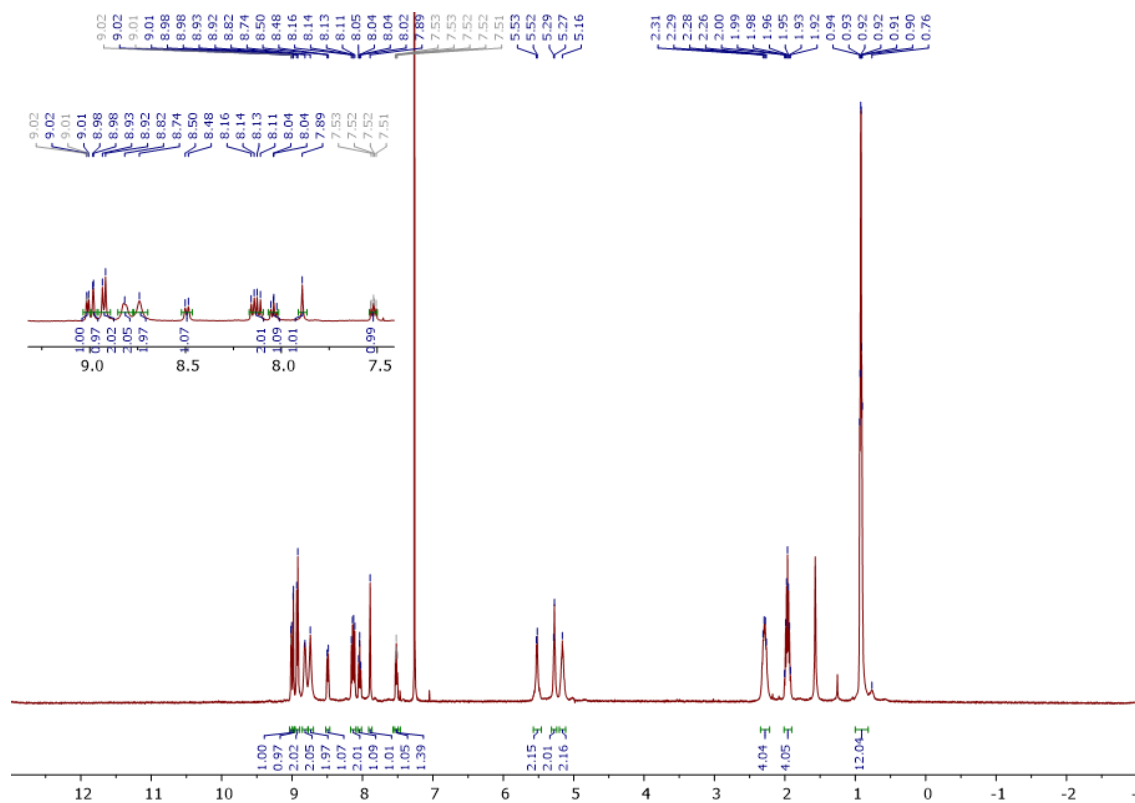


Figure S6. ^1H NMR spectrum of Re(bpy-TAz-PDI) (500 MHz, CDCl_3)

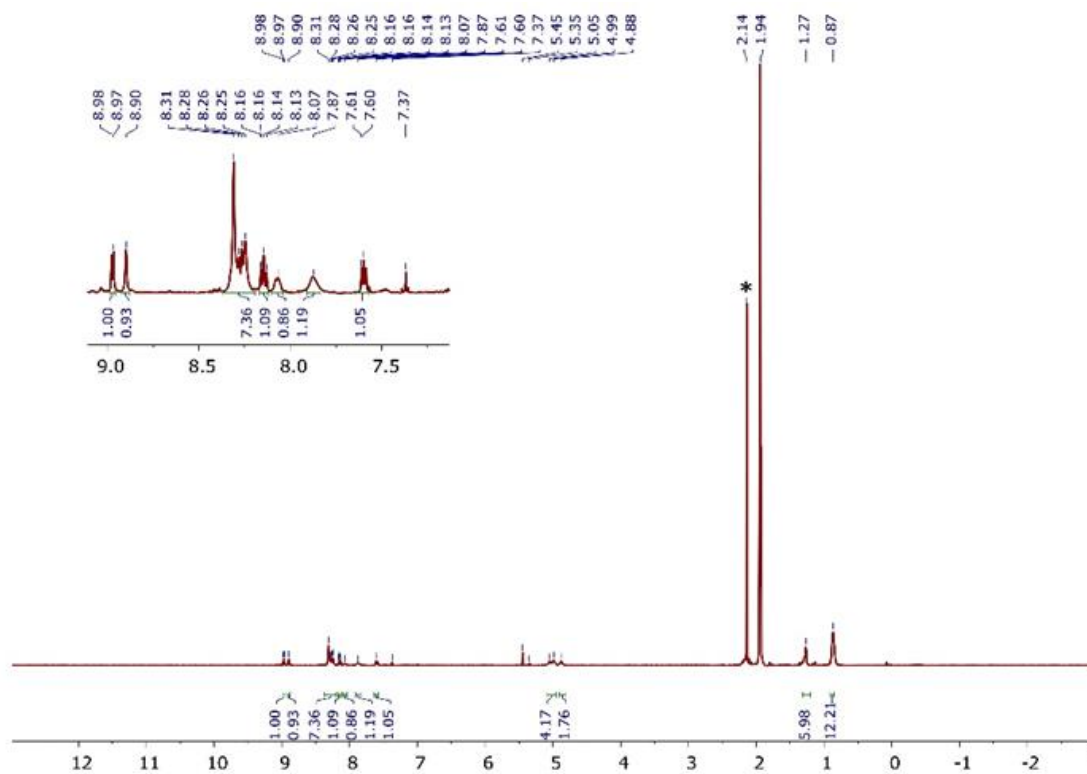


Figure S7. ^1H NMR spectrum of Re(bpy-TAz-PDI) (500 MHz, CD_3CN); * = solvent impurity

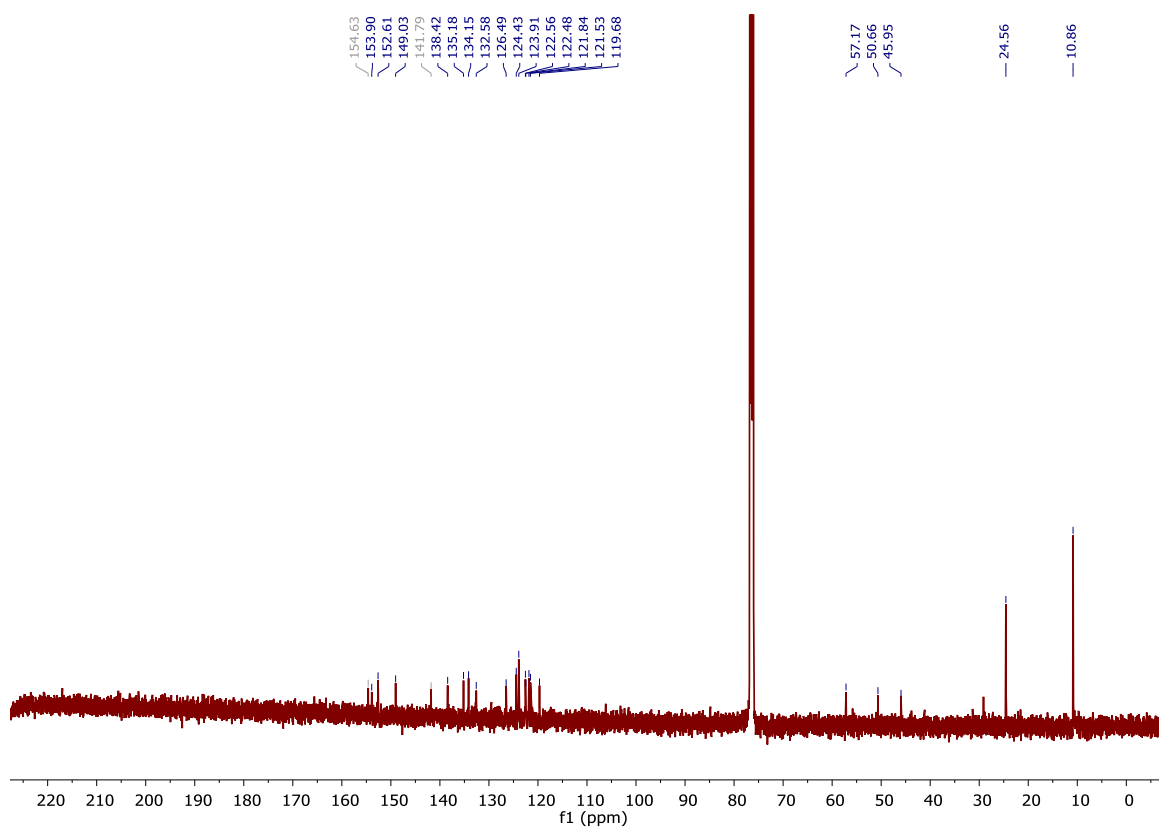


Figure S8. $^{13}\text{C}\{^1\text{H}\}$ NMR spectrum of Re(bpy-TAz-PDI) (126 MHz, CDCl_3)

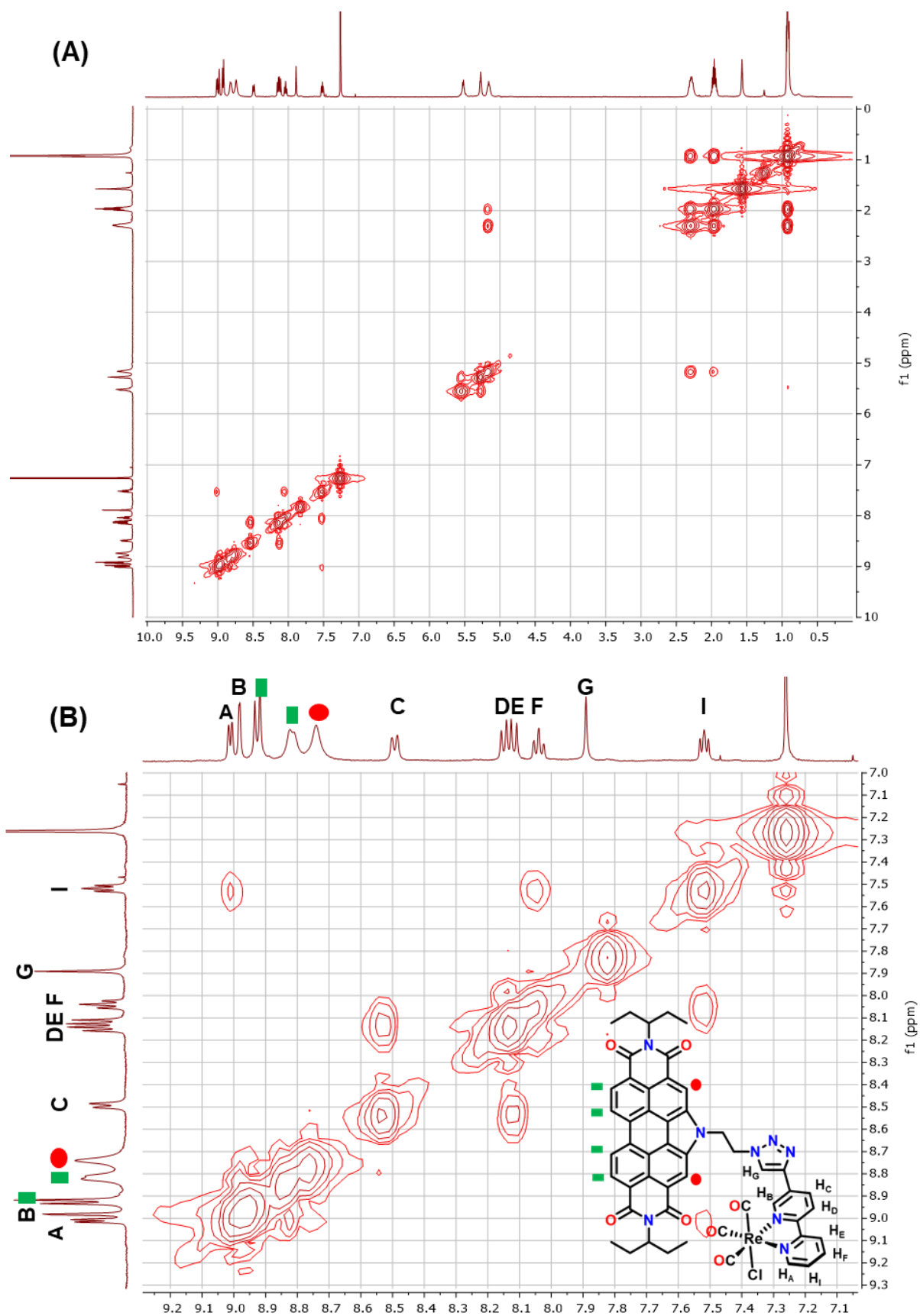


Figure S9. ^1H - ^1H COSY spectrum (A) and assignment of aromatic peaks (B) of $\text{Re}(\text{bpy-TAz-PDI})$ (500 MHz, CDCl_3)

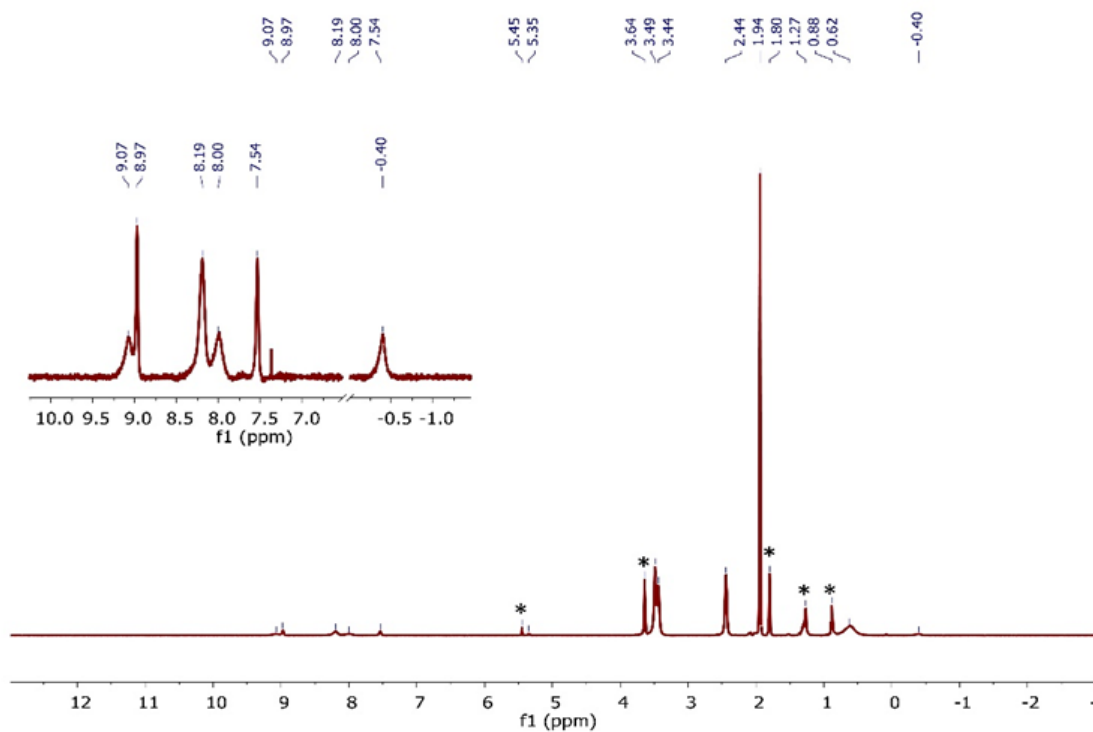


Figure S10. ^1H NMR spectrum of $[\text{K}(\text{crypt})][\text{Re}(\text{bpy-TAz-PDI})]$ (500 MHz, CD_3CN); * = solvent impurities ¹⁵

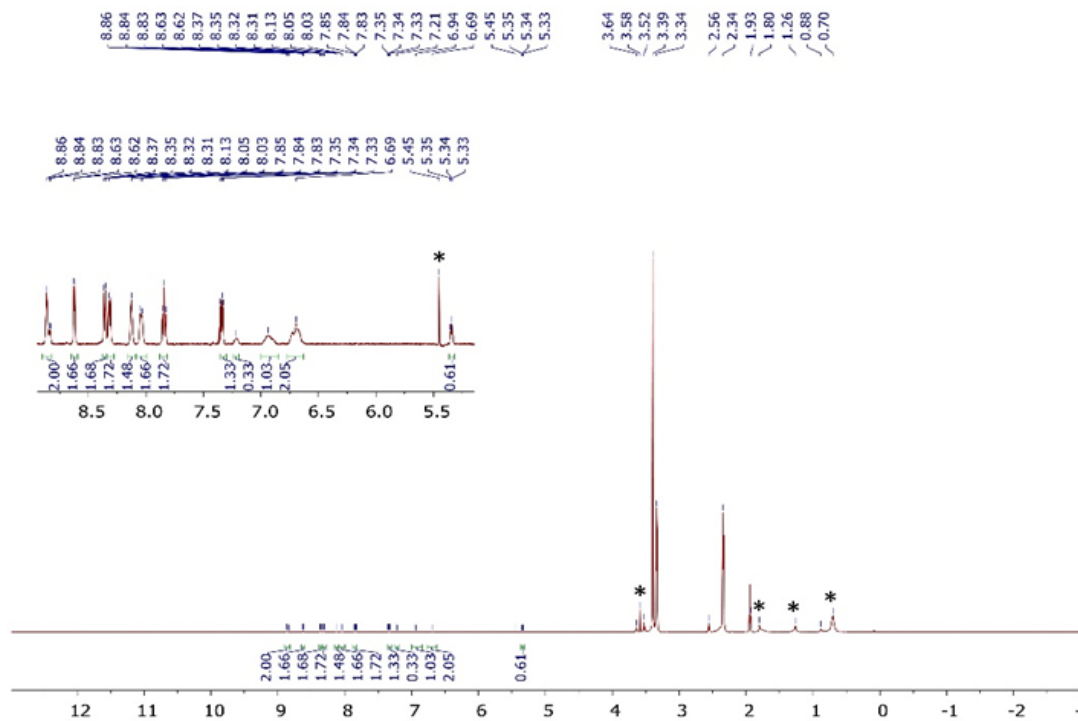


Figure S11. ^1H NMR spectrum of $[\text{K}(\text{crypt})]_2[\text{Re}(\text{bpy-TAz-PDI})]$ (500 MHz, CD_3CN); * = solvent impurities ¹⁵

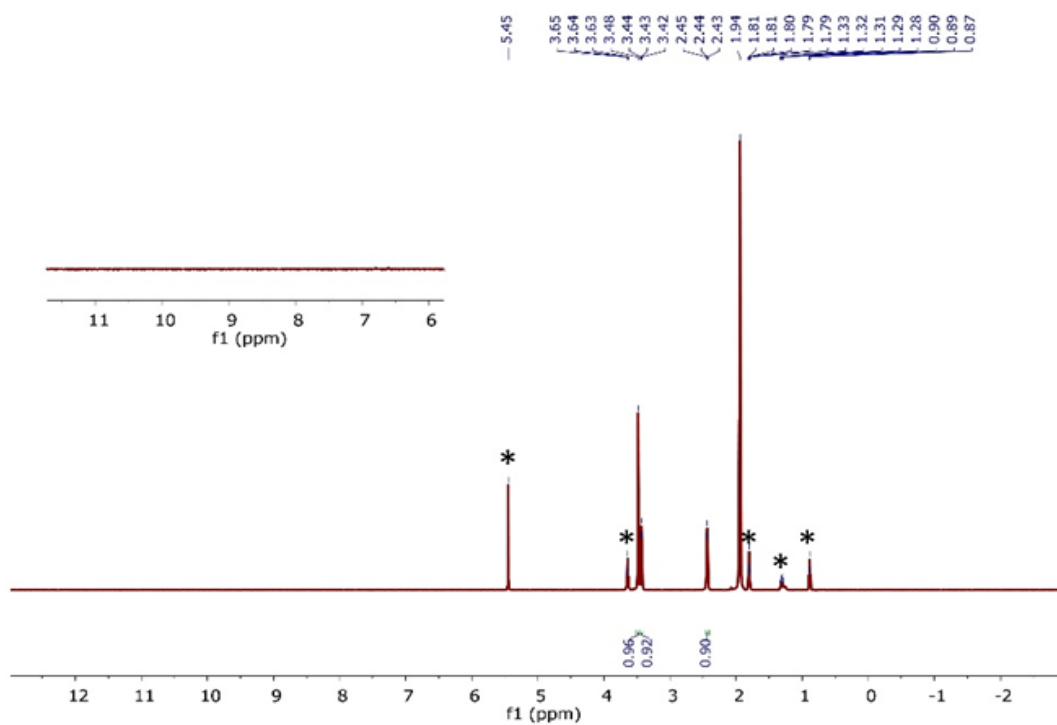


Figure S12. ^1H NMR spectrum of $[\text{K}(\text{crypt})]_3[\text{Re}(\text{bpy-TAz-PDI})]$ (500 MHz, CD_3CN); * = solvent impurities ¹⁵

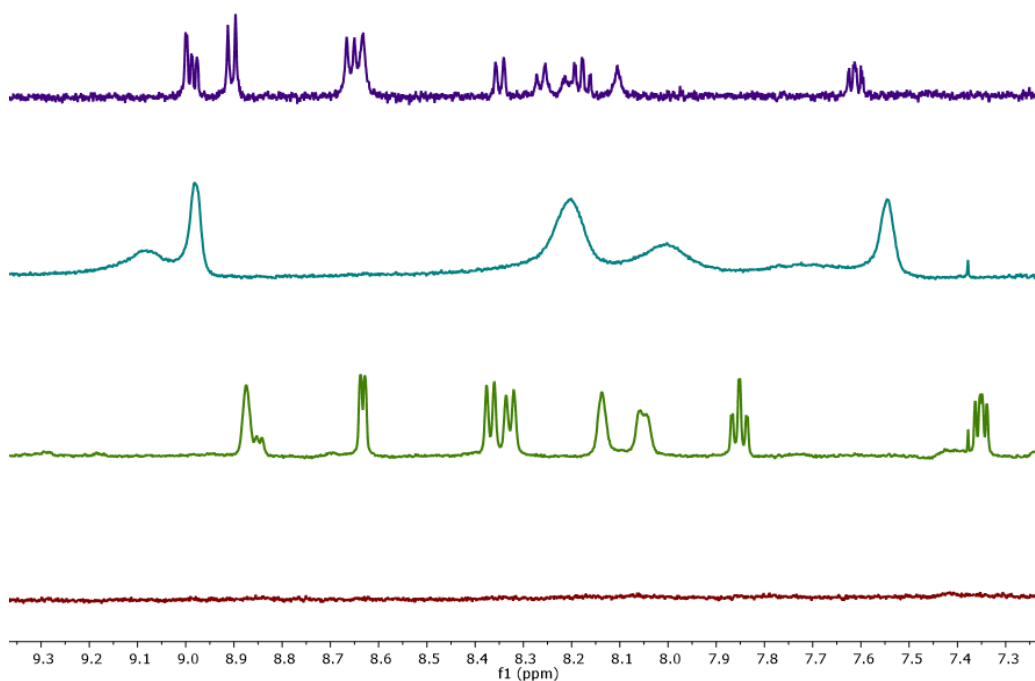


Figure S13. Enhanced view of aromatic ^1H NMR resonances (500 MHz, CD_3CN) for $\text{Re}(\text{bpy-TAz-PDI})$ (purple), $[\text{K}(\text{crypt})][\text{Re}(\text{bpy-TAz-PDI})]$ (teal), $[\text{K}(\text{crypt})]_2[\text{Re}(\text{bpy-TAz-PDI})]$ (green), and $[\text{K}(\text{crypt})]_3[\text{Re}(\text{bpy-TAz-PDI})]$ (red)

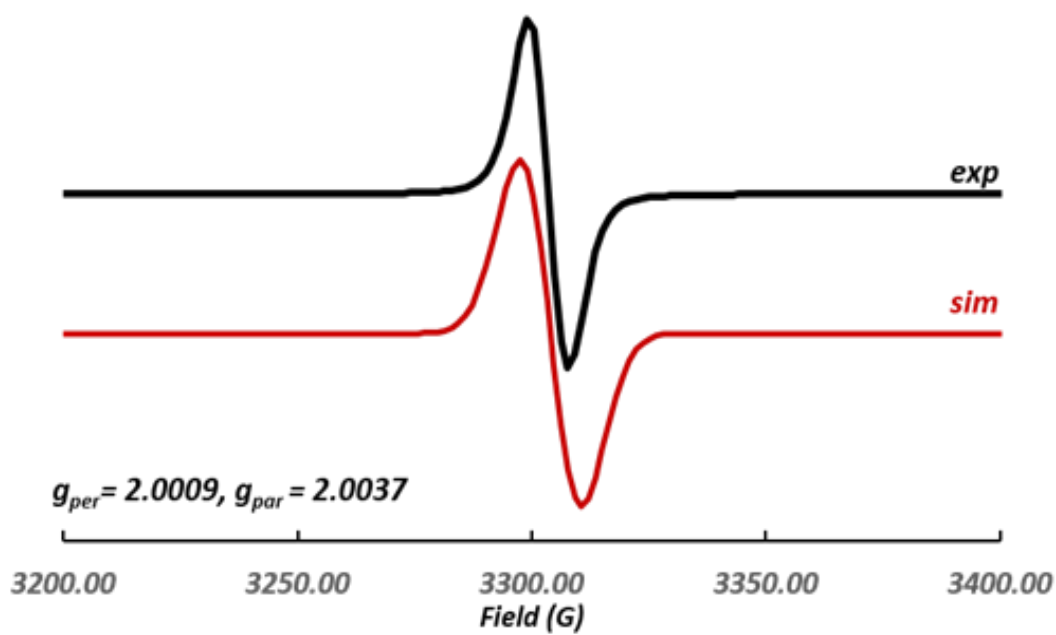


Figure S14. X-band EPR spectrum of [K(crypt)][Re(bpy-TAz-PDI)] recorded in toluene at 298K

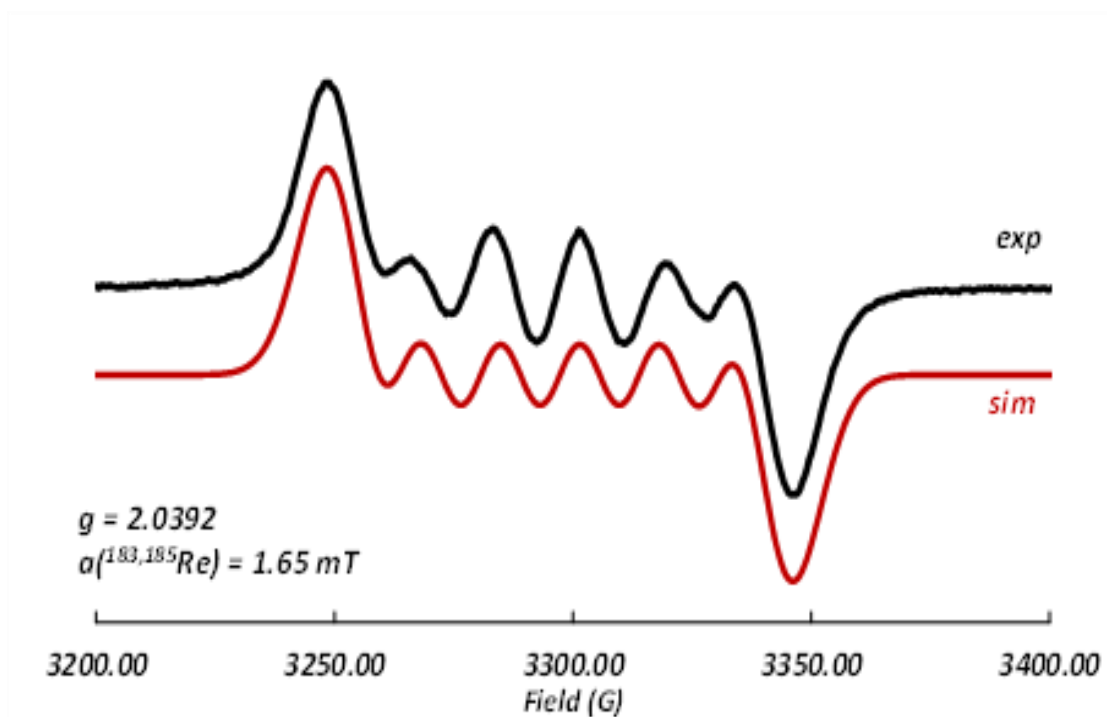


Figure S15. X-band EPR spectrum of [K(crypt)]₃[Re(bpy-TAz-PDI)]³⁻ recorded in THF at 298K

4. MALDI-TOF MS & CHN Elemental Analysis

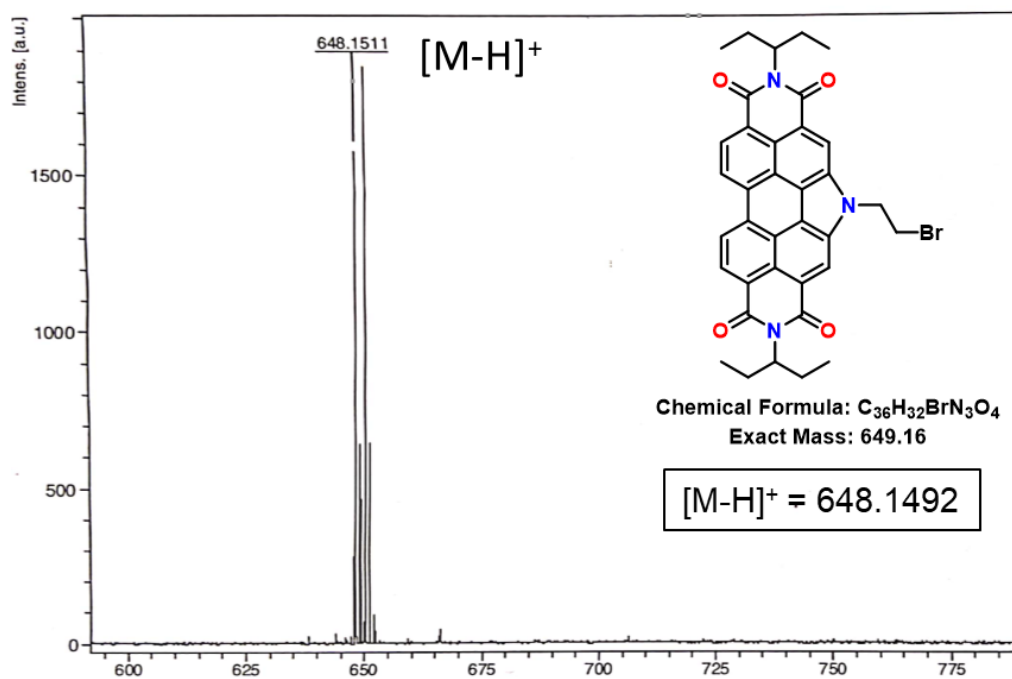


Figure S16. HR-MALDI-TOF mass spectrum of BrEt-PDI

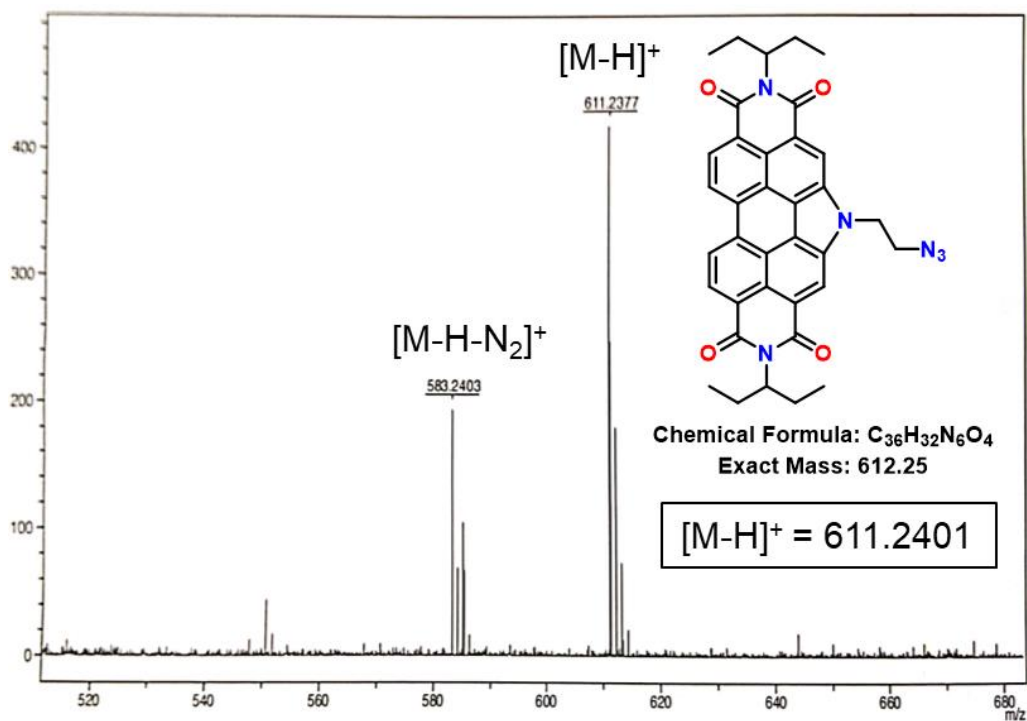


Figure S17. HR-MALDI-TOF mass spectrum of N_3 -PDI

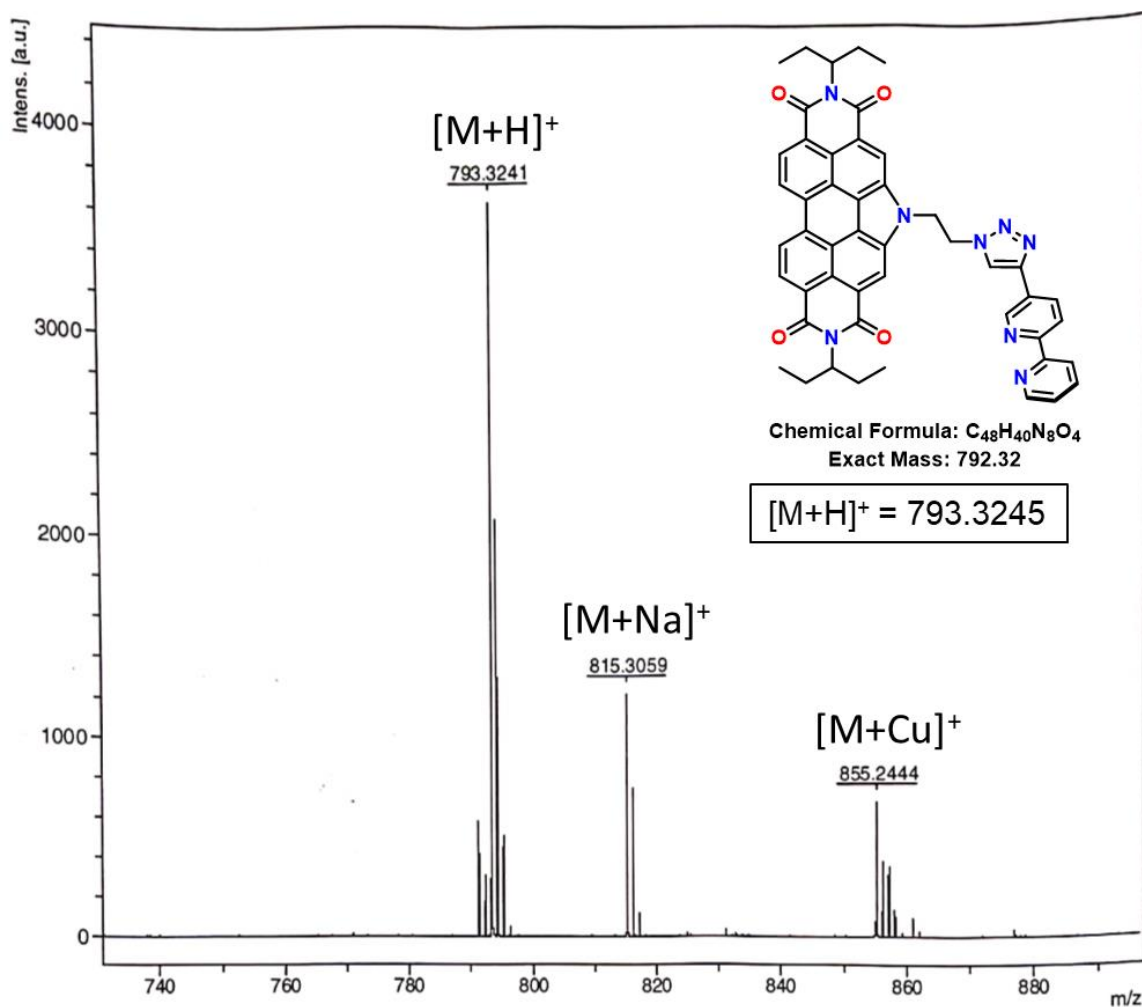


Figure S18. HR-MALDI-TOF mass spectrum of bpy-TAz-PDI

University of Calgary

Department of Chemistry EA

Date: 2/6/2019

| | | | |
|--------------|--------------------|-------------------|-------|
| Name: | JOSH | Group: | GW |
| Sample: | bpy-TAz-PDI | Weight (mg): | 0.856 |
| %C (Actual): | 72.49 | %C (Theoretical): | 72.71 |
| %H (Actual): | 4.99 | %H (Theoretical): | 5.09 |
| %N (Actual): | 13.68 | %N (Theoretical): | 14.13 |

Figure S19. CHN elemental analysis of bpy-TAz-PDI

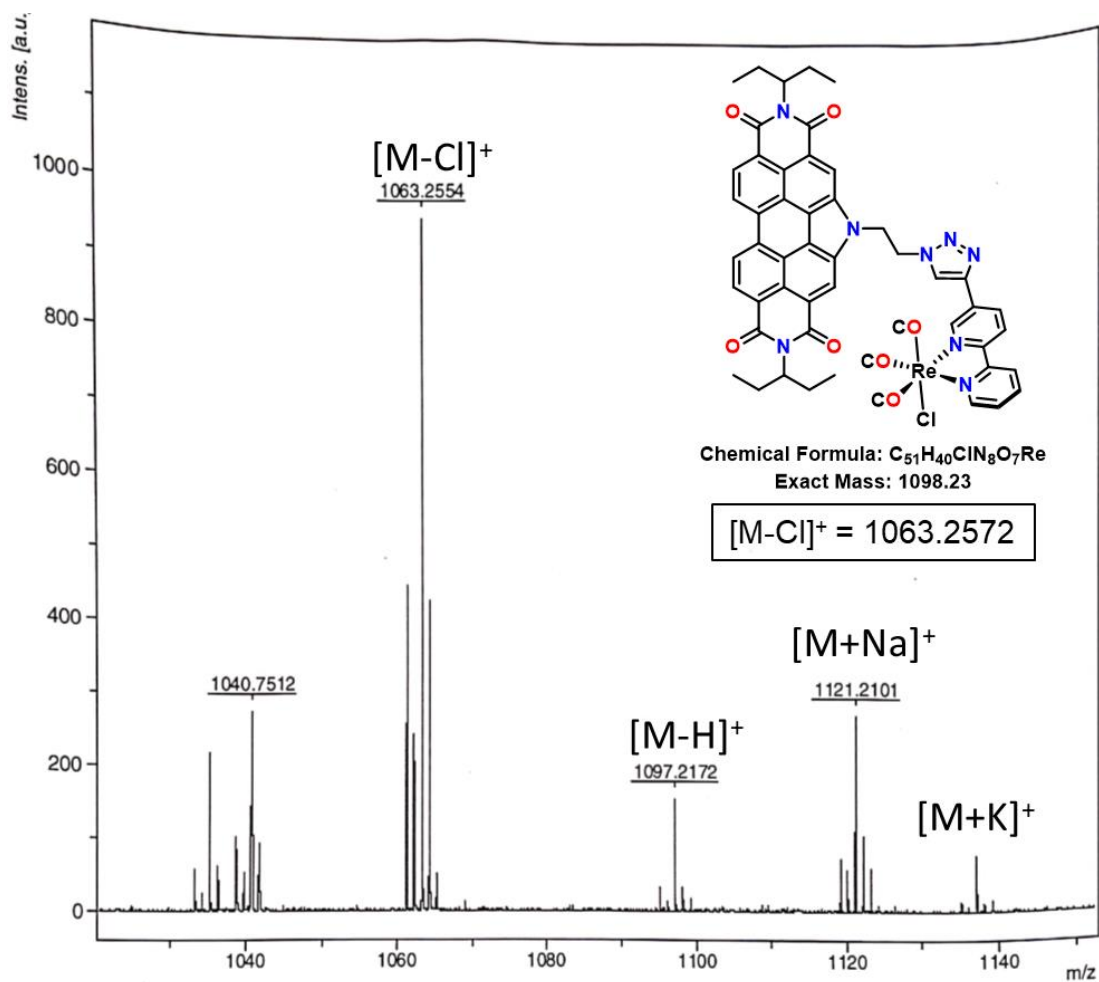


Figure S20. HR-MALDI-TOF mass spectrum of Re(bpy-TAz-PDI)

University of Calgary

Department of Chemistry EA

Date: 2/6/2019

| | | | |
|--------------|------------------------|-------------------|-------|
| Name: | JOSH | Group: | GW |
| Sample: | Re(bpy-TAz-PDI) | Weight (mg): | 1.588 |
| %C (Actual): | 55.30 | %C (Theoretical): | 55.76 |
| %H (Actual): | 3.75 | %H (Theoretical): | 3.67 |
| %N (Actual): | 9.98 | %N (Theoretical): | 10.20 |

Figure S21. CHN elemental analysis of Re(bpy-TAz-PDI)

5. UV-Vis & FTIR Spectroscopy

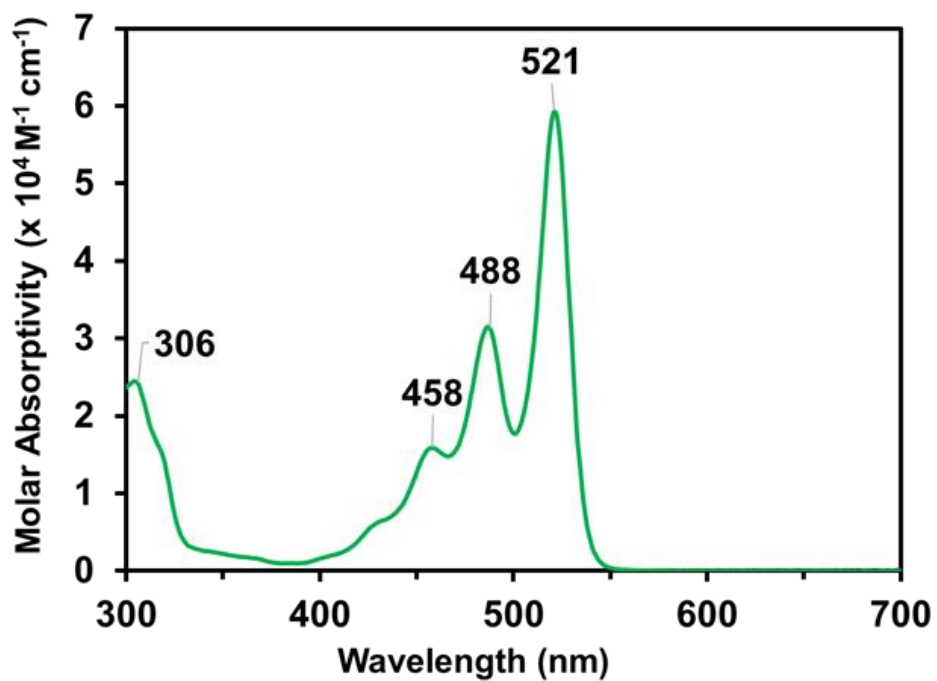


Figure S22. UV-vis absorption spectrum of bpy-TAz-PDI in CHCl₃

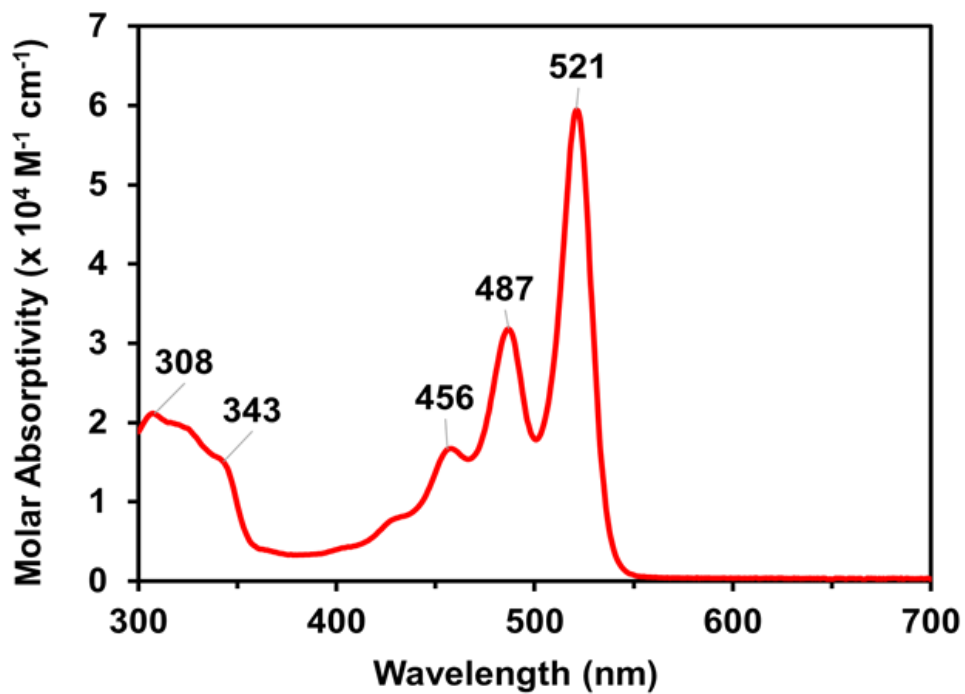


Figure S23. UV-vis absorption spectrum of Re(bpy-TAz-PDI) in CHCl₃

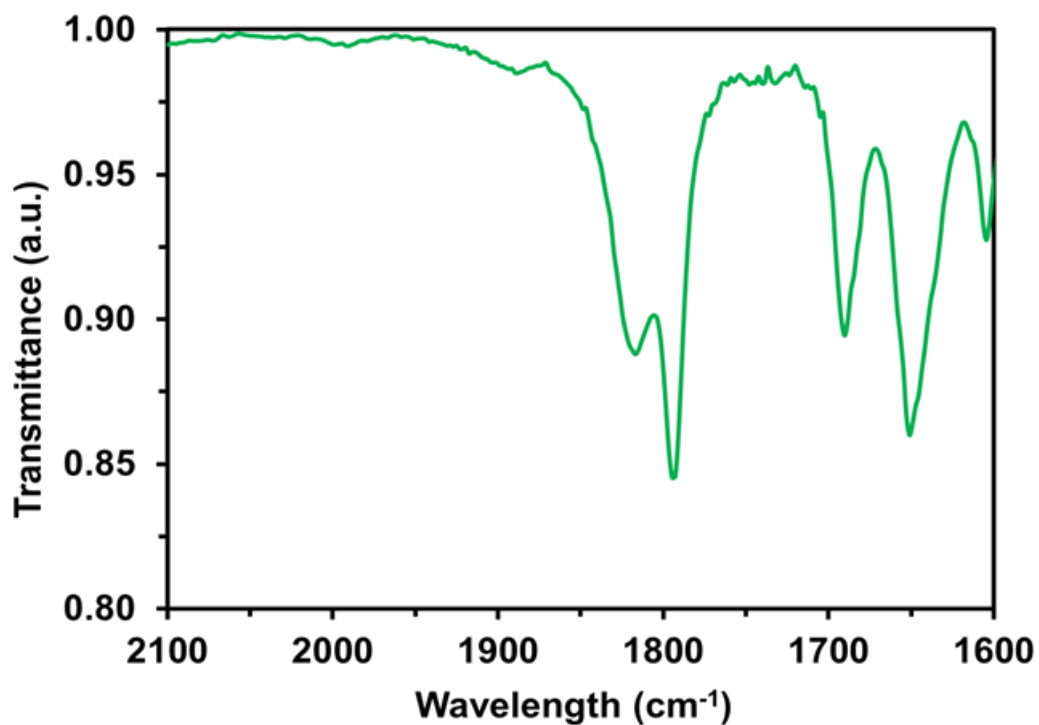


Figure S24. FTIR transmission spectrum of bpy-TAz-PDI in CH₂Cl₂

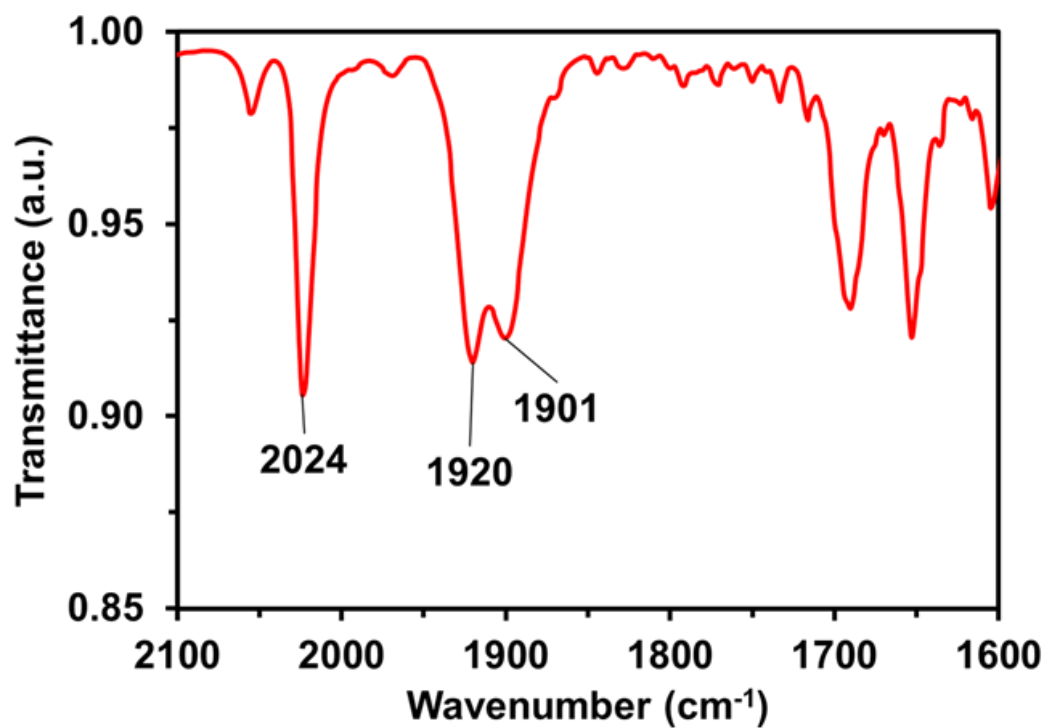


Figure S25. FTIR transmission spectrum of Re(bpy-TAz-PDI) in CH₂Cl₂

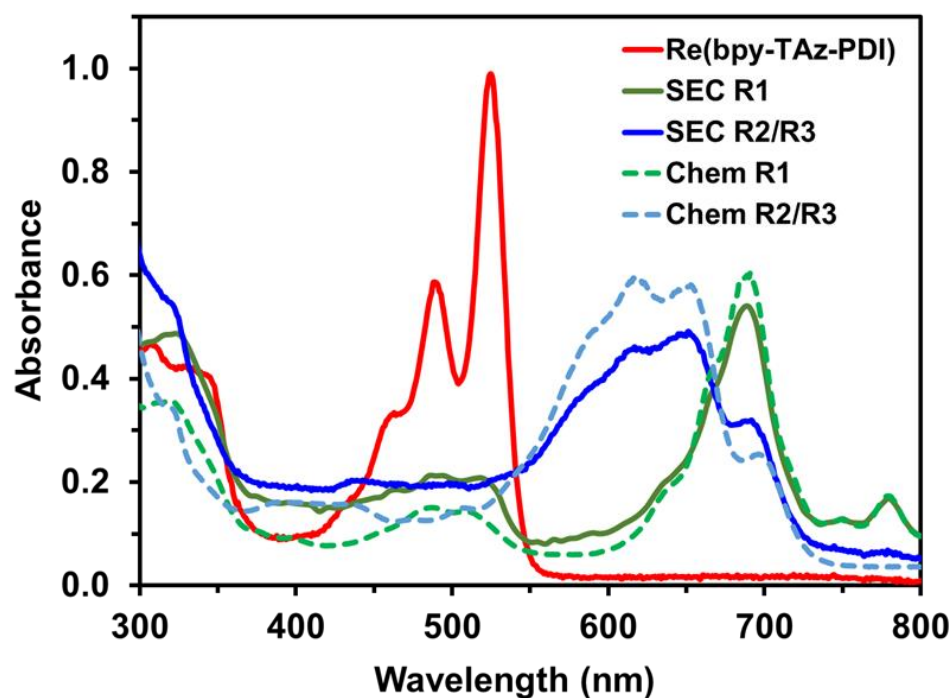


Figure S26. Comparing the UV-vis-nIR absorption spectra of electrochemically reduced (solid lines) and chemically reduced (dashed lines) Re(bpy-TAz-PDI) species, where R1, R2, and R3 denote the singly-, doubly-, and triply- reduced products

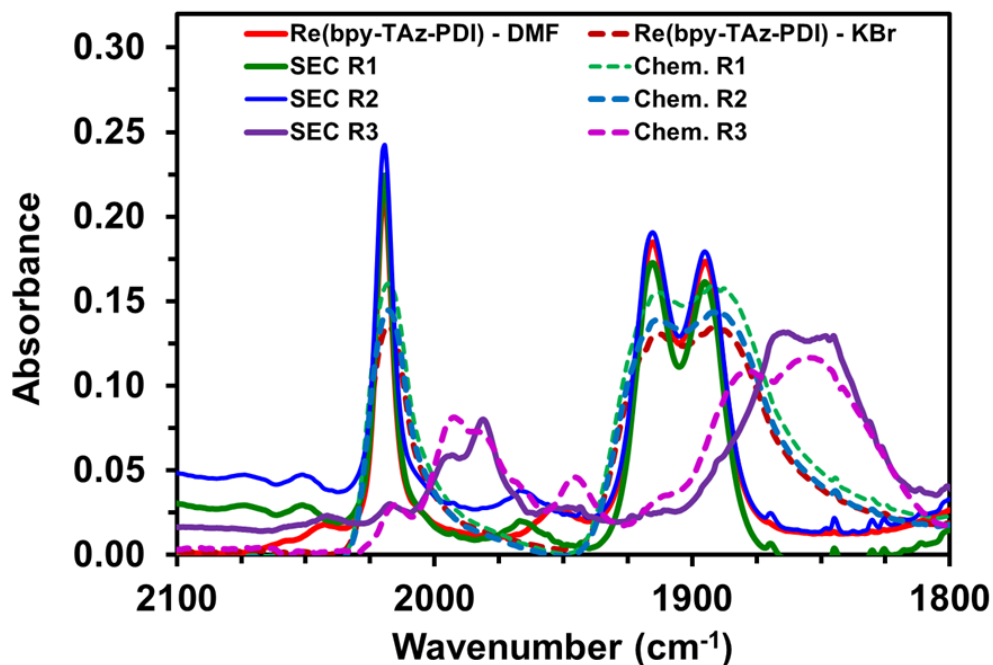


Figure S27. Comparing the FTIR absorption spectra of electrochemically reduced (solid lines) and chemically reduced (dashed lines) Re(bpy-TAz-PDI) species, where R1, R2, and R3 denote the singly-, doubly-, and triply- reduced products

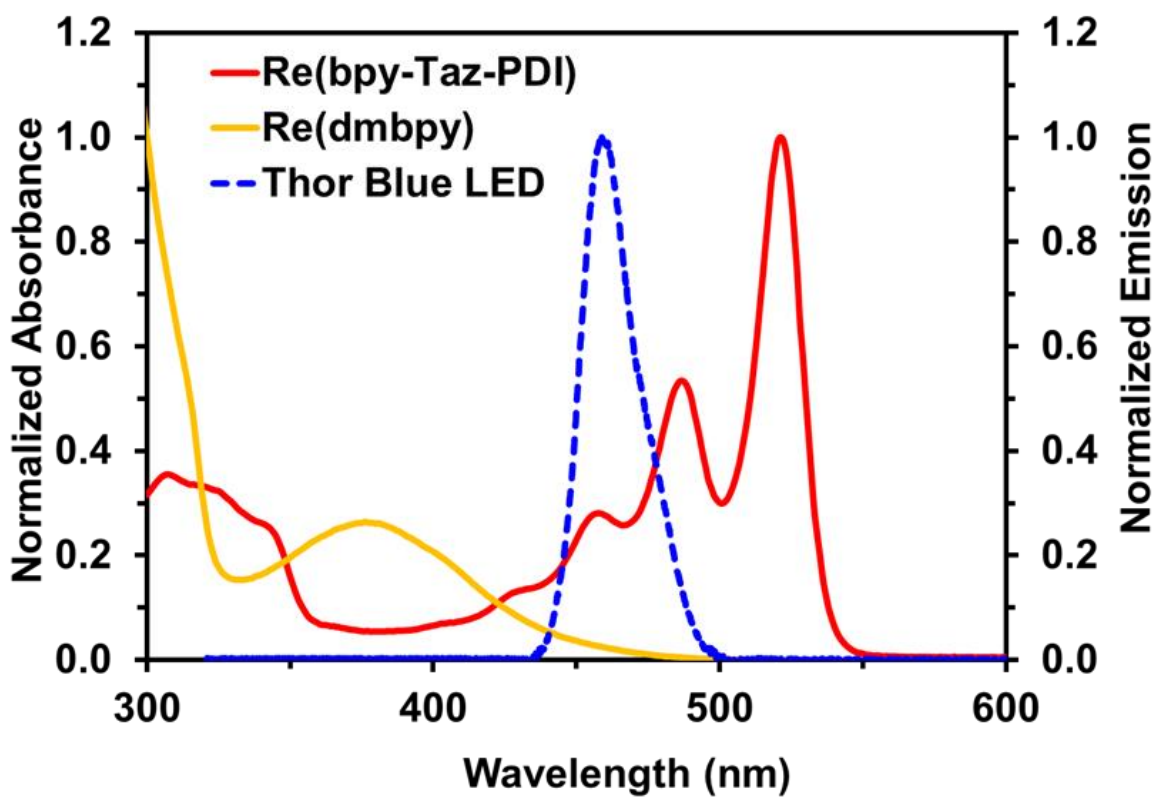


Figure S28. UV-vis absorbance spectra of Re(bpy-TAz-PDI) (red) and Re(dmbpy) (yellow), overlaid with the UV-vis emission spectrum of the Thor Labs Blue LED (dashed blue)

6. Cyclic Voltammetry & Spectroelectrochemistry

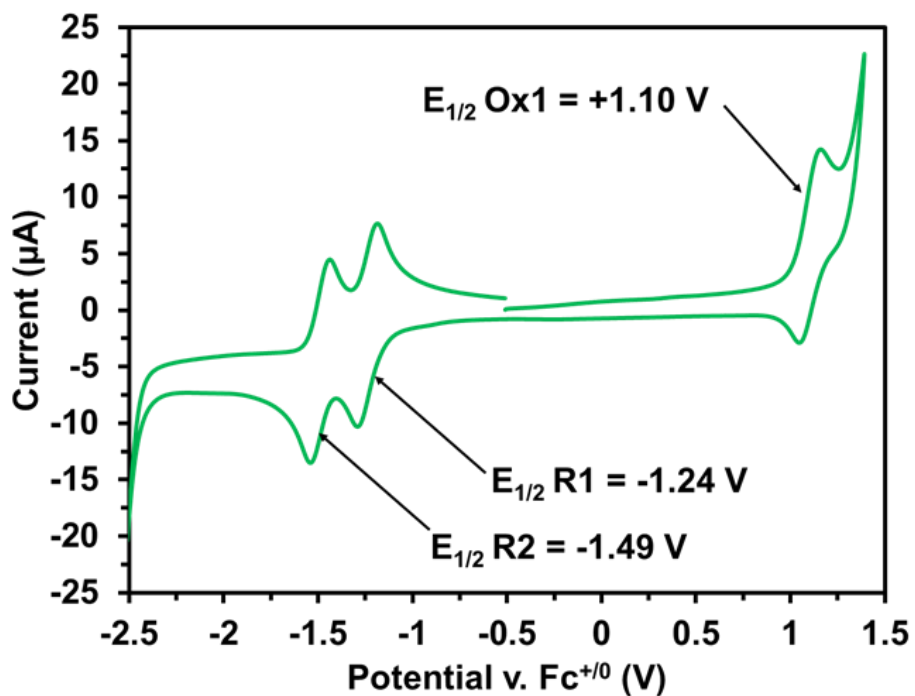


Figure S29. CV of bpy-TAz-PDI recorded at 100 mV/s, under argon in CH_2Cl_2 with 0.1 M TBAPF₆ as supporting electrolyte and $\text{Fc}^{+/0}$ as internal reference

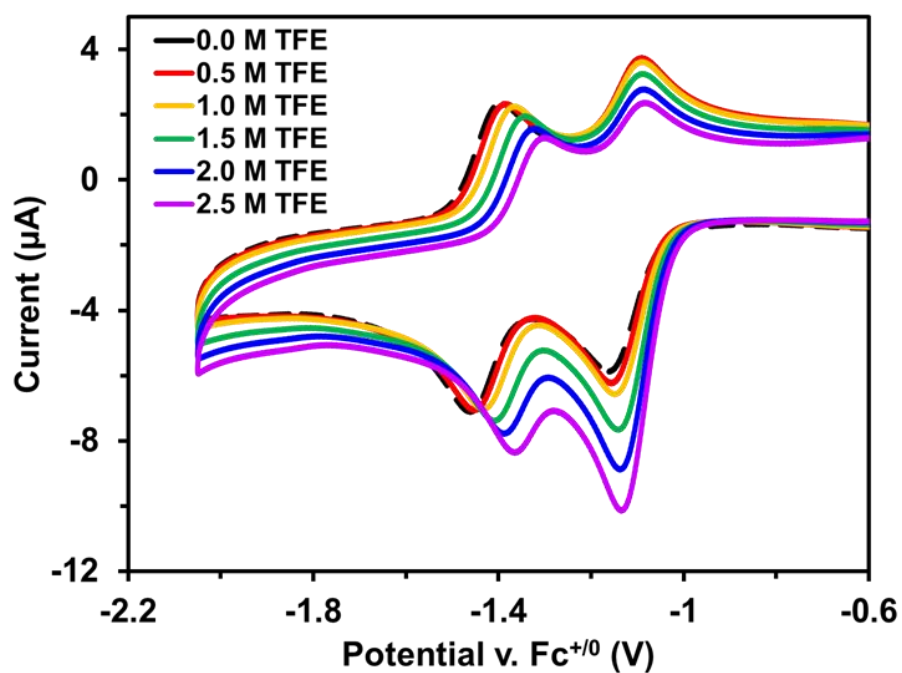


Figure S30. CV of bpy-TAz-PDI as a function of TFE concentration, recorded at 100 mV/s, under argon in DMF with 0.1 M TBAPF₆ as supporting electrolyte and $\text{Fc}^{+/0}$ as internal reference

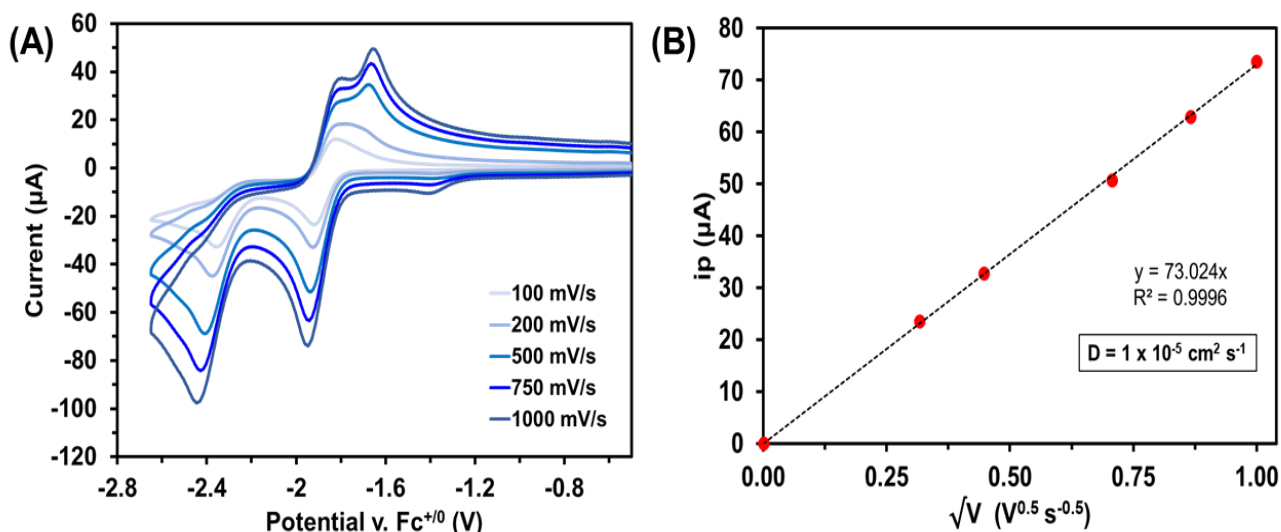


Figure S31. CVs of Re(dmbpy) recorded at variable scan rate (A), under argon in DMF with 0.1 M TBAPF₆ supporting electrolyte (WE = glassy carbon, CE = Pt-wire, RE = Ag/AgCl, and $\text{Fc}^{+/0}$ as internal reference standard). Linear fitting of the scan rate to the Randles-Sevcik equation (B) demonstrates that Re(dmbpy) undergoes a diffusion-limited current response

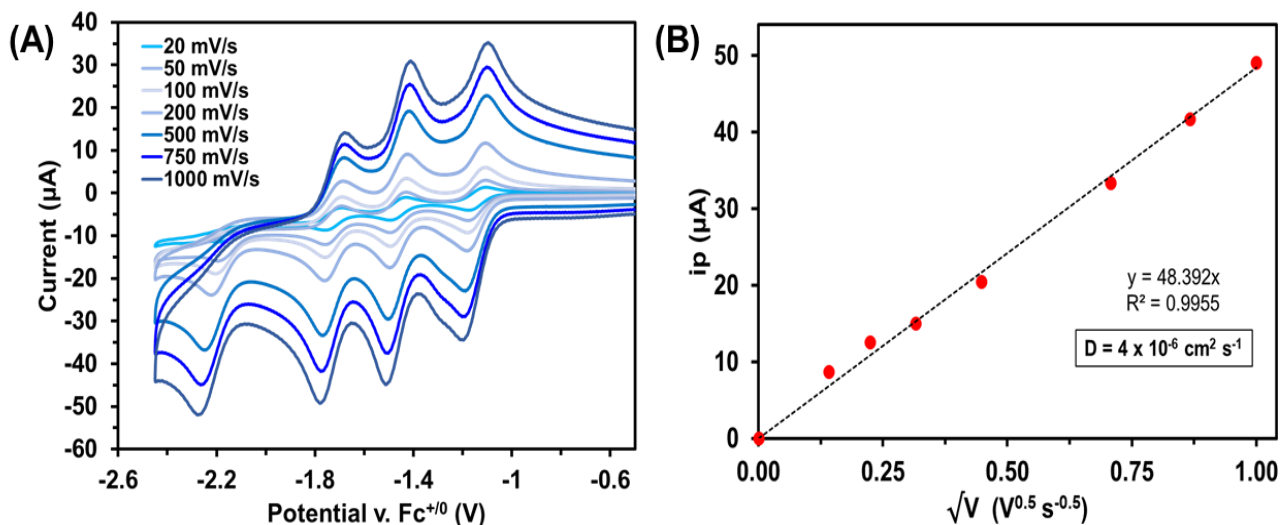


Figure S32. CVs of Re(bpy-TAz-PDI) recorded at variable scan rate (A), under argon in DMF with 0.1 M TBAPF₆ supporting electrolyte (WE = glassy carbon, CE = Pt-wire, RE = Ag/AgCl, and $\text{Fc}^{+/0}$ as internal reference standard). Linear fitting of the scan rate to the Randles-Sevcik equation (B) demonstrates that Re(bpy-TAz-PDI) undergoes a diffusion-limited current response

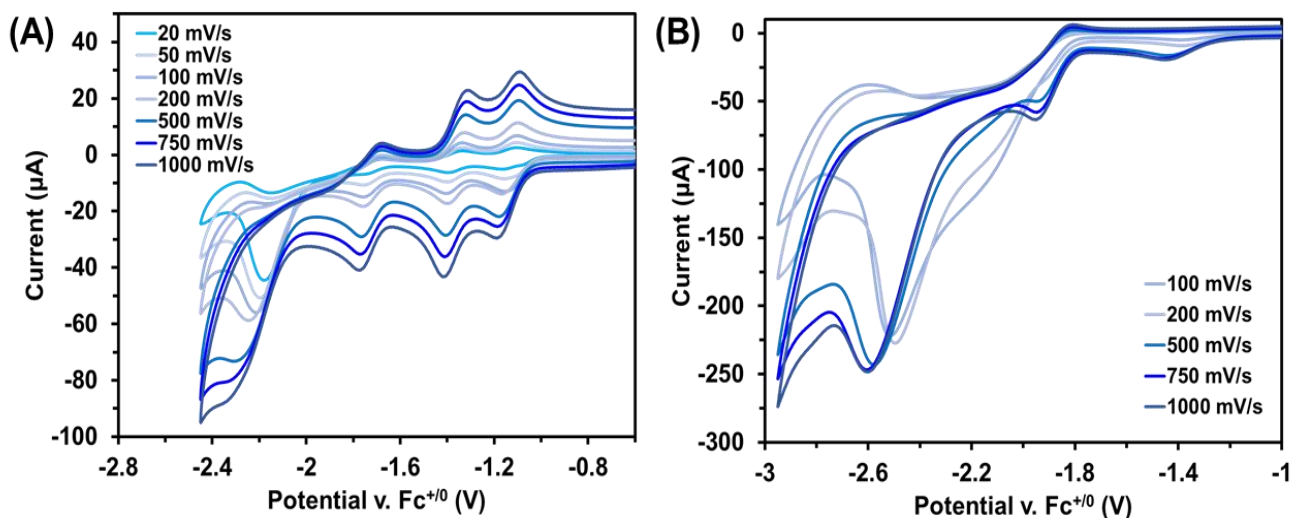


Figure S33. CVs of Re(bpy-TAz-PDI) (A) and Re(dmbpy) (B) recorded at variable scan rate (A), under CO₂-saturated DMF with 2.0 M TFE and 0.1 M TBAPF₆ supporting electrolyte (WE = glassy carbon, CE = Pt-wire, RE = Ag/AgCl, and Fc^{+/0} as internal reference standard)

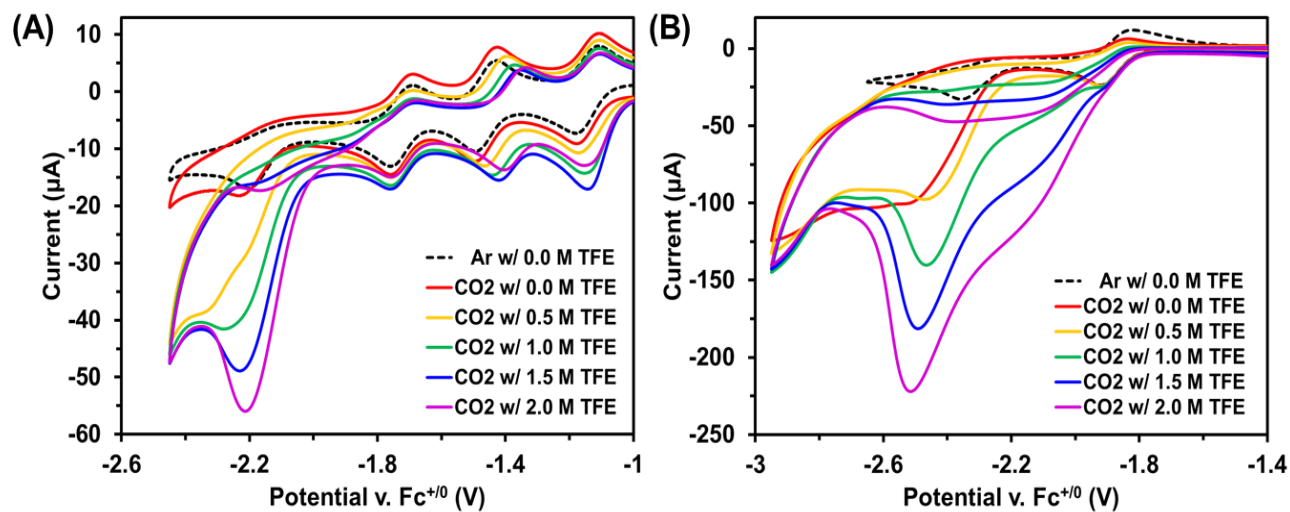


Figure S34. Comparing catalytic current enhancement of Re(bpy-TAz-PDI) (A) and Re(dmbpy) (B) in CO₂ saturated DMF solutions, as a function of proton source (TFE)

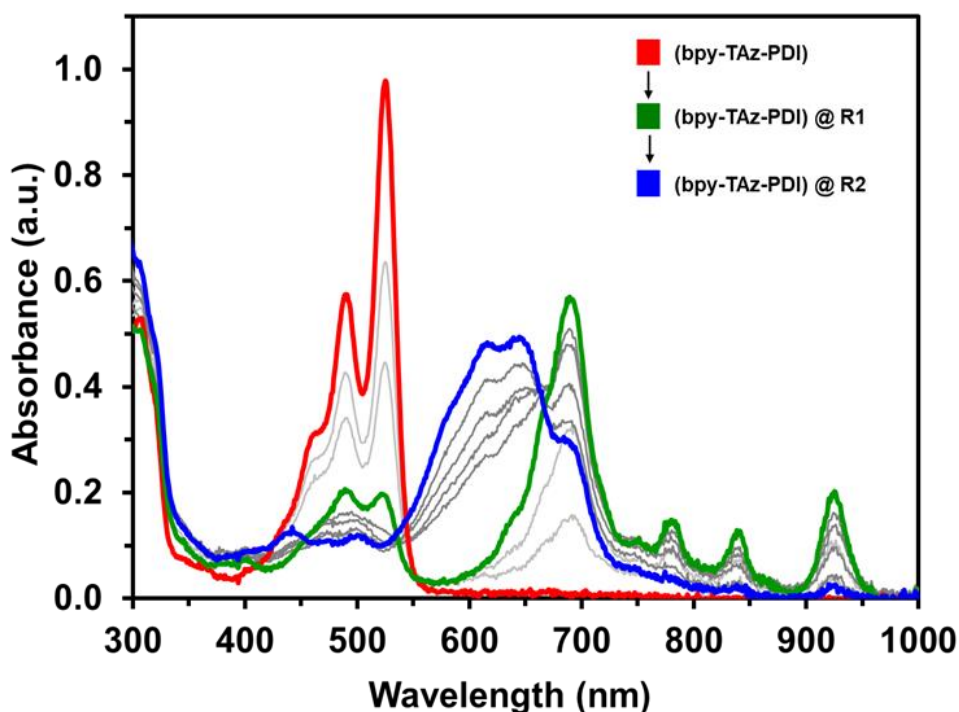


Figure S35. UV-vis-nIR spectroelectrochemical absorption profile of bpy-TAz-PDI under argon in DMF with 0.1 M TBAPF₆ electrolyte (WE = Pt-mesh, CE = Pt-wire, pseudo-RE = Ag-wire)

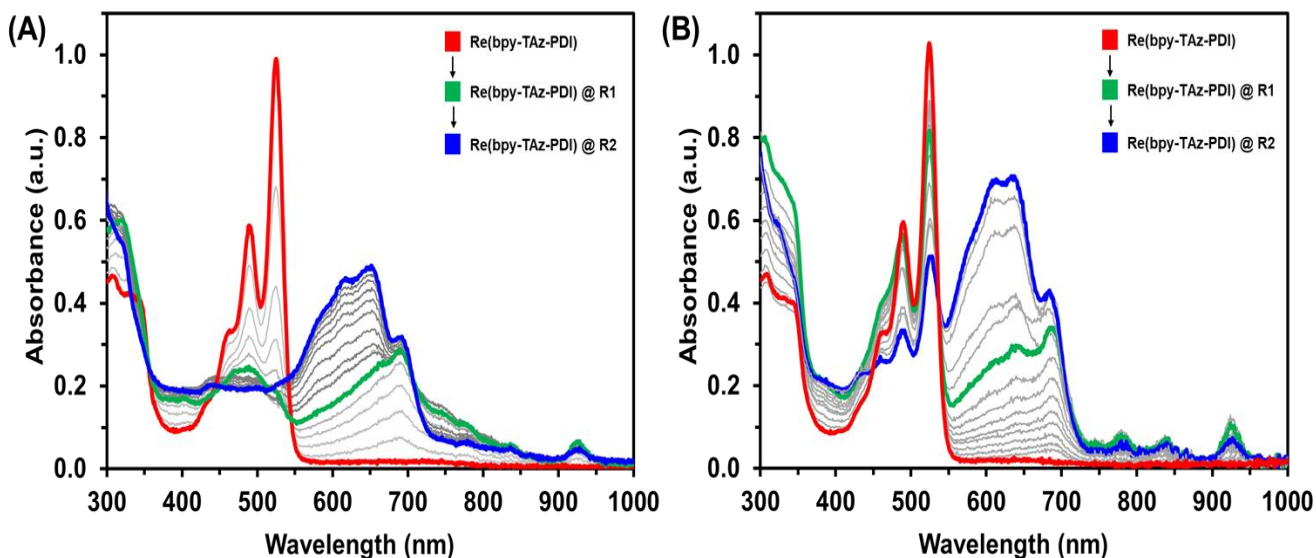
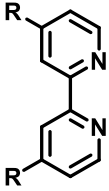
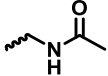
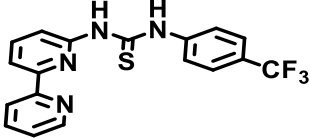
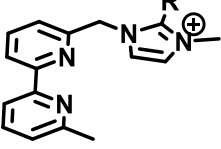
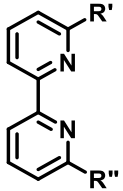
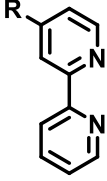
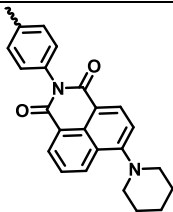
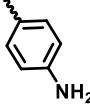
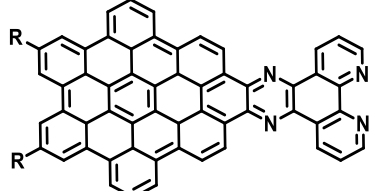


Figure S36. Comparing UV-vis-nIR spectroelectrochemical absorption profiles of Re(bpy-TAz-PDI) without TFE (A) and with TFE (B), using a constant applied potential of -1.5 V vs. Fc^{+/0}. All experiments were performed under argon, in DMF, with 0.1 M TBAPF₆ electrolyte (WE = Pt-mesh, CE = Pt-wire, pseudo-RE = Ag-wire). Spectra obtained for SEC experiments performed with TFE were complicated by the evolution of H₂ gas. It is possible that H₂ could have been evolved from either the Pt-mesh WE or Re(bpy-TAz-PDI)

7. Electro- and Photocatalytic CO₂ Reduction

Table S1. Homogeneous Re(bpy)-based catalysts for electrocatalytic CO₂ reduction.

| <i>Ligand</i> | <i>R-group</i> | <i>Applied Potential</i> (<i>V</i> vs. <i>Fc</i> ⁺⁰) | <i>FE_{co}</i> (%) | <i>Ref.</i> |
|---|---|--|----------------------------|-------------|
|  | -H | -2.09 | 98 | [16] |
| | -Me | -2.14 | ~100 | [17] |
| | - <i>t</i> Bu | -2.20 | ~100 | [17] |
| | -OCH ₃ | -2.18 | 59 | [7] |
| | -CF ₃ | -2.57 | 30 | [7] |
| | -CN | -2.31 | 18 | [7] |
|  | | -1.98 | 73 | [18] |
| | | | | |
|  | | -1.9 ^a | 89 | [19] |
|  | -H | -1.74 | 73 | [20] |
| | -Me | -1.74 | 35 | [20] |
|  | ' & " -NHMe | -2.10 | 51 | [21] |
| | ' -H; " -NHMe | -2.06 | 73 | [21] |
| | ' & " -NMe ₂ | -2.32 | 53 | [21] |
| | ' -H; " -NMe ₂ | -2.32 | 58 | [21] |
|  |  | -1.96 | 86 | [22] |
| |  | -2.0 | 96 | [23] |
|  | | -0.86 ^b | 96 | [24] |

a = (vs. Ag/AgNO₃); b = (vs. NHE)

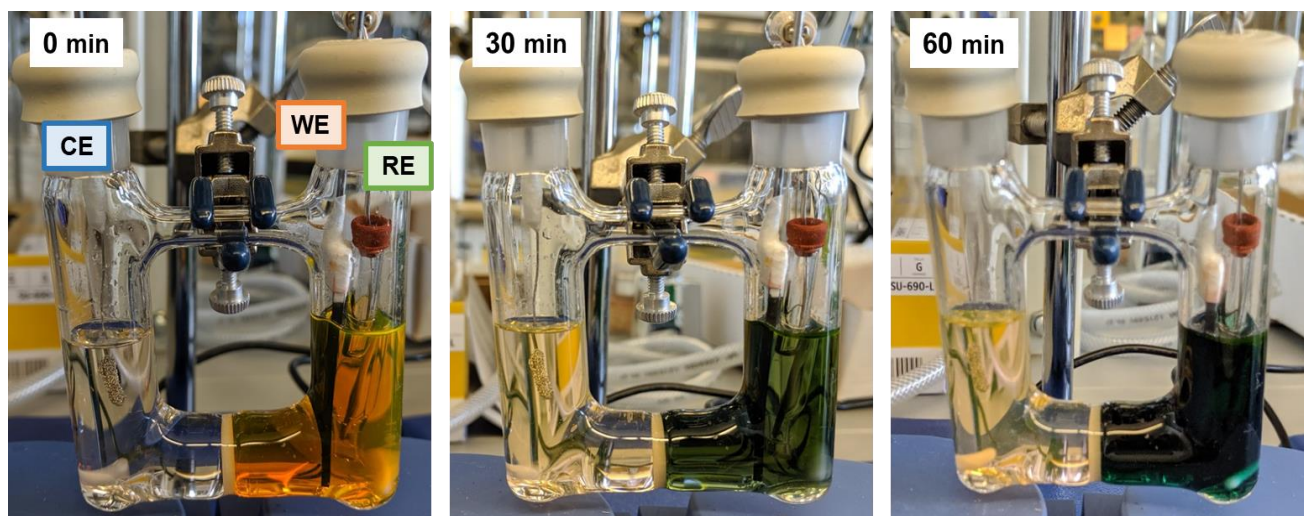


Figure S37. Representative time-lapse (left to right) of Re(bpy-TAz-PDI) CPE experiments performed in two-compartment H-shaped cell. The 3-electrode setup consisted of a glassy carbon plate working electrode (WE), a Pt-mesh counter electrode (CE), and a non-aqueous Ag/AgCl reference electrode (RE)

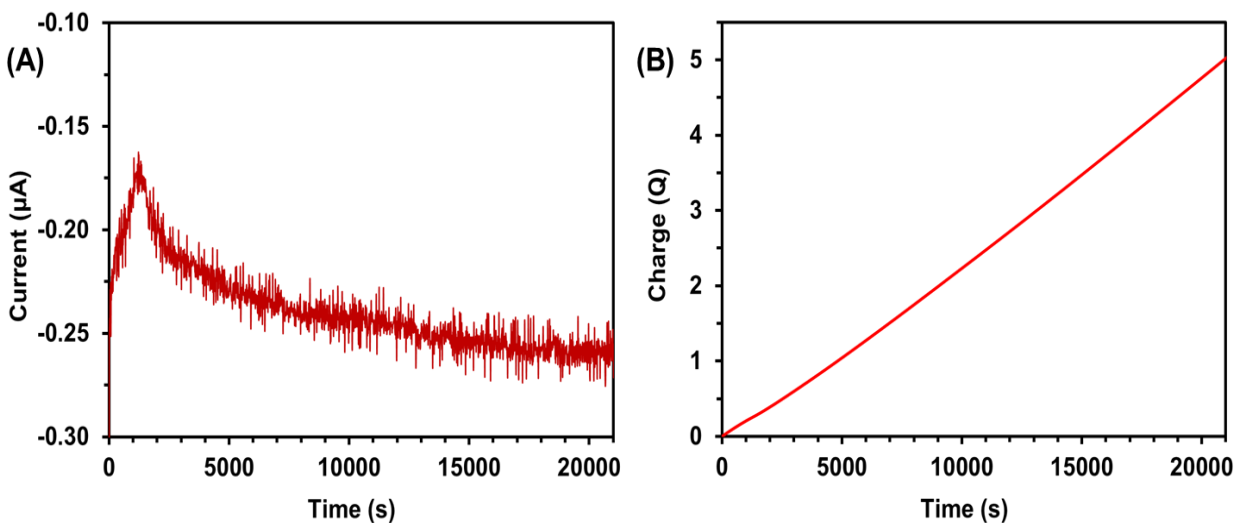


Figure S38. Representative current versus time (A) and charge passed versus time (B) plots for Re(bpy-TAz-PDI) CPE experiments performed at $E = -1.8 \text{ V}$ vs. $\text{Fc}^{+/0}$ in DMF (WE = glassy carbon plate, CE = Pt-mesh, RE = Ag/AgCl)

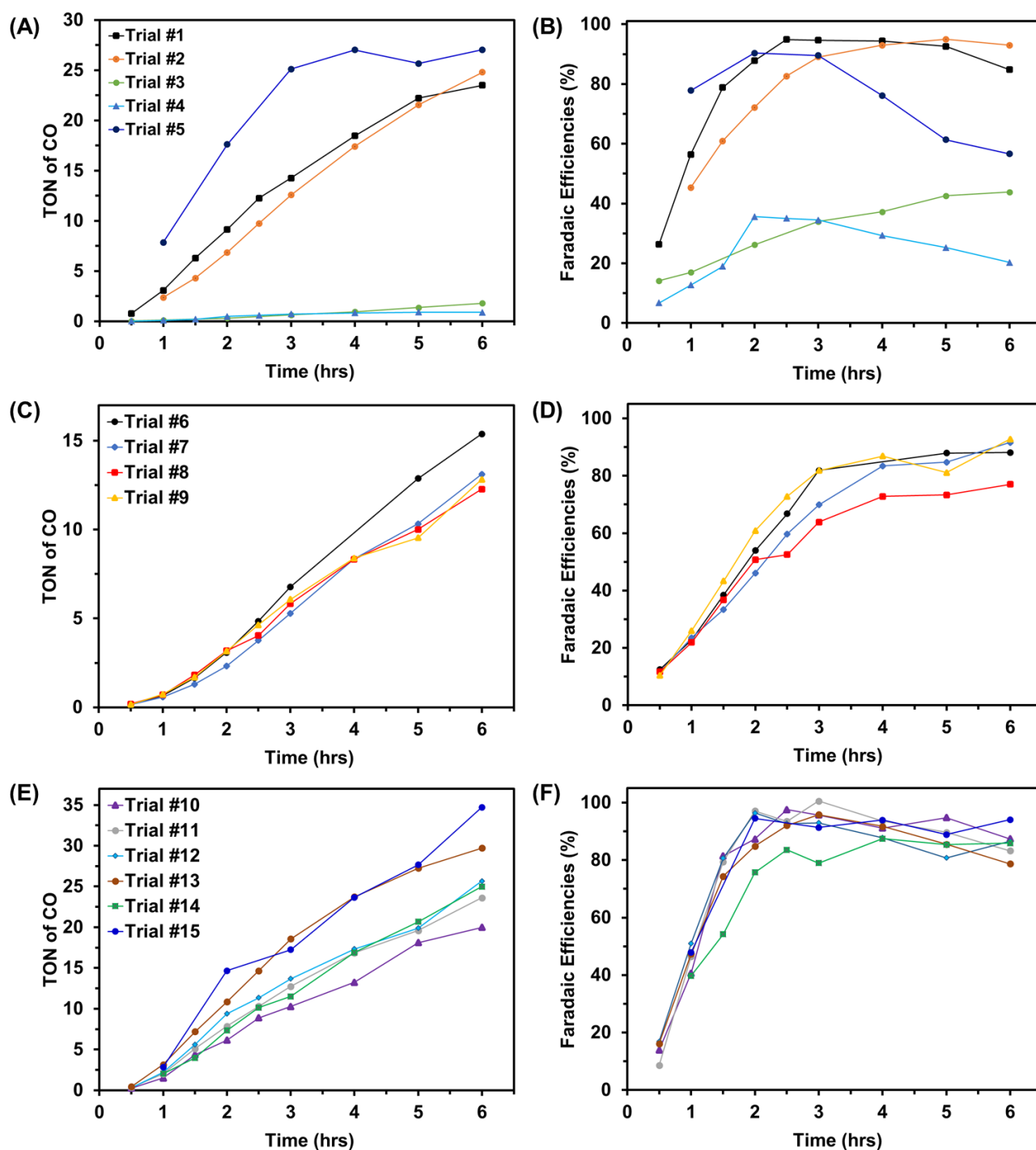


Figure S39. Controlled potential electrolysis (CPE) determined TON_{CO} and faradaic efficiencies of CO formation for Re(dmbpy) (A and B, respectively), Re(bpy-TAz-PDI) at -2.20 V vs. $Fc^{+/0}$ (C and D, respectively), and Re(bpy-TAz-PDI) at -1.80 V vs. $Fc^{+/0}$ (E and F, respectively). Full experiment details for each trail are described in Table S2

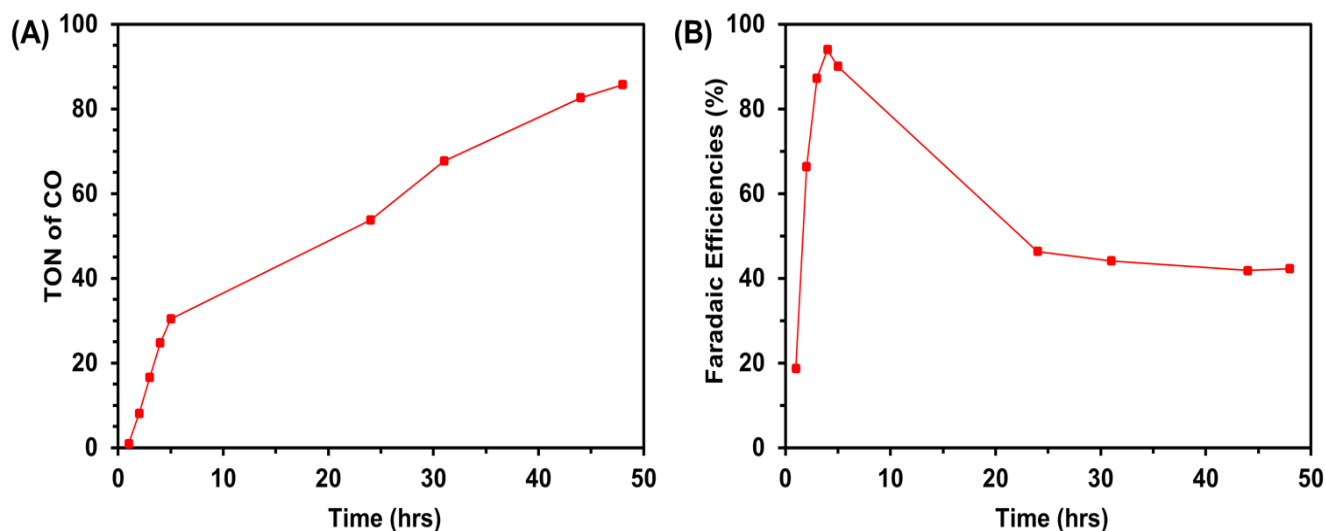


Figure S40. Prolonged controlled potential electrolysis determined TON_{co} (A) and faradaic efficiency of CO formation (B) for Re(bpy-TAz-PDI) at -1.80 V vs. Fc^{+/0}. Prolonging the CPE experiment to 24 hours resulted in a TON_{co} = 54, while the FE dropped to 47 %. Following 48 hours of CPE, the TON_{co} further increased to 86, with a stable FE of 42 %.

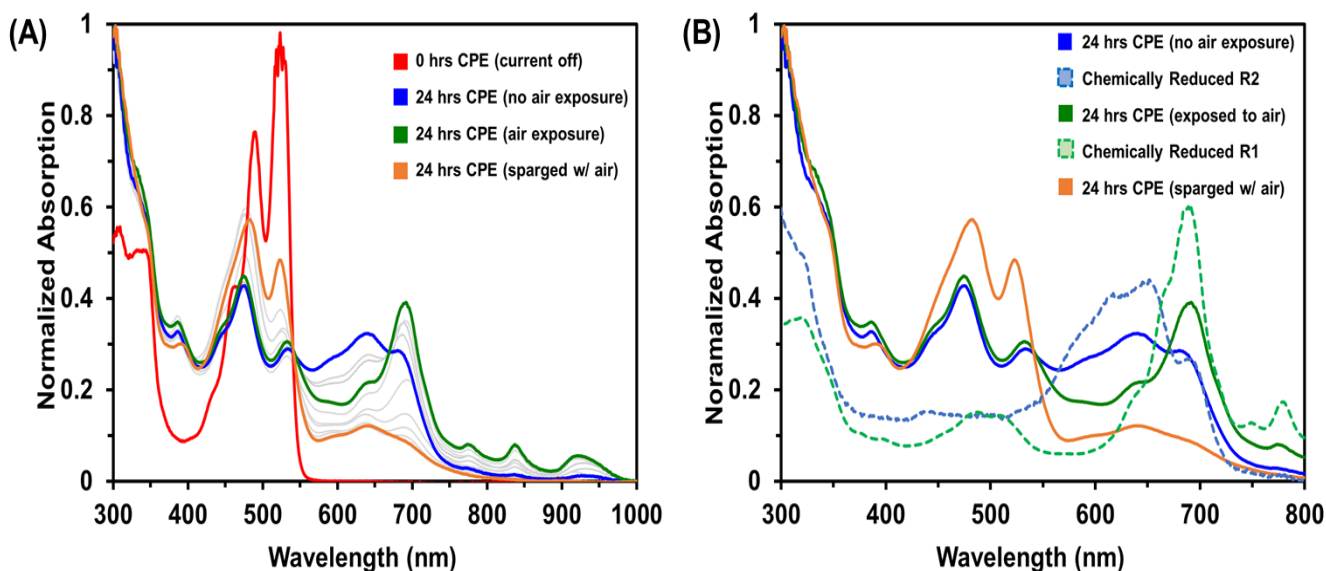


Figure S41. UV-vis-nIR absorption profiles tracking the controlled potential electrolysis of Re(bpy-TAz-PDI) at -1.80 V vs. Fc^{+/0} (A). The initial profile (red) converts to a new profile prior to exposing to air (blue). Initial exposure to air quenches dianionic PDI character in favor of monoanionic character (green), while sparging the solution with air for 1 hour affords the final profile (orange). Absorbance profiles are compared with measured UV-vis-nIR absorption profiles of singly- (dashed green) and doubly- (dashed blue) Re(bpy-TAz-PDI) (B). Final absorption profile following 24 hours of CPE (orange) does not match initial Re(bpy-TAz-PDI), likely indicating some form of PDI-related degradation.

Table S2. Replicate photocatalytic CO₂ reduction of Re(dmbpy) and Re(bpy-TAz-PDI). All experiments were completed in 0.5 mM catalyst and 0.1 M TBAPF₆ in CO₂ saturated DMF, with 2 M TFE as proton source. Product distribution was analyzed by GC. The maximum TON_{CO} was calculated based on bulk catalyst concentration and reported faradaic efficiency (FE) for CO was the maximum measured value during the 6-hour CPE experiments. Remainder of passed current led to evolution of H₂. No other gaseous products (i.e. CH₄ or C₂H₄) were detected by GC.

| <i>Entry</i> | <i>Catalyst</i> | <i>Potential</i> (V vs. Fc ^{+/0}) | <i>TON_{CO}</i> | <i>FE CO</i> (%) |
|--------------|----------------------------|--|---|--|
| 1 | Re(dmbpy) | -2.20 | 23.5 48.6 [^] | 93 61 [^] |
| 2 | Re(dmbpy) | -2.20 | 24.8 | 95 |
| | | | 24 ± 1 | 94 ± 2 |
| 3 | Re(dmbpy) | -1.80 | 1.8 | 43 |
| 4 | Re(dmbpy) | -1.80 | 0.9 | 35 |
| | | | 1.3 ± 0.8 | 39 ± 8 |
| 5 # | Re(dmbpy) | -2.20 | 27.0 | 90 |
| 6 | Re(bpy-TAz-PDI) | -2.20 | 15.4 | 88 |
| 7 | Re(bpy-TAz-PDI) | -2.20 | 13.1 33.5 [^] | 92 79 [^] |
| 8 | Re(bpy-TAz-PDI) | -2.20 | 12.3 | 77 |
| 9 | Re(bpy-TAz-PDI) | -2.20 | 12.8 | 93 |
| | | | 13 ± 1 | 87 ± 10 |
| 10 | Re(bpy-TAz-PDI) | -1.80 | 20.0 | 95 |
| 11 | Re(bpy-TAz-PDI) | -1.80 | 23.6 53.8 [^] 86.2 ^{^^} | 101 47 [^] 42 ^{^^} |
| 12 | Re(bpy-TAz-PDI) | -1.80 | 25.7 | 93 |
| 13 | Re(bpy-TAz-PDI) | -1.80 | 29.7 | 88 |
| 14 * | Re(bpy-TAz-PDI) | -1.80 | 24.9 | 87 |
| | | | 24 ± 4 | 92 ± 7 |
| 15 # | Re(bpy-TAz-PDI) | -1.80 | 34.7 | 95 |
| 16 † | Re(bpy-TAz-PDI) | -1.80 | 0 | 0 |
| 17 ‡ | Re(bpy-TAz-PDI) | -1.80 | 0 | 0 |
| 18 | none | -1.80 | 0 | 0 |
| 19 | Re(dmbpy) & bpy-TAz-PDI | -1.80 | 1.3 | 32 |

[^] = measured after 24 hrs of electrocatalysis; # = electrolysis performed in presence of Thor Labs blue LED;

* = performed in the dark; † = control experiment under argon; ‡ = control experiment under CO₂ with no TFE added;

Table S3. Replicate controlled potential electrolyses of Re(dmbpy) and Re(bpy-TAz-PDI). All experiments were completed in septum-sealed glass pressure vials using 65 μ M catalyst. The maximum TON_{CO} and TON_{H₂} were calculated based on bulk catalyst concentration. Product distribution was analyzed by GC. No other gaseous products (i.e. CH₄, C₂H₄, or C₂H₆) were detected by GC.

| Entry | Catalyst | Solvent (DMF:TEOA:TFE) | Time (hrs) | TON _{CO} | TON _{H₂} |
|-----------|-----------------|---------------------------|---------------|---------------------------------|------------------------------|
| 1a | Re(dmbpy) | 5 : 1 : 0 | 2 | 0.9 | 0.0 |
| 1b | Re(dmbpy) | 5 : 1 : 0 | 4 | 1.5 | 0.0 |
| 1c | Re(dmbpy) | 5 : 1 : 0 | 6 | 1.7 | 0.0 |
| 1d | Re(dmbpy) | 5 : 1 : 0 | 18 | 2.1 | 0.0 |
| 2 | Re(dmbpy) | 5 : 1 : 0 | 18 | 1.8 | 0.0 |
| 3 | Re(dmbpy) | 5 : 1 : 0 | 18 | 1.7 | 0.0 |
| | | | | 1.9 \pm 0.2 | 0 |
| 4 | Re(dmbpy) | 4 : 1 : 1 | 18 | 0.0 | 0.0 |
| 5 | Re(dmbpy) | 4 : 1 : 1 | 18 | 0.0 | 0.0 |
| 6 | Re(dmbpy) | 4 : 1 : 1 | 18 | 0.0 | 0.0 |
| 7a | Re(bpy-TAz-PDI) | 5 : 1 : 0 | 2 | 0.2 | 0.0 |
| 7b | Re(bpy-TAz-PDI) | 5 : 1 : 0 | 4 | 1.5 | 0.0 |
| 7c | Re(bpy-TAz-PDI) | 5 : 1 : 0 | 6 | 2.2 | 0.0 |
| 7d | Re(bpy-TAz-PDI) | 5 : 1 : 0 | 18 | 8.7 | 1.0 |
| 8 | Re(bpy-TAz-PDI) | 5 : 1 : 0 | 18 | 7.4 | 0.6 |
| 9 | Re(bpy-TAz-PDI) | 5 : 1 : 0 | 18 | 9.1 | 0.0 |
| | | | | 8.4 \pm 0.9 | 0.5 |
| 10 | Re(bpy-TAz-PDI) | 4 : 1 : 1 | 18 | 4.3 | 0.0 |
| 11 | Re(bpy-TAz-PDI) | 4 : 1 : 1 | 18 | 5.6 | 0.2 |
| 12 | Re(bpy-TAz-PDI) | 4 : 1 : 1 | 18 | 3.9 | 0.0 |
| | | | | 4.6 \pm 0.9 | 0.1 |

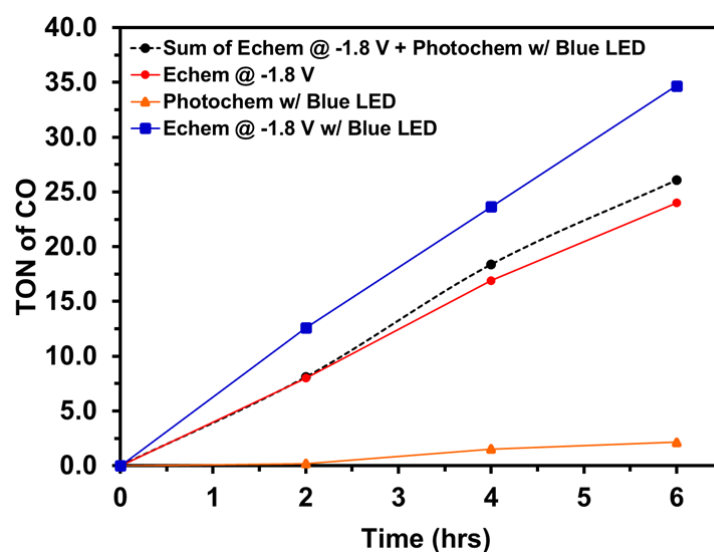


Figure S42. Comparing individual photo- and electrocatalytic CO₂ reductions of Re(bpy-TAz-PDI) relative to the electrocatalysis of Re(bpy-TAz-PDI) performed in presence of blue light.

8. Density Functional Theory Calculations

Density functional theory (DFT) calculations were carried with the Gaussian16 (Revision A.03)²⁵ software suite. The M06 functional was used for all calculations as it was developed for use with both transition metals and non-metals.²⁶ The 6-31G(d,p) Pople basis set^{27–29} was used for all non-metal elements, and the LANL2DZ basis set^{30–32} was used for Re, with 60 core electrons subsumed into the effective core potentials. For all optimized geometries, normal mode analyses were carried out to ensure that no negative frequencies were present. To reduce computational cost, all terminal N-alkyl groups were truncated to methyl groups. For highly charged species, full convergence was first obtained by using the loose criteria for convergence, followed by the tighter, default grid. In addition, the NoSymm tag was used for initial convergence of the -3 charged species and then removed to attain full convergence. Molecular orbitals and spin densities were visualized using GaussView 5.0.9.³³

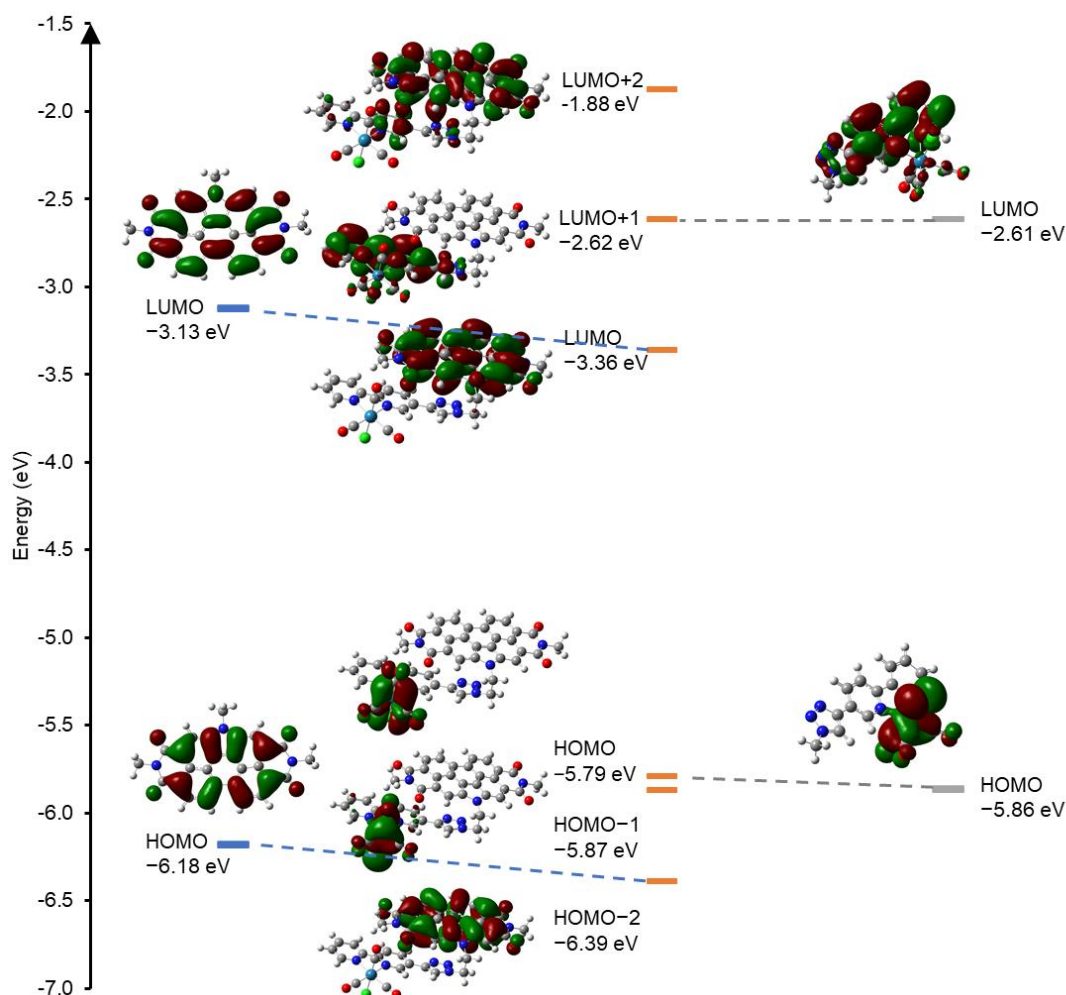


Figure S43. Molecular orbital diagram of Re(bpy-TAz-PDI) (center), comprised of N-annulated PDI (left) and Re(bpy-TAz) (right) as determined at the M06/6-31G(d,p)/LANL2DZ level of theory.

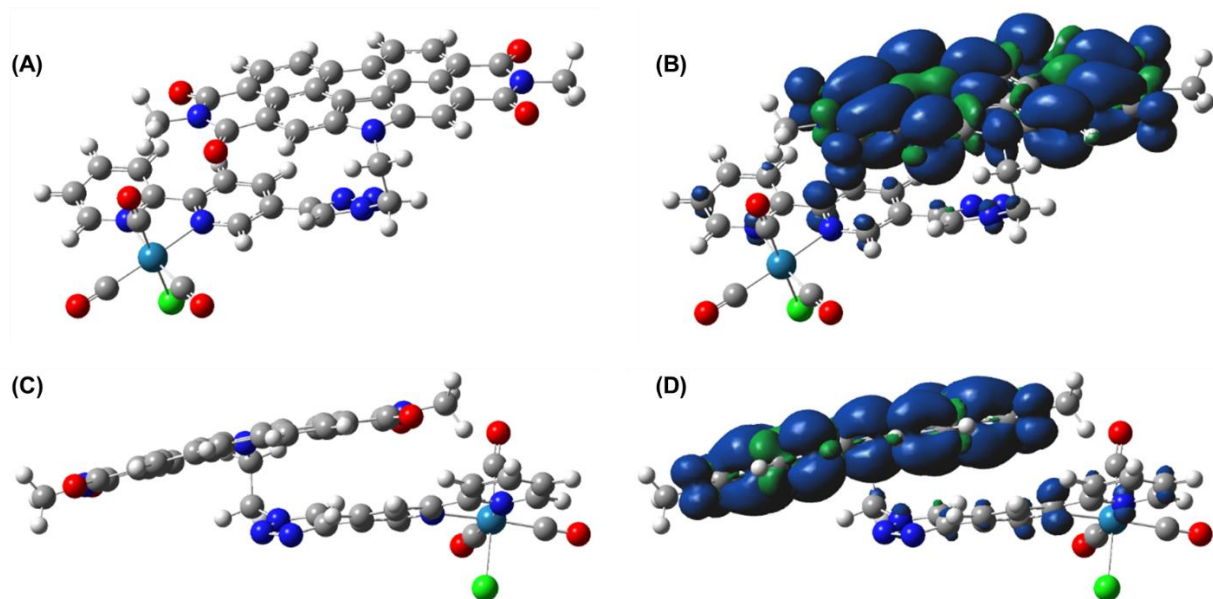


Figure S44. Face-on and side-on perspectives of the optimized geometry (A & C) and spin density map (B & D) for the doublet state of $\text{Re}^{\text{I}}(\text{bpy-TAz-PDI})^-$ as determined at the M06/6-31G(d,p)/LANL2DZ level of theory.

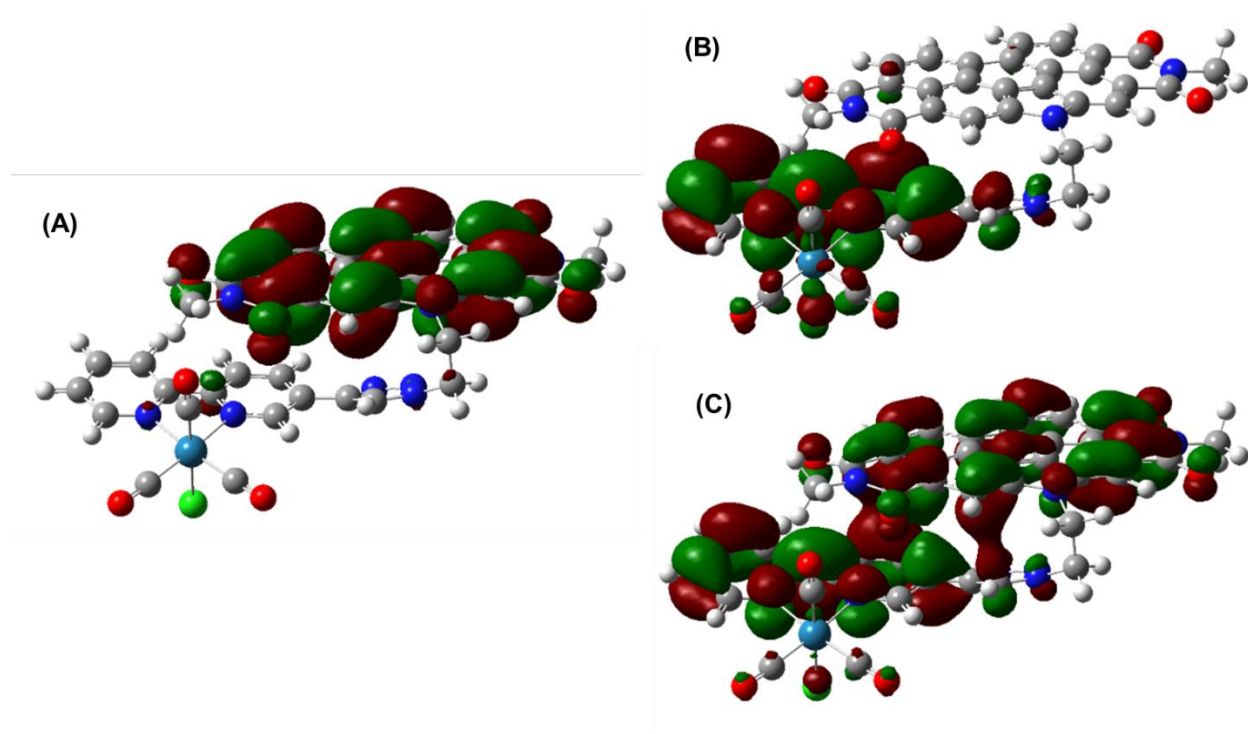


Figure S45. Frontier molecular orbitals of the doublet state of $\text{Re}^{\text{I}}(\text{bpy-TAz-PDI})^-$ at the M06/6-31G(d,p)/LANL2DZ level of theory, where (A) represents HOMO and (B & C) represent the LUMO with α - and β -spins, respectively.

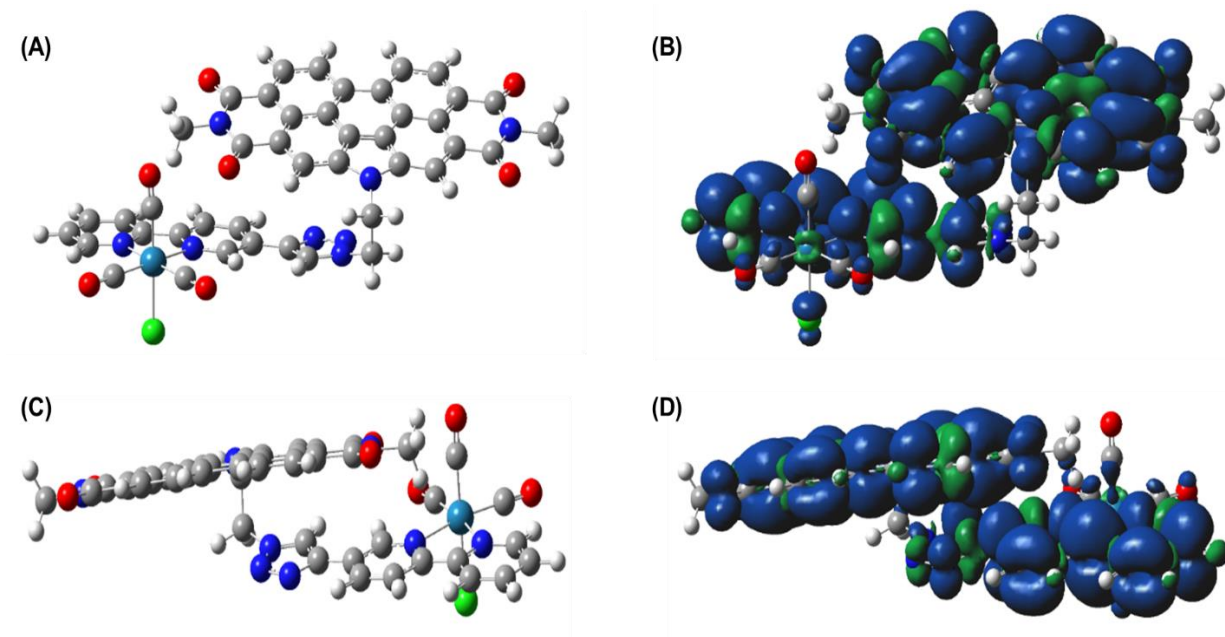


Figure S46. Face-on and side-on perspectives of the optimized geometry (A & C) and spin density map (B & D) for the triplet state of $\text{Re}^{\text{I}}(\text{bpy-TAz-PDI})^{2-}$ as determined at the M06/6-31G(d,p)/LANL2DZ level of theory.

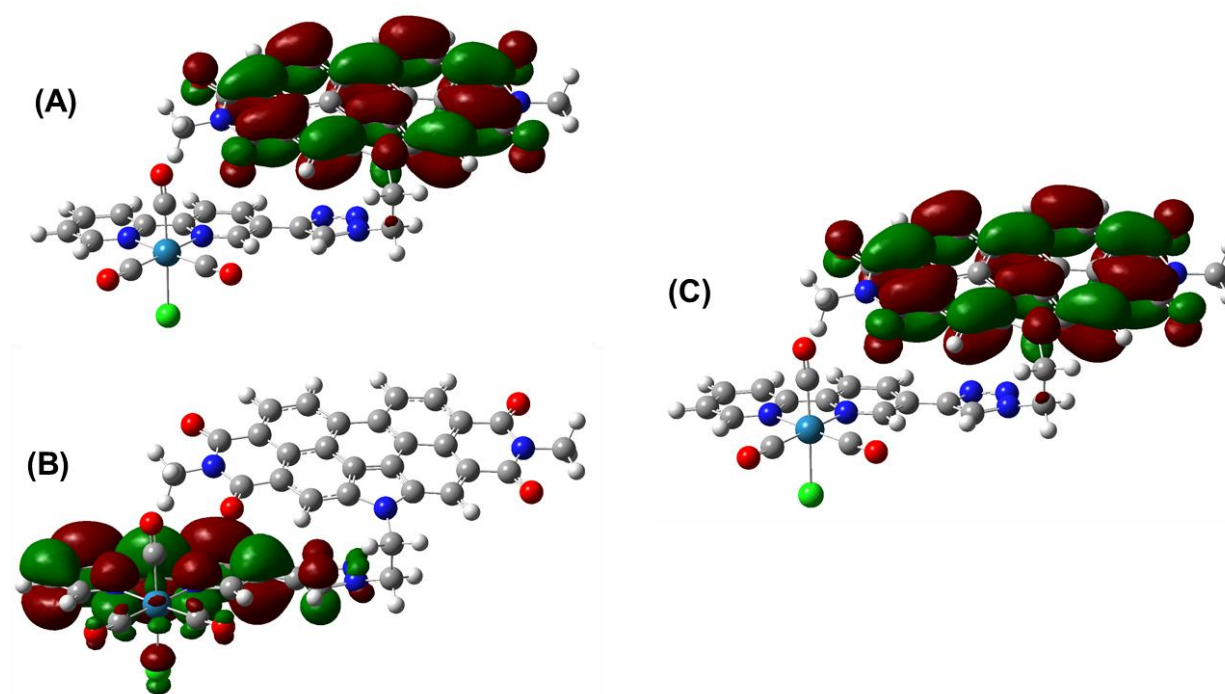


Figure S47. Frontier molecular orbitals of the triplet state of $\text{Re}^{\text{I}}(\text{bpy-TAz-PDI})^{2-}$ at the M06/6-31G(d,p)/LANL2DZ level of theory, where (A & B) represent the HOMO-1 and HOMO with α -spins, respectively, and (C) is the LUMO with β -spin.

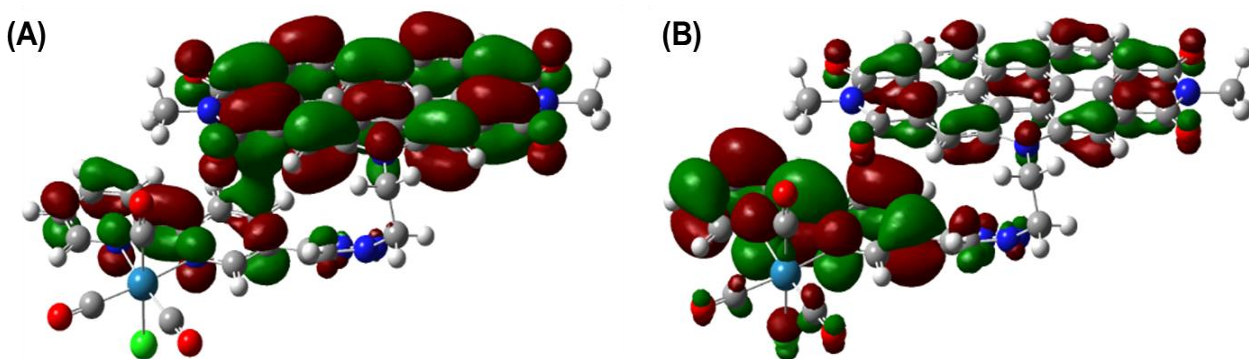


Figure S48. Frontier molecular orbitals of the singlet state of $\text{Re}^{\text{I}}(\text{bpy-TAz-PDI})_2^-$ at the M06/6-31G(d,p)/LANL2DZ level of theory, where (A) represents the HOMO and (B) is the LUMO.

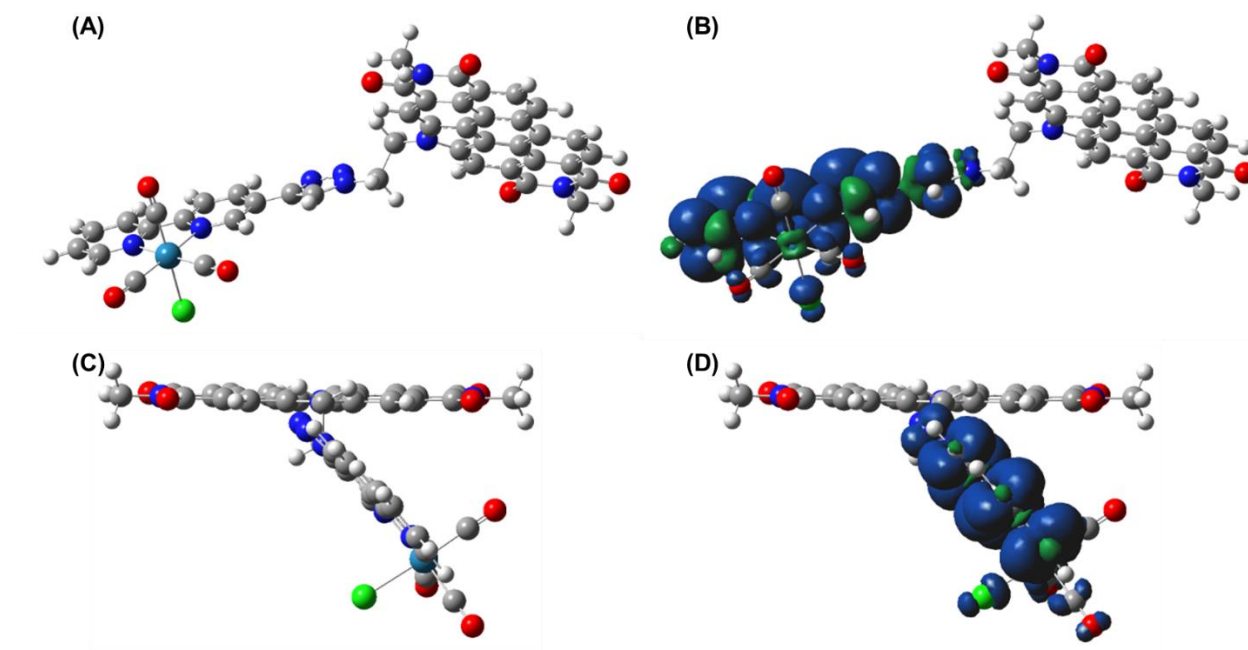


Figure S49. Face-on and side-on perspectives of the optimized geometry (A & C) and spin density map (B & D) for the doublet state of $\text{Re}^{\text{I}}(\text{bpy-TAz-PDI})_3^-$ as determined at the M06/6-31G(d,p)/LANL2DZ level of theory.

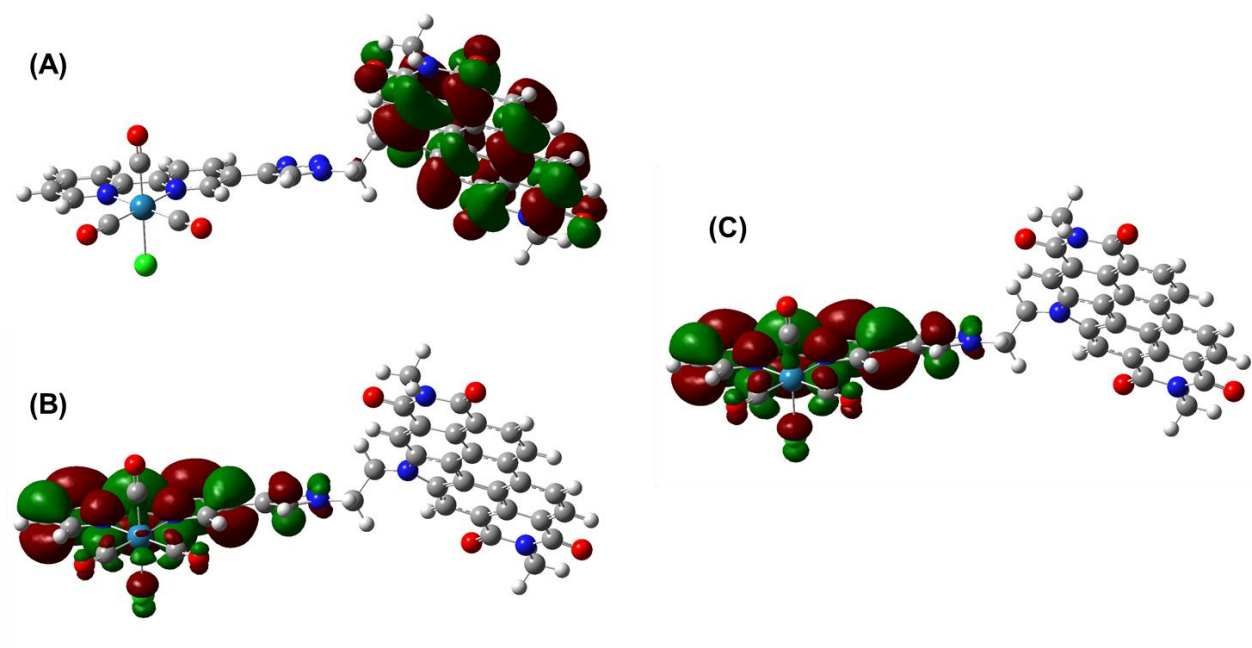


Figure S50. Frontier molecular orbitals of the doublet state of $\text{Re}^{\text{I}}(\text{bpy-TAz-PDI})^{3-}$ at the M06/6-31G(d,p)/LANL2DZ level of theory, where (A) represents the HOMO with electrons paired on PDI, while (B & C) represent the $\text{HO}\alpha\text{O}$ and $\text{LU}\beta\text{O}$ with α - and β -spins, respectively.

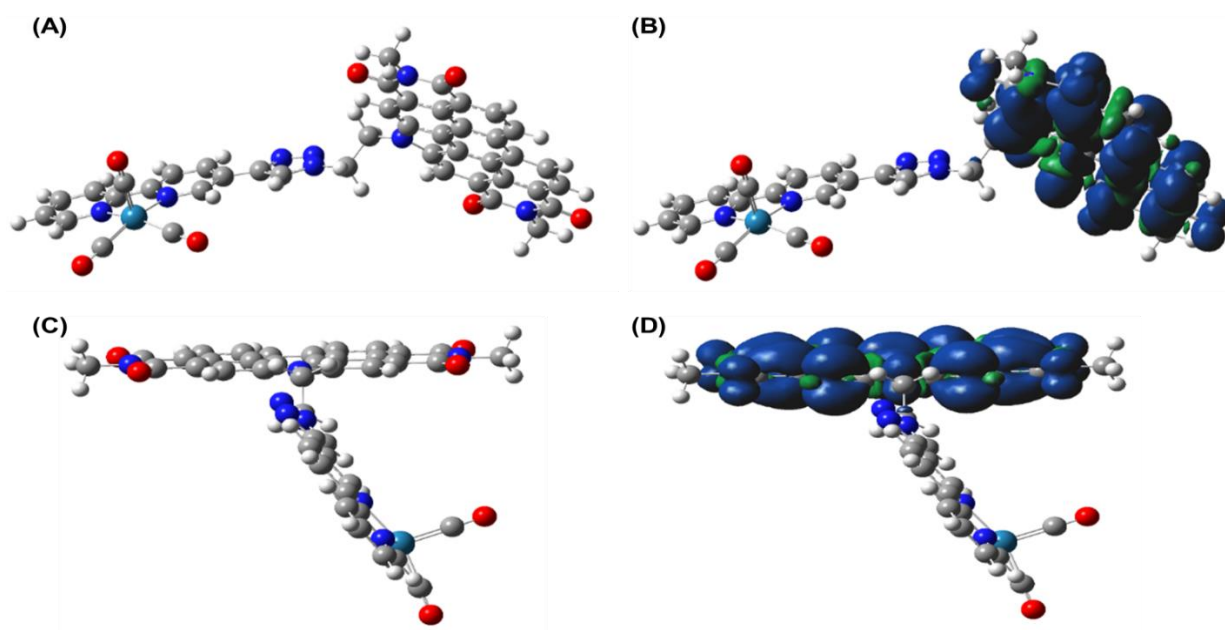


Figure S51. Face-on and side-on perspectives of the optimized geometry (A & C) and spin density map (B & D) for the doublet state of $\text{Re}^0(\text{bpy-TAz-PDI})^{2-}$ as determined at the M06/6-31G(d,p)/LANL2DZ level of theory.

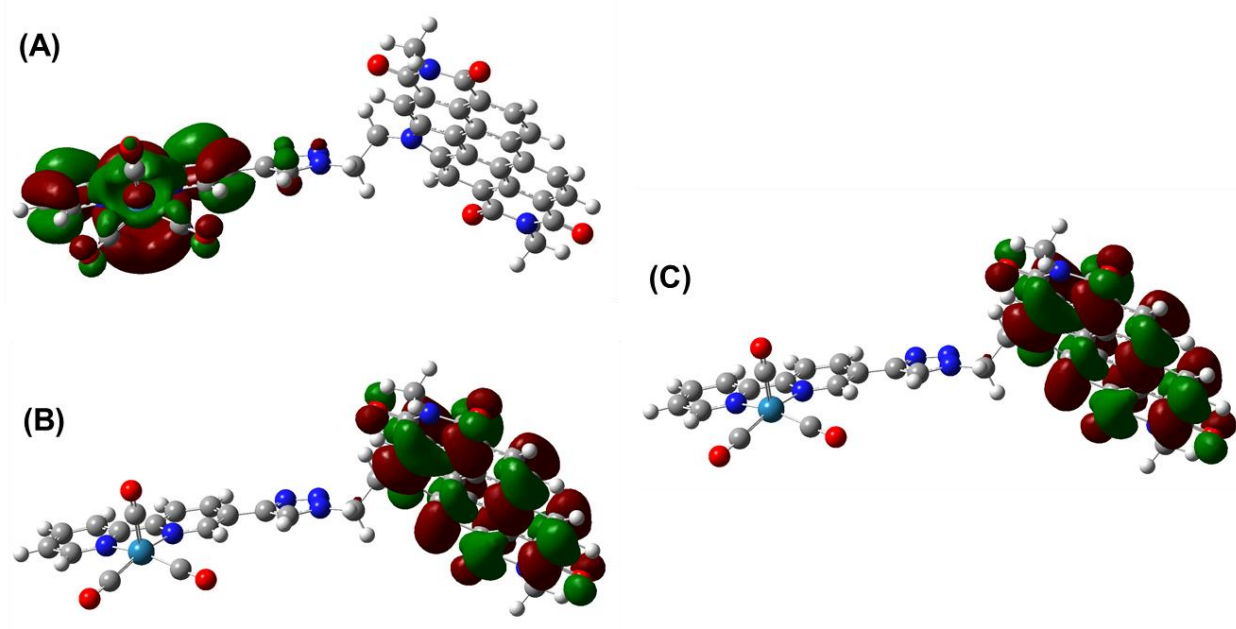


Figure S52. Frontier molecular orbitals of the doublet state of $\text{Re}^0(\text{bpy-TAz-PDI})^{2-}$ at the M06/6-31G(d,p)/LANL2DZ level of theory, where (A) represents the HOMO with paired electrons on $\text{Re}(\text{bpy})$, and (B & C) are the $\text{HO}\alpha\text{O}$ and $\text{LU}\beta\text{O}$ with α - and β -spins, respectively.

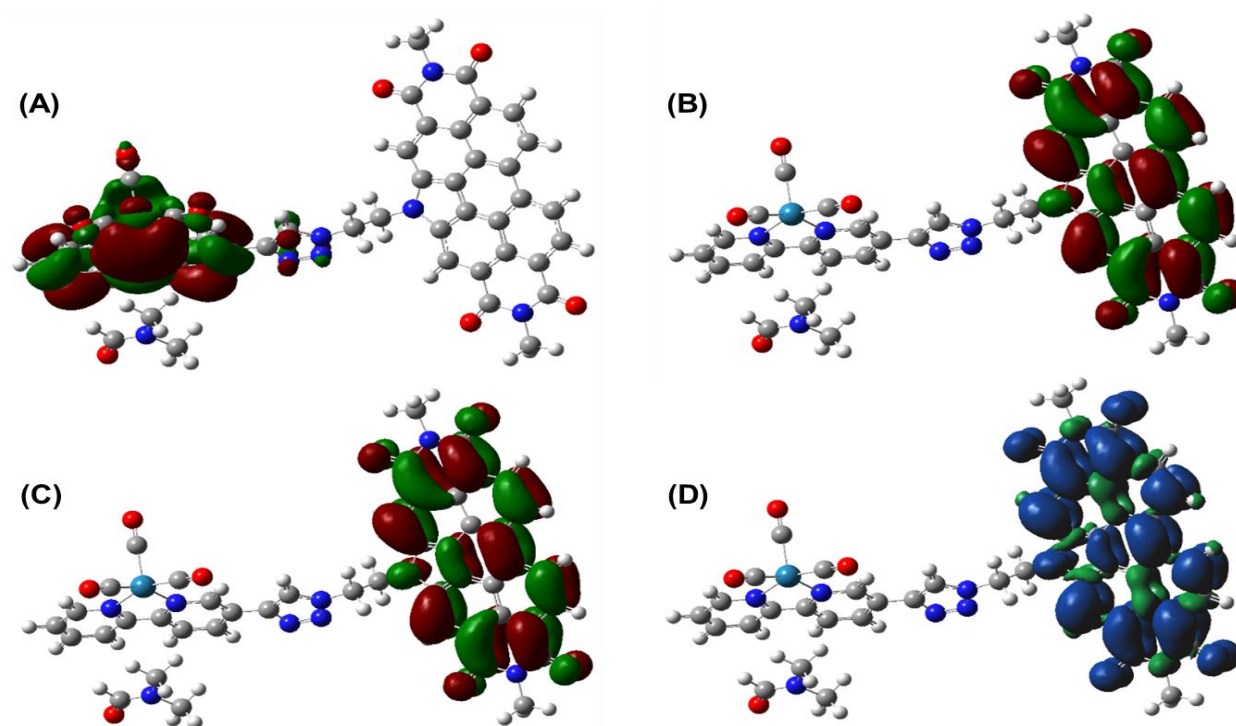


Figure S53. Frontier molecular orbitals and spin density mapping at the M06/6-31G(d,p)/LANL2DZ level of theory for the doublet state of $\text{Re}^0(\text{bpy-TAz-PDI})^{2-}$ stabilized by an explicit molecule of DMF, where (A) represents the HOMO with paired electrons on $\text{Re}(\text{bpy})$, and (B & C) are the $\text{HO}\alpha\text{O}$ and $\text{LU}\beta\text{O}$ with α - and β -spins, respectively, and (D) is the spin density map.

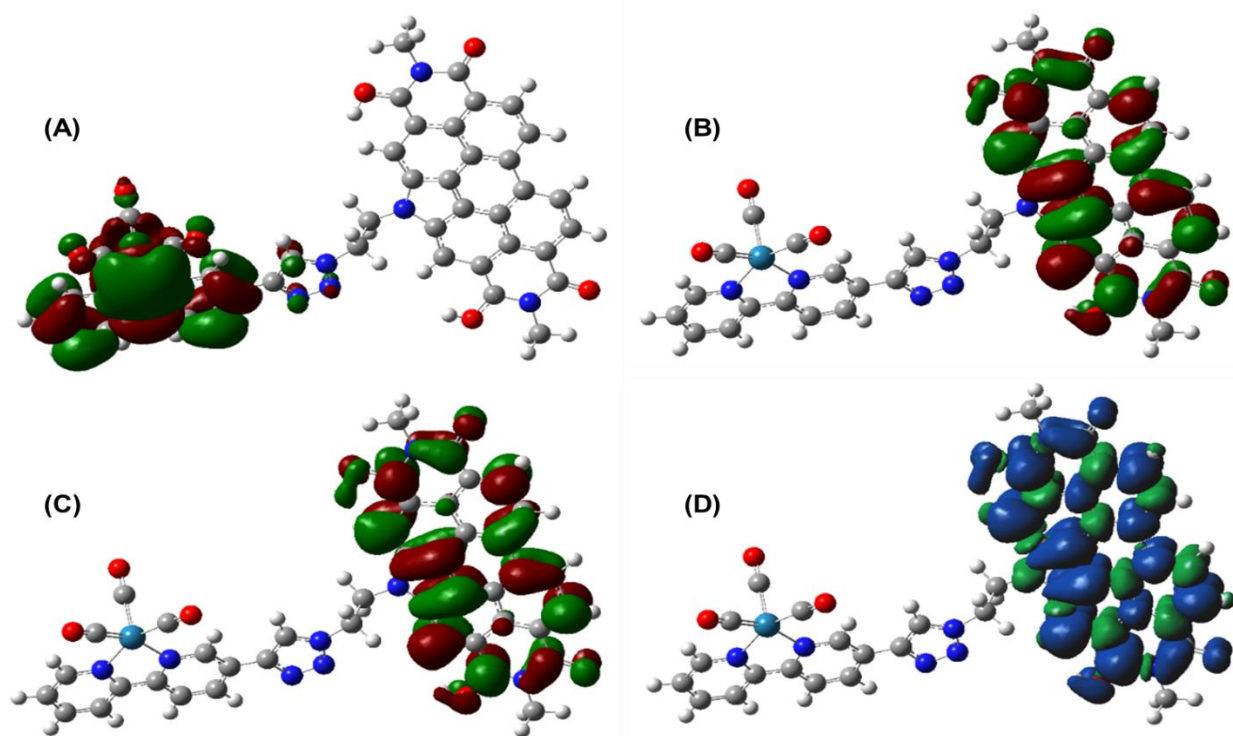


Figure S54. Frontier molecular orbitals and spin density mapping at the M06/6-31G(d,p)/LANL2DZ level of theory for the doublet state of $\text{Re}^0(\text{bpy-TAz-PDI})^{2-}$ stabilized by explicit protonation of PDI imide oxygens, where (A) represents the HOMO with paired electrons on $\text{Re}(\text{bpy})$, and (B & C) are the HO α O and LU β O with α - and β -spins, respectively, and (D) is the spin density map.

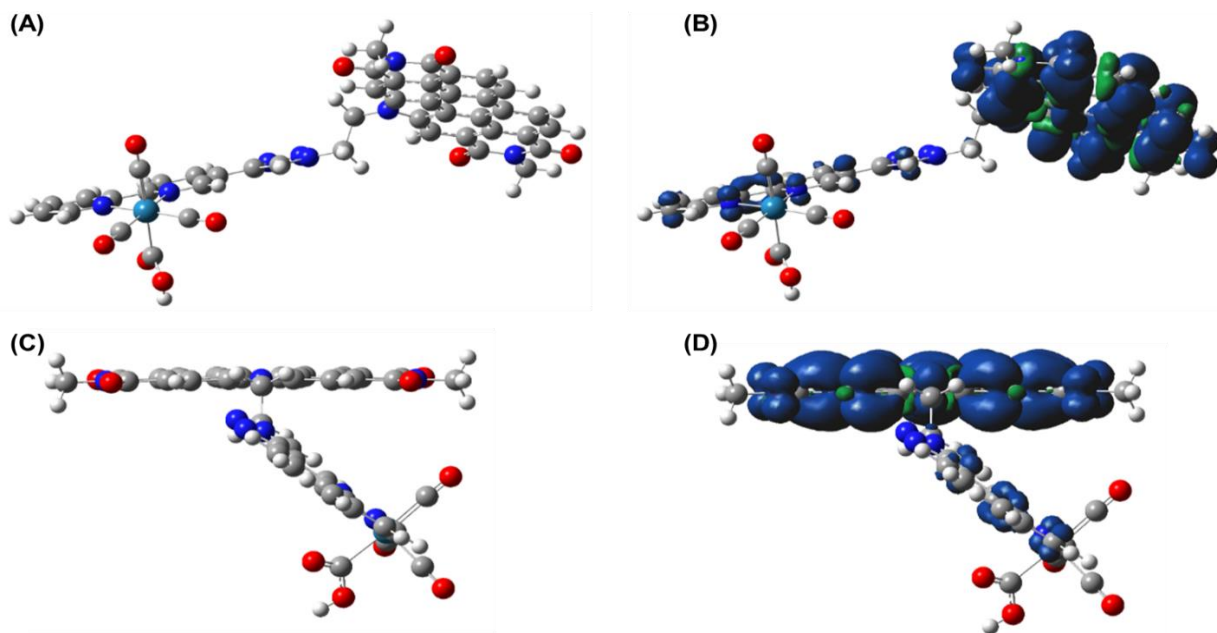


Figure S55. Face-on and side-on perspectives of the optimized geometry (A & C) and spin density map (B & D) for the doublet state of $\text{Re}^I[(\text{COOH})(\text{bpy-TAz-PDI})]^-$ as determined at the M06/6-31G(d,p)/LANL2DZ level of theory.

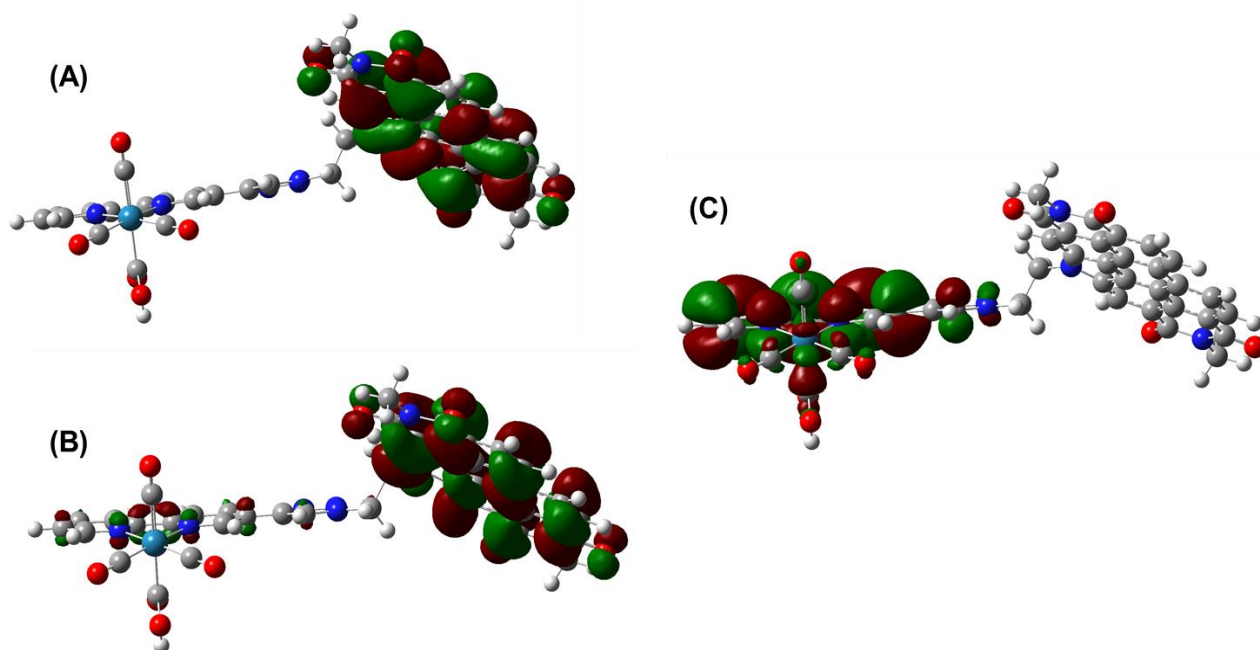


Figure S56. Frontier molecular orbitals of the doublet state of $\text{Re}^{\text{I}}[(\text{COOH})(\text{bpy-TAz-PDI})]^-$ at the M06/6-31G(d,p)/LANL2DZ level of theory, where (A) represents the HOMO, and (B & C) are the $\text{HO}\alpha\text{O}$ and $\text{LU}\beta\text{O}$ with α - and β -spins, respectively.

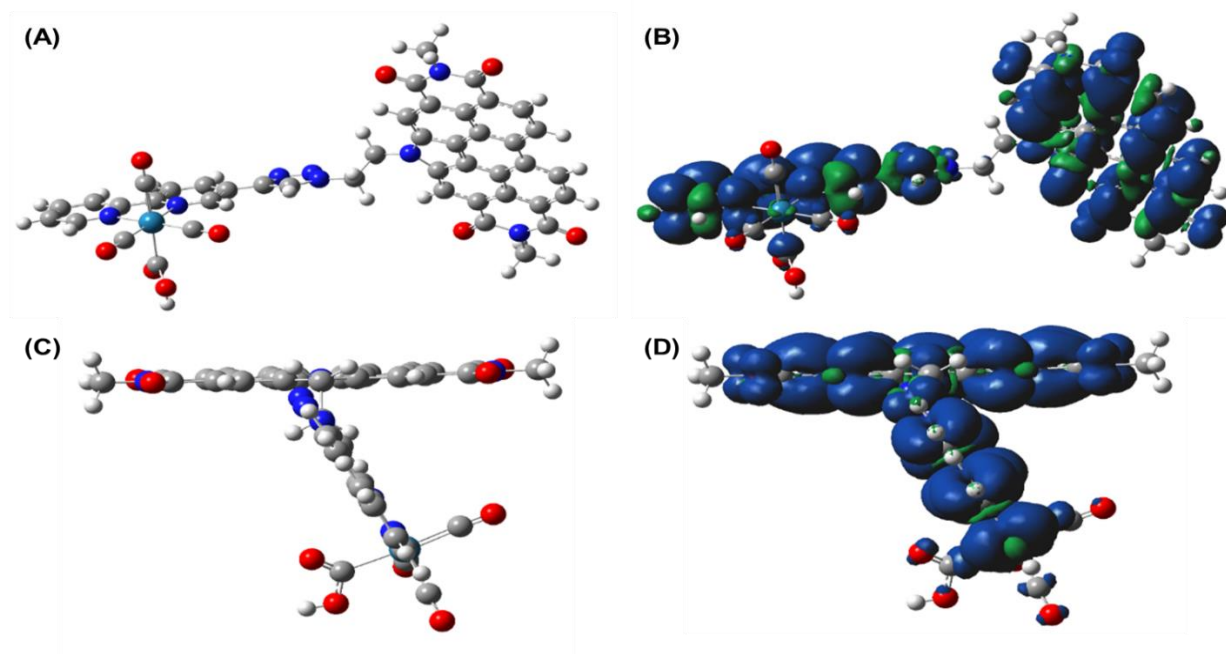


Figure S57. Face-on and side-on perspectives of the optimized geometry (A & C) and spin density map (B & D) for the triplet state of $\text{Re}^{\text{I}}[(\text{COOH})(\text{bpy-TAz-PDI})]^{2-}$ as determined at the M06/6-31G(d,p)/LANL2DZ level of theory.

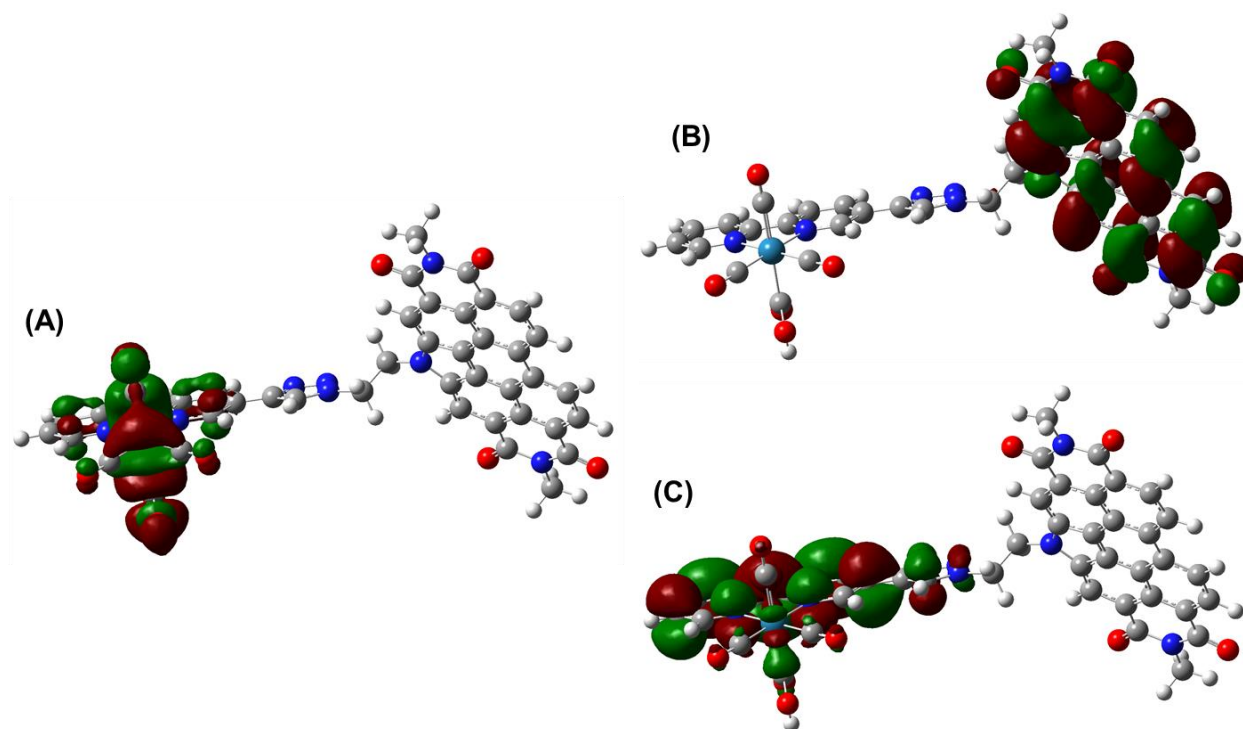


Figure S58. Frontier molecular orbitals of the triplet state of $\text{Re}^{\text{I}}[(\text{COOH})(\text{bpy-TAz-PDI})]^{2-}$ at the M06/6-31G(d,p)/LANL2DZ level of theory, where (A) represents the HOMO, and (B & C) are the $\text{HO}\alpha\text{O}-1$ and $\text{HO}\alpha\text{O}$ with α -electrons, respectively.

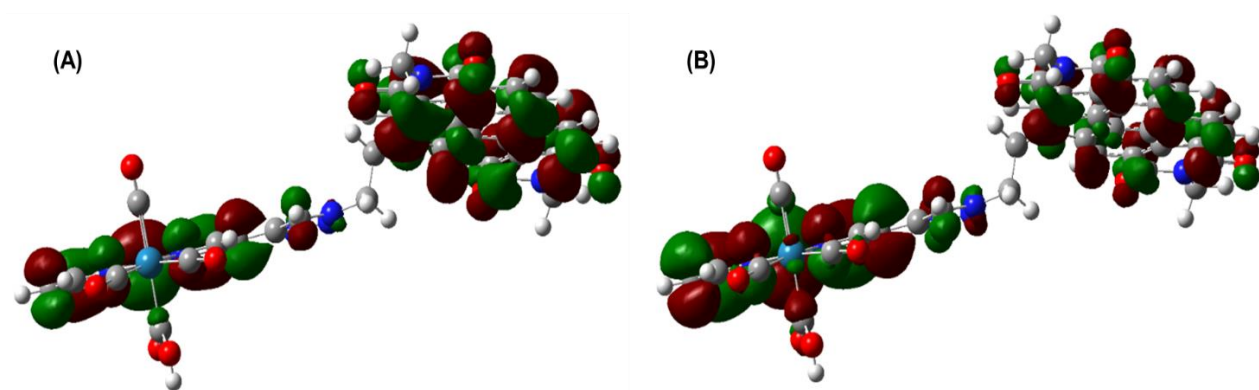


Figure S59. Frontier molecular orbitals of the singlet state of $\text{Re}^{\text{I}}[(\text{COOH})(\text{bpy-TAz-PDI})]^{2-}$ at the M06/6-31G(d,p)/LANL2DZ level of theory, where (A) is the HOMO and (B) is the LUMO.

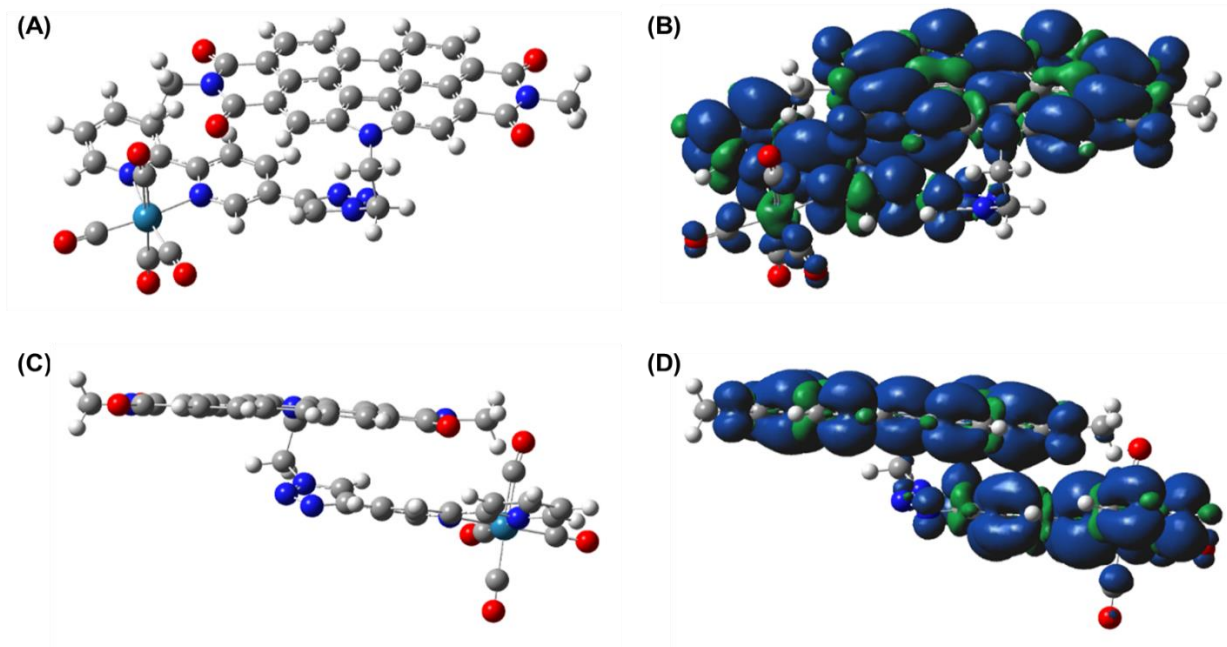


Figure S60. Face-on and side-on perspectives of the optimized geometry (A & C) and spin density map (B & D) for the triplet state of $\text{Re}^{\text{I}}[(\text{CO})_4(\text{bpy-TAz-PDI})]^-$ as determined at the M06/6-31G(d,p)/LANL2DZ level of theory.

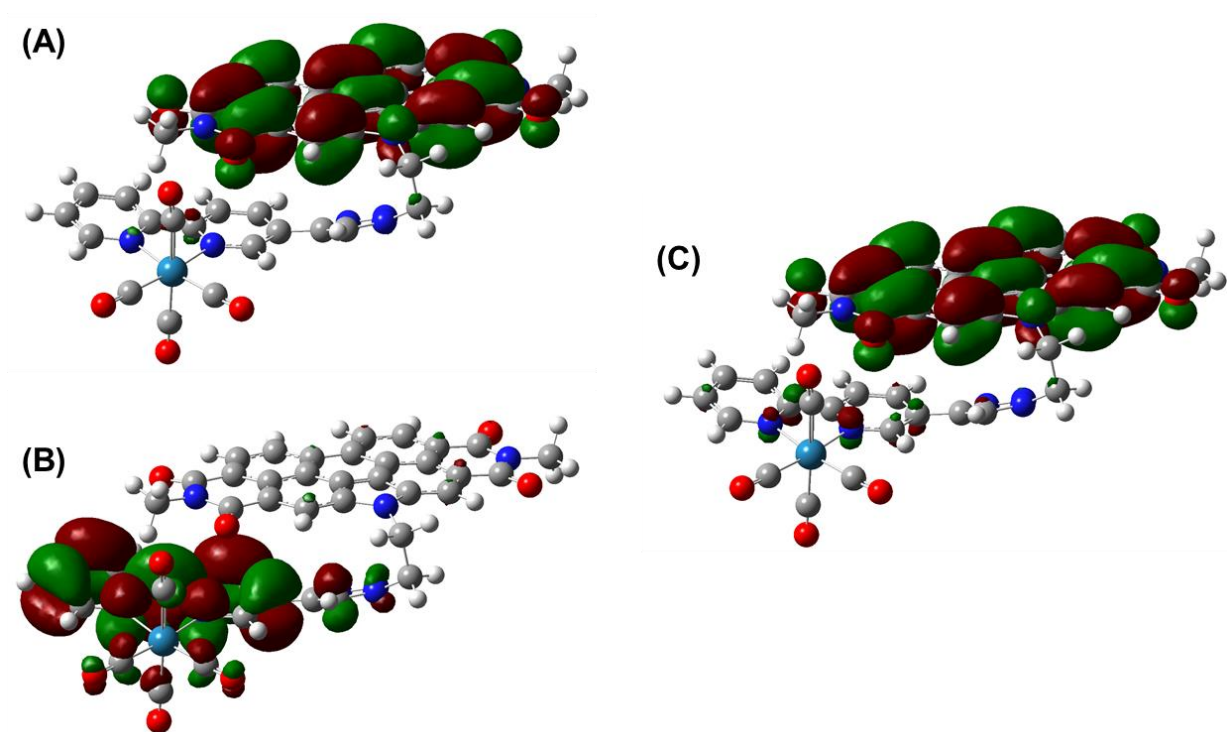


Figure S61. Frontier molecular orbitals of the triplet state of $\text{Re}^{\text{I}}[(\text{CO})_4(\text{bpy-TAz-PDI})]^-$ at the M06/6-31G(d,p)/LANL2DZ level of theory, where (A & B) represent the $\text{HO}\alpha\text{O}-1$ and $\text{HO}\alpha\text{O}$ with α -electrons, and (C) is the $\text{LU}\beta\text{O}$ with β -spin.

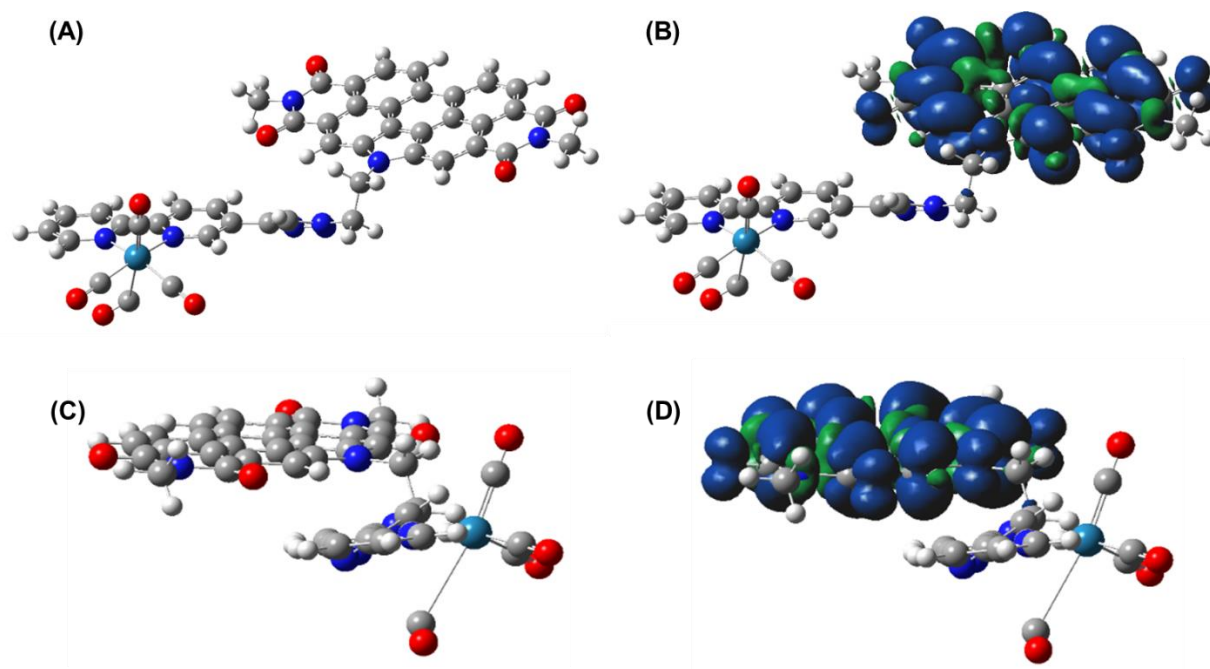


Figure S62. Face-on and side-on perspectives of the optimized geometry (A & C) and spin density map (B & D) for the doublet state of $\text{Re}^{\text{I}}[(\text{CO})_4(\text{bpy-TAz-PDI})]^{2-}$ as determined at the M06/6-31G(d,p)/LANL2DZ level of theory.

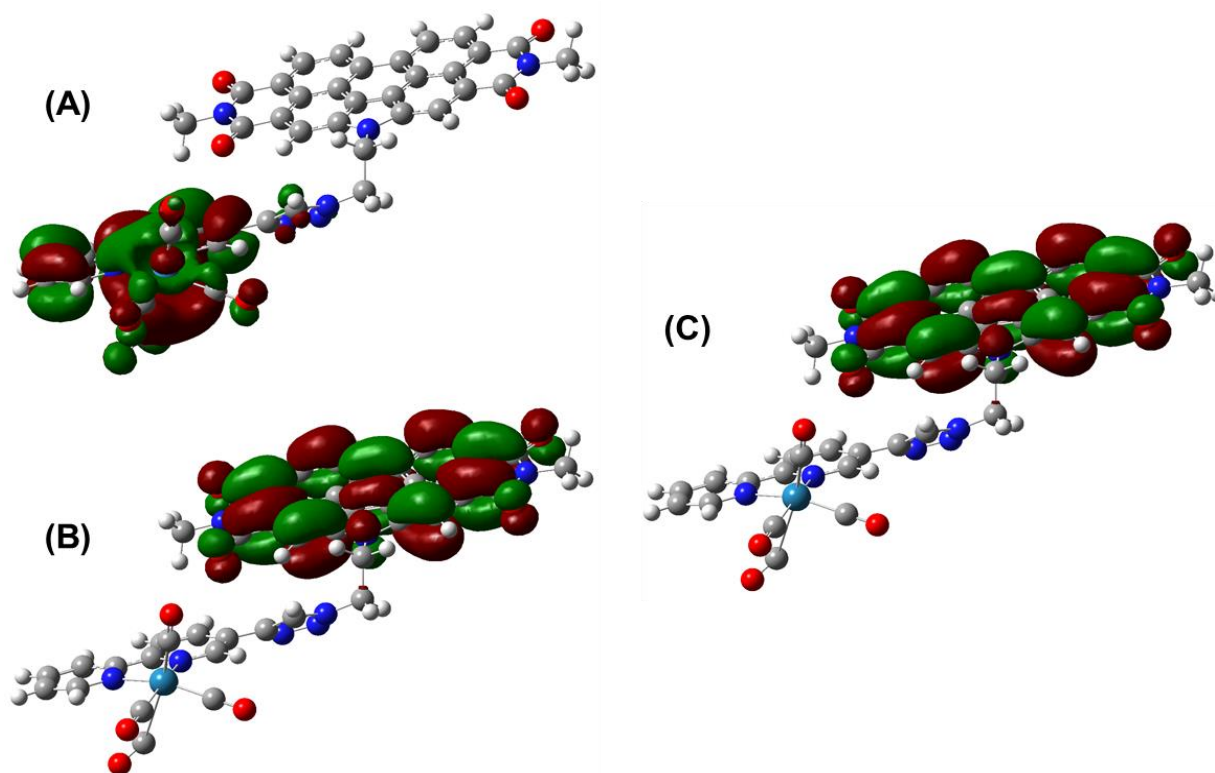


Figure S63. Frontier molecular orbitals of the triplet state of $\text{Re}^{\text{I}}[(\text{CO})_4(\text{bpy-TAz-PDI})]^{2-}$ at the M06/6-31G(d,p)/LANL2DZ level of theory, where (A) represents the HOMO, and (B & C) are the HOMO-1 with α - and β -spins, respectively.

9. X-ray Diffraction

The selected crystal was mounted on a glass loop using Paratone. Diffraction experiments were performed on a Bruker Smart diffractometer equipped with an Incoatec Microfocus (Cu K α , $\lambda = 1.54178 \text{ \AA}$) and an APEX II CCD detector. The crystal was kept at 173 K during data collection. Diffractions spots were integrated and scaled with SAINT³⁴ and the space group was determined with XPREP.³⁵ Using Olex2,³⁶ the structure was solved with the ShelXT³⁷ structure solution program using Intrinsic Phasing and refined with the ShelXL³⁸ refinement package using Least Squares minimisation. Weak diffraction and unresolvable twinning prevented a complete structural solution and required that several restraints be used to obtain a stable model; notably, restraining the Uij components (SIMU) for the whole structure and the carbonyl and pentyl distances *via* SADI.

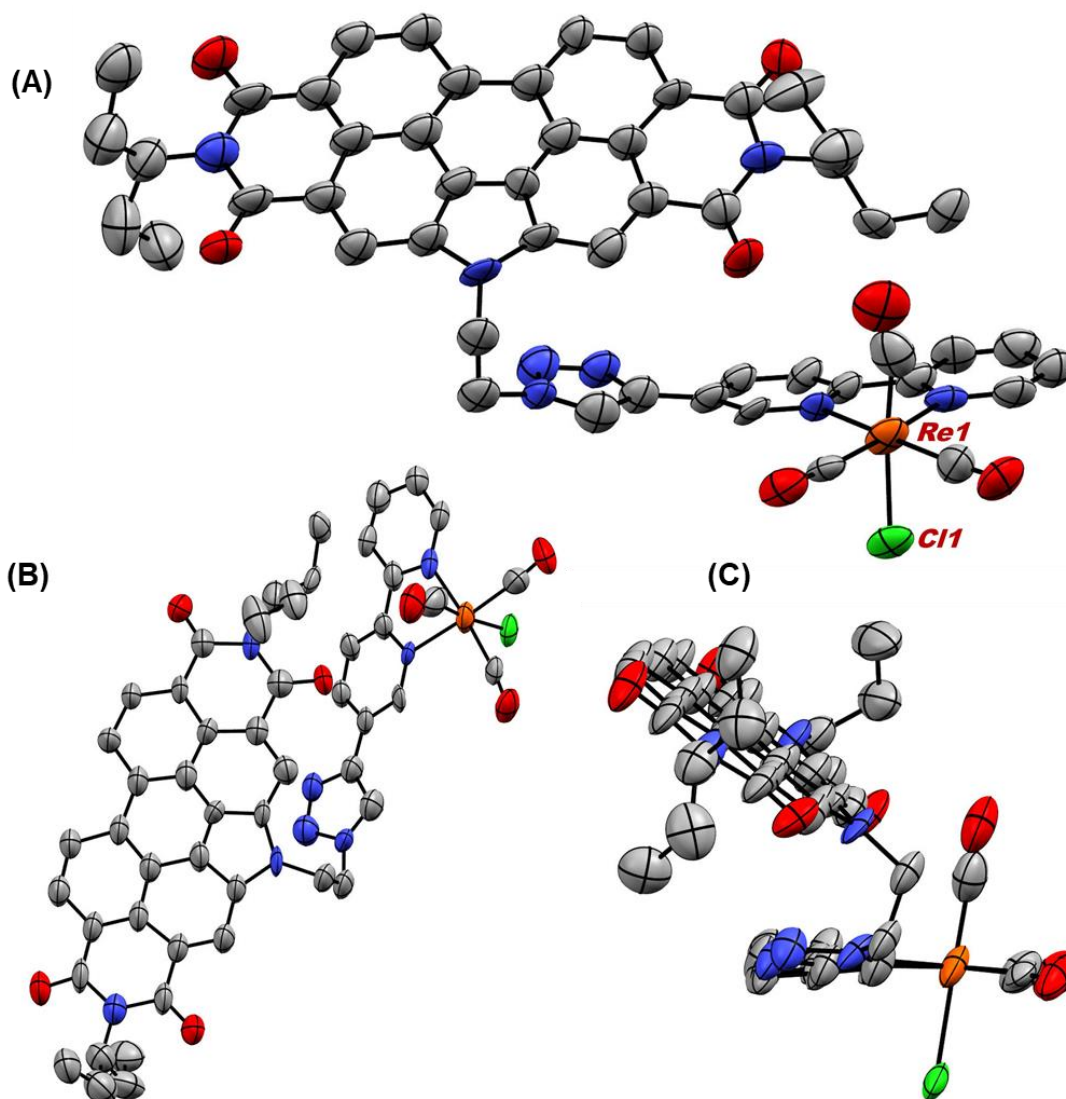


Figure S64. Single-crystal X-ray diffraction connectivity map of Re(bpy-TAz-PDI), showing the face-on (A), top-view (B), and side-view (C), as determined by X-ray diffraction crystallography (where: grey = carbon, blue = nitrogen, red = oxygen, green = chlorine, and orange = rhenium). Hydrogen atoms and outer-sphere solvent molecules have been omitted for clarity.

Table S4. Re(bpy-TAz-PDI) crystal data and structure refinement for repdi_sq

| | |
|---|--|
| Identification code | repdi_sq |
| Empirical formula | C ₅₁ H ₄₀ ClN ₈ O ₇ Re |
| Formula weight | 1098.56 |
| Temperature/K | 173.0 |
| Crystal system | triclinic |
| Space group | P-1 |
| a/Å | 11.2408(10) |
| b/Å | 17.2057(16) |
| c/Å | 18.3623(16) |
| α/° | 113.446(6) |
| β/° | 100.320(7) |
| γ/° | 103.520(7) |
| Volume/Å³ | 3016.8(5) |
| Z | 2 |
| ρ_{calc}/cm³ | 1.209 |
| μ/mm⁻¹ | 4.744 |
| F(000) | 1100.0 |
| Crystal size/mm³ | 0.354 × 0.119 × 0.117 |
| Radiation | CuKα (λ = 1.54178) |
| 2θ range for data collection/° | 17.184 to 99.998 |
| Index ranges | -9 ≤ h ≤ 11, -17 ≤ k ≤ 14, -18 ≤ l ≤ 18 |
| Reflections collected | 5575 |
| Independent reflections | 5575 [R _{int} = 0.0561, R _{sigma} = 0.0905] |
| Data/restraints/parameters | 5575/1463/617 |
| Goodness-of-fit on F² | 1.114 |
| Final R indexes [I ≥ 2σ (I)] | R ₁ = 0.1250, wR ₂ = 0.3165 |
| Final R indexes [all data] | R ₁ = 0.1466, wR ₂ = 0.3437 |
| Largest diff. peak/hole / e Å⁻³ | 4.33/-1.41 |

Table S5. Fractional Atomic Coordinates ($\times 10^4$) and Equivalent Isotropic Displacement Parameters ($\text{\AA}^2 \times 10^3$) for repdi_sq. U_{eq} is defined as 1/3 of of the trace of the orthogonalised U_{ij} tensor.

| Atom | <i>x</i> | <i>y</i> | <i>z</i> | U(eq) |
|------|------------|------------|------------|-----------|
| Re1 | 6104.6 (9) | 3170.9 (8) | 3855.1 (7) | 70.0 (6) |
| Cl1 | 6887 (5) | 4450 (4) | 3564 (4) | 65.8 (15) |
| O1 | 6666 (18) | 3063 (12) | 6385 (10) | 88 (5) |
| O2 | 9420 (16) | 1960 (12) | 7501 (10) | 85 (5) |
| O3 | 8812 (18) | 6972 (14) | 13777 (11) | 97 (5) |
| O4 | 5969 (18) | 7556 (12) | 12167 (11) | 86 (5) |
| O5 | 3735 (13) | 3664 (12) | 4197 (11) | 83 (5) |
| O6 | 4590 (20) | 1902 (12) | 1999 (9) | 103 (6) |
| O7 | 5080 (18) | 1590 (15) | 4213 (14) | 121 (7) |
| N1 | 7976 (18) | 2460 (13) | 6936 (12) | 72 (4) |
| N2 | 7470 (20) | 7305 (15) | 13002 (13) | 83 (5) |
| N3 | 5846 (17) | 5319 (12) | 9088 (11) | 64 (4) |
| N4 | 7882 (19) | 6488 (14) | 8556 (13) | 79 (5) |
| N5 | 6560 (17) | 6207 (12) | 8090 (11) | 61 (4) |
| N7 | 7433 (14) | 4086 (11) | 5117 (10) | 50 (3) |
| N8 | 7913 (16) | 2994 (11) | 3807 (11) | 59 (4) |
| N37 | 8501 (18) | 6187 (13) | 8009 (12) | 70 (4) |
| C1 | 6460 (20) | 4694 (15) | 8736 (13) | 59 (4) |
| C2 | 6460 (20) | 4157 (16) | 7920 (15) | 71 (5) |
| C3 | 7240 (20) | 3632 (16) | 7860 (15) | 72 (5) |
| C4 | 7290 (20) | 3060 (17) | 7008 (16) | 77 (5) |
| C5 | 8760 (30) | 2419 (17) | 7592 (15) | 75 (5) |
| C6 | 8800 (20) | 3041 (15) | 8438 (13) | 65 (5) |
| C7 | 9520 (20) | 3094 (16) | 9170 (14) | 69 (5) |
| C8 | 9580 (20) | 3699 (16) | 9984 (14) | 68 (5) |
| C9 | 8750 (20) | 4218 (17) | 10057 (15) | 73 (5) |
| C10 | 8720 (20) | 4885 (16) | 10876 (15) | 70 (5) |
| C11 | 9410 (20) | 5050 (17) | 11703 (14) | 74 (5) |
| C12 | 9260 (20) | 5693 (16) | 12402 (16) | 72 (5) |
| C13 | 8430 (20) | 6186 (17) | 12355 (15) | 70 (5) |
| C14 | 8290 (20) | 6844 (18) | 13089 (16) | 78 (5) |
| C15 | 6690 (20) | 7135 (17) | 12214 (15) | 73 (5) |
| C16 | 6840 (20) | 6468 (16) | 11434 (15) | 69 (5) |
| C17 | 6190 (20) | 6380 (17) | 10694 (15) | 70 (5) |
| C18 | 6310 (20) | 5684 (16) | 9950 (14) | 64 (5) |
| C19 | 8020 (20) | 3603 (16) | 8542 (14) | 66 (4) |
| C20 | 8030 (20) | 4181 (17) | 9338 (15) | 72 (5) |
| C21 | 7280 (20) | 4673 (15) | 9370 (14) | 62 (4) |
| C22 | 7170 (20) | 5249 (16) | 10089 (14) | 65 (4) |
| C23 | 7880 (20) | 5368 (17) | 10881 (15) | 71 (5) |
| C24 | 7730 (20) | 6033 (16) | 11604 (15) | 71 (5) |
| C25 | 8460 (20) | 1427 (15) | 4734 (11) | 75 (6) |
| C26 | 8187 (18) | 2124 (12) | 5442 (11) | 59 (5) |
| C27 | 7829 (19) | 1748 (14) | 6060 (12) | 81 (6) |

| | | | | |
|-----|------------|-----------|------------|----------|
| C28 | 6440 (20) | 1076 (18) | 5739 (14) | 99 (7) |
| C29 | 6110 (30) | 790 (20) | 6387 (17) | 124 (11) |
| C30 | 8890 (30) | 9270 (17) | 13600 (20) | 110 (9) |
| C31 | 7680 (30) | 8966 (16) | 13830 (20) | 112 (8) |
| C32 | 7430 (20) | 8015 (15) | 13762 (18) | 89 (6) |
| C33 | 6210 (20) | 7713 (18) | 14000 (20) | 107 (8) |
| C34 | 6130 (30) | 6887 (18) | 14134 (18) | 106 (9) |
| C35 | 5010 (20) | 5611 (17) | 8628 (16) | 73 (5) |
| C36 | 5700 (20) | 6428 (17) | 8548 (15) | 69 (5) |
| C37 | 6400 (20) | 5767 (18) | 7311 (17) | 80 (6) |
| C38 | 7600 (20) | 5695 (16) | 7224 (15) | 67 (5) |
| C39 | 7140 (20) | 4611 (14) | 5751 (12) | 53 (4) |
| C40 | 8020 (20) | 5234 (15) | 6514 (13) | 57 (4) |
| C41 | 9267 (19) | 5310 (15) | 6593 (13) | 57 (4) |
| C42 | 9620 (20) | 4785 (15) | 5948 (13) | 59 (5) |
| C43 | 8688 (19) | 4150 (14) | 5204 (12) | 53 (4) |
| C44 | 8950 (20) | 3515 (15) | 4494 (14) | 64 (5) |
| C45 | 10210 (20) | 3433 (17) | 4503 (16) | 74 (5) |
| C46 | 10330 (30) | 2826 (17) | 3839 (17) | 82 (6) |
| C47 | 9290 (20) | 2259 (16) | 3078 (15) | 72 (5) |
| C48 | 8130 (20) | 2384 (16) | 3122 (15) | 67 (5) |
| C49 | 4552 (17) | 3420 (13) | 4005 (12) | 53 (4) |
| C50 | 5090 (20) | 2383 (15) | 2696 (12) | 80 (6) |
| C51 | 5500 (30) | 2094 (15) | 3986 (19) | 92 (6) |

Table S6. Anisotropic Displacement Parameters ($\text{\AA}^2 \times 10^3$) for repdi_sq. The Anisotropic displacement factor exponent takes the form: $-\pi^2[h^2a^{*2}U_{11}+2hka^*b^*U_{12}+\dots]$.

| Atom | U ₁₁ | U ₂₂ | U ₃₃ | U ₂₃ | U ₁₃ | U ₁₂ |
|------|-----------------|-----------------|-----------------|-----------------|-----------------|-----------------|
| Re1 | 52.3 (8) | 117.0 (11) | 59.1 (8) | 53.1 (7) | 10.0 (5) | 42.6 (6) |
| Cl1 | 42 (3) | 100 (4) | 67 (3) | 54 (3) | 2 (2) | 28 (3) |
| O1 | 105 (11) | 136 (12) | 45 (9) | 49 (9) | 16 (8) | 73 (10) |
| O2 | 80 (10) | 114 (11) | 67 (10) | 36 (9) | 15 (8) | 60 (9) |
| O3 | 95 (12) | 152 (14) | 63 (10) | 59 (10) | 11 (9) | 66 (10) |
| O4 | 113 (12) | 113 (11) | 72 (10) | 62 (9) | 35 (9) | 70 (10) |
| O5 | 53 (9) | 146 (14) | 98 (12) | 86 (11) | 35 (8) | 54 (9) |
| O6 | 125 (15) | 131 (15) | 50 (10) | 45 (11) | 6 (10) | 48 (12) |
| O7 | 82 (13) | 170 (20) | 108 (16) | 68 (14) | 0 (12) | 59 (13) |
| N1 | 77 (8) | 97 (8) | 56 (8) | 47 (7) | 3 (7) | 44 (7) |
| N2 | 82 (9) | 114 (9) | 68 (8) | 49 (7) | 15 (8) | 51 (8) |
| N3 | 68 (8) | 104 (8) | 48 (7) | 56 (7) | 10 (6) | 47 (7) |
| N4 | 69 (10) | 109 (10) | 68 (10) | 46 (8) | 20 (8) | 38 (8) |
| N5 | 71 (8) | 100 (9) | 56 (8) | 53 (7) | 32 (7) | 63 (7) |
| N7 | 46 (7) | 81 (8) | 40 (7) | 36 (6) | 8 (6) | 42 (6) |
| N8 | 61 (6) | 67 (6) | 55 (6) | 41 (5) | -1 (5) | 24 (5) |
| N37 | 63 (9) | 108 (10) | 58 (9) | 48 (8) | 16 (8) | 46 (8) |
| C1 | 61 (8) | 94 (9) | 51 (8) | 51 (7) | 15 (7) | 45 (7) |
| C2 | 67 (9) | 103 (10) | 60 (9) | 46 (8) | 22 (8) | 38 (8) |
| C3 | 79 (9) | 94 (9) | 58 (8) | 42 (7) | 16 (8) | 47 (8) |
| C4 | 83 (10) | 95 (10) | 60 (10) | 34 (8) | 18 (9) | 47 (8) |
| C5 | 84 (10) | 97 (10) | 55 (9) | 38 (8) | 15 (9) | 49 (9) |
| C6 | 75 (9) | 99 (9) | 47 (8) | 48 (7) | 15 (7) | 52 (7) |
| C7 | 75 (10) | 102 (10) | 46 (9) | 37 (8) | 13 (8) | 55 (8) |
| C8 | 67 (10) | 106 (10) | 52 (9) | 42 (8) | 25 (8) | 52 (8) |
| C9 | 74 (9) | 107 (9) | 58 (8) | 48 (7) | 13 (8) | 49 (8) |
| C10 | 69 (9) | 102 (9) | 58 (8) | 49 (7) | 10 (8) | 45 (7) |
| C11 | 76 (10) | 104 (10) | 54 (10) | 42 (9) | 11 (9) | 47 (9) |
| C12 | 64 (10) | 104 (10) | 63 (10) | 50 (8) | 13 (9) | 39 (8) |
| C13 | 63 (9) | 104 (9) | 64 (9) | 51 (8) | 10 (8) | 44 (8) |
| C14 | 76 (10) | 116 (10) | 64 (10) | 62 (8) | 5 (9) | 45 (9) |
| C15 | 75 (10) | 109 (10) | 63 (9) | 60 (8) | 15 (8) | 48 (9) |
| C16 | 72 (9) | 97 (9) | 64 (9) | 52 (7) | 19 (8) | 48 (7) |
| C17 | 60 (9) | 110 (10) | 62 (9) | 51 (8) | 17 (8) | 46 (8) |
| C18 | 59 (8) | 103 (9) | 53 (8) | 47 (7) | 14 (7) | 45 (7) |
| C19 | 64 (8) | 98 (8) | 56 (8) | 42 (7) | 15 (7) | 50 (7) |
| C20 | 70 (8) | 104 (8) | 59 (8) | 49 (7) | 15 (7) | 42 (7) |
| C21 | 64 (8) | 94 (8) | 54 (8) | 41 (7) | 22 (7) | 55 (7) |
| C22 | 63 (8) | 100 (8) | 55 (8) | 52 (7) | 16 (7) | 38 (7) |
| C23 | 64 (8) | 105 (8) | 58 (8) | 46 (7) | 13 (7) | 43 (7) |
| C24 | 69 (8) | 104 (8) | 58 (8) | 51 (7) | 11 (7) | 44 (7) |
| C25 | 46 (12) | 129 (16) | 54 (11) | 45 (11) | 9 (10) | 34 (11) |
| C26 | 52 (8) | 66 (8) | 59 (8) | 29 (6) | -7 (6) | 33 (6) |
| C27 | 93 (11) | 85 (10) | 68 (10) | 39 (9) | 8 (9) | 39 (9) |
| C28 | 110 (14) | 86 (12) | 75 (12) | 40 (10) | -3 (11) | 7 (11) |

| | | | | | | |
|-----|----------|----------|----------|---------|---------|---------|
| C29 | 150 (20) | 111 (18) | 87 (17) | 64 (15) | -6 (15) | -1 (17) |
| C30 | 130 (20) | 94 (18) | 110 (20) | 40 (16) | 51 (18) | 47 (16) |
| C31 | 109 (14) | 123 (14) | 90 (14) | 25 (12) | 49 (12) | 45 (12) |
| C32 | 93 (11) | 116 (11) | 74 (10) | 49 (9) | 34 (10) | 47 (10) |
| C33 | 111 (15) | 128 (15) | 79 (13) | 42 (12) | 33 (12) | 41 (13) |
| C34 | 106 (19) | 150 (20) | 69 (16) | 49 (15) | 14 (15) | 57 (16) |
| C35 | 61 (10) | 112 (11) | 66 (10) | 49 (9) | 16 (9) | 53 (9) |
| C36 | 57 (10) | 110 (11) | 67 (10) | 54 (9) | 17 (9) | 50 (9) |
| C37 | 64 (10) | 109 (11) | 72 (10) | 44 (9) | 9 (9) | 42 (9) |
| C38 | 55 (9) | 100 (10) | 60 (9) | 43 (8) | 16 (8) | 41 (8) |
| C39 | 56 (9) | 94 (10) | 38 (8) | 50 (8) | 16 (7) | 38 (8) |
| C40 | 54 (8) | 92 (9) | 48 (8) | 48 (7) | 14 (7) | 39 (7) |
| C41 | 50 (9) | 90 (9) | 46 (9) | 42 (8) | 13 (7) | 32 (7) |
| C42 | 51 (9) | 97 (10) | 43 (9) | 42 (8) | 15 (8) | 30 (8) |
| C43 | 49 (8) | 86 (9) | 45 (8) | 43 (7) | 17 (7) | 32 (7) |
| C44 | 59 (9) | 89 (9) | 50 (8) | 41 (7) | 6 (8) | 29 (8) |
| C45 | 60 (10) | 102 (11) | 62 (10) | 40 (9) | -4 (9) | 42 (8) |
| C46 | 76 (11) | 94 (11) | 72 (11) | 40 (9) | 0 (10) | 33 (9) |
| C47 | 71 (10) | 95 (11) | 56 (10) | 38 (9) | 11 (9) | 37 (9) |
| C48 | 67 (10) | 90 (11) | 62 (10) | 48 (9) | 8 (9) | 40 (9) |
| C49 | 54 (7) | 70 (8) | 52 (8) | 45 (6) | 12 (6) | 26 (6) |
| C50 | 90 (12) | 108 (12) | 71 (12) | 49 (10) | 35 (11) | 62 (10) |
| C51 | 72 (9) | 102 (9) | 91 (9) | 31 (7) | 8 (7) | 46 (7) |

10. References

- (1) Williams, D. B. G.; Lawton, M. Drying of Organic Solvents: Quantitative Evaluation of the Efficiency of Several Desiccants. *J. Org. Chem.* **2010**, 75 (24), 8351–8354. <https://doi.org/10.1021/jo101589h>.
- (2) Lalancette, J.-M.; Rollin, G.; Dumas, P. Metals Intercalated in Graphite. I. Reduction and Oxidation. *Can. J. Chem.* **1972**, 50 (18), 3058–3062. <https://doi.org/10.1139/v72-485>.
- (3) Stoll, S.; Schweiger, A. EasySpin, a Comprehensive Software Package for Spectral Simulation and Analysis in EPR. *J. Magn. Reson.* **2006**, 178 (1), 42–55. <https://doi.org/10.1016/j.jmr.2005.08.013>.
- (4) Molton, F. Simultispin: A Versatile Graphical User Interface for the Simulation of Solid-State Continuous Wave EPR Spectra. *Magn. Reson. Chem.* **2020**, 58 (8), 718–726. <https://doi.org/10.1002/mrc.5019>.
- (5) Koenig, J. D. B.; Willkomm, J.; Roesler, R.; Piers, W. E.; Welch, G. C. Electrocatalytic CO₂ Reduction at Lower Overpotentials Using Iron(III) Tetra(Meso-Thienyl)Porphyrins. *ACS Appl. Energy Mater.* **2019**, 2 (6), 4022–4026. <https://doi.org/10.1021/acsaelm.9b00761>.
- (2) Bard, A. J.; Faulkner, L. R. *Electrochemical Methods: Fundamentals and Applications*, 2nd Edition | Wiley: 2008.
- (7) Clark, M. L.; Cheung, P. L.; Lessio, M.; Carter, E. A.; Kubiak, C. P. Kinetic and Mechanistic Effects of Bipyridine (Bpy) Substituent, Labile Ligand, and Brønsted Acid on Electrocatalytic CO₂ Reduction by Re(Bpy) Complexes. *ACS Catal.* **2018**, 8 (3), 2021–2029. <https://doi.org/10.1021/acscatal.7b03971>.
- (8) Azcarate, I.; Costentin, C.; Robert, M.; Savéant, J.-M. Through-Space Charge Interaction Substituent Effects in Molecular Catalysis Leading to the Design of the Most Efficient Catalyst of CO₂-to-CO Electrochemical Conversion. *J. Am. Chem. Soc.* **2016**, 138 (51), 16639–16644. <https://doi.org/10.1021/jacs.6b07014>.
- (9) Smith, T. J.; Stevenson, K. J. 4 - Reference Electrodes. In *Handbook of Electrochemistry*; Zoski, C. G., Ed.; Elsevier: Amsterdam, 2007; pp 73–110. <https://doi.org/10.1016/B978-044451958-0.50005-7>.
- (10) D'Souza, D. M.; Leigh, D. A.; Papmeyer, M.; Woltering, S. L. A Scalable Synthesis of 5,5'-Dibromo-2,2'-Bipyridine and Its Stepwise Functionalization via Stille Couplings. *Nat. Protoc.* **2012**, 7 (11), 2022–2028. <https://doi.org/10.1038/nprot.2012.122>.
- (11) Grosshenny, V.; Romero, F. M.; Ziessel, R. Construction of Preorganized Polytopic Ligands via Palladium-Promoted Cross-Coupling Reactions. *J. Org. Chem.* **1997**, 62 (5), 1491–1500. <https://doi.org/10.1021/jo962068w>.
- (12) Hendsbee, A. D.; Sun, J.-P.; Law, W. K.; Yan, H.; Hill, I. G.; Spasyuk, D. M.; Welch, G. C. Synthesis, Self-Assembly, and Solar Cell Performance of N-Annulated Perylene Diimide Non-Fullerene Acceptors. *Chem. Mater.* **2016**, 28 (19), 7098–7109. <https://doi.org/10.1021/acs.chemmater.6b03292>.
- (13) Cann, J. R.; Cabanetos, C.; Welch, G. C. Synthesis of Molecular Dyads and Triads Based Upon N-Annulated Perylene Diimide Monomers and Dimers. *Eur. J. Org. Chem.* **2018**, 2018 (48), 6933–6943. <https://doi.org/10.1002/ejoc.201801383>.
- (14) Dubrawski, Z.; Heidebrecht, J.; Lombardi, B. M. P.; Hyla, A. S.; Willkomm, J.; Radford, C. L.; Lin, J.-B.; Welch, G. C.; Ponnurangam, S.; Roesler, R.; Prokopchuk, D. E.; Piers, W. E. Ligand-Centered Electrochemical Processes Enable CO₂ Reduction with a Nickel Bis(Triazapentadienyl) Complex. *Sustain. Energy Fuels* **2019**, 3 (5), 1172–1181. <https://doi.org/10.1039/C8SE00623G>.
- (15) Fulmer, G. R.; Miller, A. J. M.; Sherden, N. H.; Gottlieb, H. E.; Nudelman, A.; Stoltz, B. M.; Bercaw, J. E.; Goldberg, K. I. NMR Chemical Shifts of Trace Impurities: Common

- Laboratory Solvents, Organics, and Gases in Deuterated Solvents Relevant to the Organometallic Chemist. *Organometallics* **2010**, 29 (9), 2176–2179. <https://doi.org/10.1021/om100106e>.
- (16) Hawecker, J.; Lehn, J.-M.; Ziessel, R. Electrocatalytic Reduction of Carbon Dioxide Mediated by Re(Bipy)(CO)₃Cl (Bipy = 2,2'-Bipyridine). *J. Chem. Soc. Chem. Commun.* **1984**, 0 (6), 328–330. <https://doi.org/10.1039/C39840000328>.
 - (17) Smieja, J. M.; Kubiak, C. P. Re(Bipy-TBu)(CO)₃Cl–improved Catalytic Activity for Reduction of Carbon Dioxide: IR-Spectroelectrochemical and Mechanistic Studies. *Inorg. Chem.* **2010**, 49, 9283–9289. <https://doi.org/10.1021/ic1008363>.
 - (18) Machan, C. W.; Chabolla, S. A.; Yin, J.; Gilson, M. K.; Tezcan, F. A.; Kubiak, C. P. Supramolecular Assembly Promotes the Electrocatalytic Reduction of Carbon Dioxide by Re(I) Bipyridine Catalysts at a Lower Overpotential. *J. Am. Chem. Soc.* **2014**, 136 (41), 14598–14607. <https://doi.org/10.1021/ja5085282>.
 - (19) Haviv, E.; Azaiza-Dabbah, D.; Carmieli, R.; Avram, L.; Martin, J. M. L.; Neumann, R. A Thiourea Tether in the Second Coordination Sphere as a Binding Site for CO₂ and a Proton Donor Promotes the Electrochemical Reduction of CO₂ to CO Catalyzed by a Rhenium Bipyridine-Type Complex. *J. Am. Chem. Soc.* **2018**, 140 (39), 12451–12456. <https://doi.org/10.1021/jacs.8b05658>.
 - (20) Sung, S.; Kumar, D.; Gil-Sepulcre, M.; Nippe, M. Electrocatalytic CO₂ Reduction by Imidazolium-Functionalized Molecular Catalysts. *J. Am. Chem. Soc.* **2017**, 139 (40), 13993–13996. <https://doi.org/10.1021/jacs.7b07709>.
 - (21) Hellman, A. N.; Haiges, R.; Marinescu, S. C. Rhenium Bipyridine Catalysts with Hydrogen Bonding Pendant Amines for CO₂ Reduction. *Dalton Trans.* **2019**, 48 (38), 14251–14255. <https://doi.org/10.1039/C9DT02689D>.
 - (22) Franco, F.; Cometto, C.; Garino, C.; Minero, C.; Sordello, F.; Nervi, C.; Gobetto, R. Photo- and Electrocatalytic Reduction of CO₂ by [Re(CO)₃α,α'-Diimine-(4-Piperidinyl-1,8-Naphthalimide)Cl] Complexes. *Eur. J. Inorg. Chem.* **2015**, 2015 (2), 296–304. <https://doi.org/10.1002/ejic.201402912>.
 - (23) Sun Cunfa; Rotundo Laura; Garino Claudio; Nencini Luca; Yoon Sam S.; Gobetto Roberto; Nervi Carlo. Electrochemical CO₂ Reduction at Glassy Carbon Electrodes Functionalized by MnI and ReI Organometallic Complexes. *ChemPhysChem* **2017**, 18 (22), 3219–3229. <https://doi.org/10.1002/cphc.201700739>.
 - (24) Qiao, X.; Li, Q.; Schaugaard, R. N.; Noffke, B. W.; Liu, Y.; Li, D.; Liu, L.; Raghavachari, K.; Li, L. Well-Defined Nanographene–Rhenium Complex as an Efficient Electrocatalyst and Photocatalyst for Selective CO₂ Reduction. *J. Am. Chem. Soc.* **2017**, 139 (11), 3934–3937. <https://doi.org/10.1021/jacs.6b12530>.
 - (25) Frisch, M. J.; Trucks, G. W.; Schlegel, H. B.; Scuseria, G. E.; Robb, M. A.; Cheeseman, J. R.; Scalmani, G.; Barone, V.; Petersson, G. A.; Nakatsuji, H.; Li, X.; Caricato, M.; Marenich, A. V.; Bloino, J.; Janesko, B. G.; Gomperts, R.; Mennucci, B.; Hratchian, H. P.; Ortiz, J. V.; Izmaylov, A. F.; Sonnenberg, J. L.; Williams-Young, D.; Ding, F.; Lipparini, F.; Egidi, F.; Goings, J.; Peng, B.; Petrone, A.; Henderson, T.; Ranasinghe, D.; Zakrzewski, V. G.; Gao, J.; Rega, N.; Zheng, G.; Liang, W.; Hada, M.; Ehara, M.; Toyota, K.; Fukuda, R.; Hasegawa, J.; Ishida, M.; Nakajima, T.; Honda, Y.; Kitao, O.; Nakai, H.; Vreven, T.; Throssell, K.; Montgomery, J. A., Jr.; Peralta, J. E.; Ogliaro, F.; Bearpark, M. J.; Heyd, J. J.; Brothers, E. N.; Kudin, K. N.; Staroverov, V. N.; Keith, T. A.; Kobayashi, R.; Normand, J.; Raghavachari, K.; Rendell, A. P.; Burant, J. C.; Iyengar, S. S.; Tomasi, J.; Cossi, M.; Millam, J. M.; Klene, M.; Adamo, C.; Cammi, R.; Ochterski, J. W.; Martin, R. L.; Morokuma, K.; Farkas, O.; Foresman, J. B.; Fox, D. J. Gaussian 16 Revision A.03, Gaussian Inc: Wallingford CT, 2016.

- (26) Zhao, Y.; Truhlar, D. G. The M06 Suite of Density Functionals for Main Group Thermochemistry, Thermochemical Kinetics, Noncovalent Interactions, Excited States, and Transition Elements: Two New Functionals and Systematic Testing of Four M06-Class Functionals and 12 Other Functionals. *Theor. Chem. Acc.* **2008**, *120* (1), 215–241. <https://doi.org/10.1007/s00214-007-0310-x>.
- (27) Hariharan, P. C.; Pople, J. A. The Influence of Polarization Functions on Molecular Orbital Hydrogenation Energies. *Theor. Chim. Acta* **1973**, *28* (3), 213–222. <https://doi.org/10.1007/BF00533485>.
- (28) Petersson, G. A.; Bennett, A.; Tensfeldt, T. G.; Al-Laham, M. A.; Shirley, W. A.; Mantzaris, J. A Complete Basis Set Model Chemistry. I. The Total Energies of Closed-shell Atoms and Hydrides of the First-row Elements. *J. Chem. Phys.* **1988**, *89* (4), 2193–2218. <https://doi.org/10.1063/1.455064>.
- (29) Petersson, G. A.; Al-Laham, M. A. A Complete Basis Set Model Chemistry. II. Open-shell Systems and the Total Energies of the First-row Atoms. *J. Chem. Phys.* **1991**, *94* (9), 6081–6090. <https://doi.org/10.1063/1.460447>.
- (30) Hehre, W. J.; Ditchfield, R.; Pople, J. A. Self—Consistent Molecular Orbital Methods. XII. Further Extensions of Gaussian—Type Basis Sets for Use in Molecular Orbital Studies of Organic Molecules. *J. Chem. Phys.* **1972**, *56* (5), 2257–2261. <https://doi.org/10.1063/1.1677527>.
- (31) Hay, P. J.; Wadt, W. R. Ab Initio Effective Core Potentials for Molecular Calculations. Potentials for the Transition Metal Atoms Sc to Hg. *J. Chem. Phys.* **1985**, *82* (1), 270–283. <https://doi.org/10.1063/1.448799>.
- (32) Wadt, W. R.; Hay, P. J. Ab Initio Effective Core Potentials for Molecular Calculations. Potentials for Main Group Elements Na to Bi. *J. Chem. Phys.* **1985**, *82* (1), 284–298. <https://doi.org/10.1063/1.448800>.
- (33) Dennington, R.; Keith, T. A.; Millam, J. M. GaussView, Version 5.0.9, Semichem Inc., Shawnee Mission: KS, 2009.
- (34) Bruker-AXS. SAINT; Madison, Wisconsin, USA, 2017.
- (35) Bruker-AXS. XPREP; Madison, Wisconsin, USA, 2017.
- (36) Dolomanov, O. V.; Bourhis, L. J.; Gildea, R. J.; Howard, J. a. K.; Puschmann, H. OLEX2: A Complete Structure Solution, Refinement and Analysis Program. *J. Appl. Crystallogr.* **2009**, *42* (2), 339–341. <https://doi.org/10.1107/S0021889808042726>.
- (37) Sheldrick, G.M. (2015). Acta Cryst. A71, 3-8.
- (38) Sheldrick, G.M. (2015). Acta Cryst. C71, 3-8.